Review article

JGS
Journal of the Geological Society

https://doi.org/10.1144/jgs2021-081 | Vol. 179 | 2022 | jgs2021-081

Dynamic interplay of biogeochemical C, S and Ba cycles in response to the Shuram oxygenation event

Huan Cui[1,2]*, Alan J. Kaufman[3], Shuhai Xiao[4], Chuanming Zhou[5], Maoyan Zhu[5,6], Mengchun Cao[7], Sean Loyd[8], Peter Crockford[9,10], Xiao-Ming Liu[11], Steven Goderis[12], Wei Wang[5] and Chengguo Guan[5]

[1] Equipe Géomicrobiologie, Institut de Physique du Globe de Paris (IPGP), Université de Paris, 75005 Paris, France
[2] Stable Isotope Laboratory, Department of Earth Sciences, University of Toronto, Toronto, ON M5S 3B1, Canada
[3] Department of Geology and Earth System Science Interdisciplinary Center, University of Maryland, College Park, MD 20742, USA
[4] Department of Geosciences and Global Change Center, Virginia Tech, Blacksburg, VA 24061, USA
[5] State Key Laboratory of Palaeobiology and Stratigraphy, Nanjing Institute of Geology and Palaeontology, and Center for Excellence in Life and Paleoenvironment, Chinese Academy of Sciences, Nanjing 210008, China
[6] College of Earth and Planetary Sciences, University of Chinese Academy of Sciences, Beijing 100049, China
[7] School of Earth Sciences and Engineering, and Frontiers Science Center for Critical Earth Material Cycling, Nanjing University, Nanjing 210023, China
[8] Department of Geological Sciences, California State University, Fullerton, Fullerton, CA 92831, USA
[9] Department of Earth and Planetary Sciences, Weizmann Institute of Science, Rehovot 76100, Israel
[10] Department of Earth and Planetary Sciences, Harvard University, Cambridge, MA 02138, USA
[11] Department of Geological Sciences, University of North Carolina, Chapel Hill, NC 27599, USA
[12] Research Group of Analytical, Environmental and Geo-Chemistry, Vrije Universiteit Brussel, Brussels, Belgium
HC, 0000-0003-0705-3423; AJK, 0000-0003-4129-6445; SX, 0000-0003-4655-2663; MZ, 0000-0001-7327-9856; X-ML, 0000-0001-7904-1056; SG, 0000-0002-6666-7153; WW, 0000-0002-4954-1831
* Correspondence: huan.cui@ipgp.fr

Abstract: Compared with Phanerozoic strata, sulfate minerals are relatively rare in the Precambrian record; this is probably due to the lower concentrations of sulfate in dominantly anoxic oceans. Here, we present a compilation of sulfate minerals that are stratigraphically associated with the Ediacaran Shuram excursion (SE) – the largest negative $\delta^{13}C$ excursion in Earth history. We evaluated 15 SE sections, all of which reveal the presence of sulfate minerals and/or enriched carbonate-associated sulfate concentrations, suggesting a rise in the sulfate reservoir. Notably, where data are available, the SE also reveals considerable enrichments in [Ba] relative to pre- and post-SE intervals. We propose that elevated seawater sulfate concentrations during the SE may have facilitated authigenesis of sulfate minerals. At the same time, the rise in Ba concentrations in shelf environments further facilitated barite deposition. A larger sulfate reservoir would stimulate microbial sulfate reduction and anaerobic oxidation of organic matter (including methane), contributing to the genesis of the SE. The existence of sulfate minerals throughout the SE suggests that oxidant pools were not depleted at that time, which challenges previous modelling results. Our study highlights the dynamic interplay of biogeochemical C, S and Ba cycles in response to the Shuram oxygenation event.

Supplementary material: SEM and EDS data and figures S1-S4 and tables S1-S3 are available at: https://doi.org/10.6084/m9.figshare.c.5602560

Thematic collection: This article is part of the 'Sulfur in the Earth system' collection available at: https://www.lyellcollection.org/cc/sulfur-in-the-earth-system

Received 25 June 2021; **revised** 31 August 2021; **accepted** 3 September 2021

Sulfate minerals are a class of minerals that include the sulfate ion SO_4^{2-} within their structure and often occur within Phanerozoic strata (Claypool *et al.* 1980; Jewell 2000; Crockford *et al.* 2019*b*; Warren 2021). Common examples include gypsum ($CaSO_4{\cdot}2H_2O$), anhydrite ($CaSO_4$), barite ($BaSO_4$) and celestine ($SrSO_4$) (Arndt 2015). In the modern oxygenated ocean, sulfate is the second most abundant anion at a concentration of 28 mM and plays a critical role in organic matter remineralization within sediments (Berner and Berner 2012). With such a high concentration today, sulfate is well mixed due to its long residence time (>11 Myr) relative to the mixing time of the ocean (Berner and Berner 2012; Paytan and Gray 2012). Compared with Phanerozoic strata, sulfate minerals are relatively rare in Precambrian sedimentary archives (Warren 2021). This uneven distribution of sulfate minerals in the geological record is typically explained as a consequence of much lower sulfate concentrations in Precambrian seawater (Grotzinger and Kasting 1993; Kah *et al.* 2004; Canfield and Farquhar 2009; Bristow and Grotzinger 2013; Algeo *et al.* 2015; Blättler *et al.* 2020). Wherever they occur in Precambrian marine strata, sulfate minerals are often used as direct mineralogical evidence for a transient increase in sulfate levels indicative of an increasingly oxygenated environment (Kah *et al.* 2001; Melezhik *et al.* 2005; Schröder *et al.* 2008; Reuschel *et al.* 2012; Turner and Bekker 2016; Blättler *et al.* 2018; Prince *et al.* 2019).

Sulfate minerals have been widely used to infer the evolution of ocean chemistry in deep time (Holland 1984). Gypsum precipitates before halite (NaCl) and becomes supersaturated when the ion product (IP_{CaSO4}) exceeds 23 mM^2 (Holland 1984). The IP_{CaSO4} in the Precambrian may have been significantly lower than that in the modern ocean (280 mM^2). Assuming that the concentration of Ca^{2+}

over the last 550 Myr (10 to 40 mM, Horita *et al.* 2002) also applies to the Precambrian, SO_4^{2-} levels of around 0.5–2 mM would have been required to achieve a condition with $IP_{CaSO4} > 23$ mM^2 (Canfield and Farquhar 2009). If sulfate concentrations are below this level, or if IP_{CaSO4} is < 23 mM^2, gypsum is less likely to form, requiring highly restricted environments with high net evaporation. Barite has also been widely used as a proxy for ocean productivity and isotopic compositions of seawater (Paytan and Griffith 2007; Ma *et al.* 2014; Bao 2015; Carter *et al.* 2020; Yao *et al.* 2020; Wei *et al.* 2021*a*). Therefore, investigating the abundance and origin of these sulfate minerals in Precambrian strata has the potential to offer important insights into the biogeochemistry of the environments in which these archives were deposited.

One of the most prominent examples of inferred oxygenation events in the Ediacaran Period coincided with the Shuram Excursion (SE) –a negative stratigraphic carbon isotope ($\delta^{13}C$) excursion from +5‰ down to a nadir of −12‰ (Fike *et al.* 2006; McFadden *et al.* 2008; Lu *et al.* 2013; Shields *et al.* 2019; Zhang *et al.* 2019; Li *et al.* 2020*b*). The SE lasted for around 7 Myr (Gong and Li 2020; Rooney *et al.* 2020) and is widely regarded as one of the most profound carbon cycle anomalies in Earth history (Grotzinger *et al.* 2011). In the past few decades, the SE has been reported in Ediacaran strata around the world. The pattern and stratigraphic position of the globally distributed SE provides compelling evidence that this middle Ediacaran event represents an oceanographic perturbation of the deep-time carbon cycle (Grotzinger *et al.* 2011; Husson *et al.* 2015), as opposed to a post-depositional phenomenon (cf. Knauth and Kennedy 2009; Derry 2010; Zhao *et al.* 2020). In most cases, the SE immediately precedes the first appearance of macroscopic organisms (Xiao *et al.* 2016; Xiao and Narbonne 2020) with only one exception in NW Canada (Macdonald *et al.* 2013). Therefore, the SE may have played an important environmental role in the long evolution of animals (Darroch *et al.* 2018).

Despite its significance, direct mineralogical evidence of redox conditions in the form of oxidized phases – for example, the presence of sulfate minerals – is still limited. To actively search for the potential evidence of sulfate minerals within the SE, we evaluated 15 SE-equivalent sections distributed around the world, including the Doushantuo Formation in South China, the Shuram Formation in Oman, the Wonoka Formation in southern Australia, the Krol B + C intervals in northern India, the Nama Group in southern Namibia, the Rainstorm Member in the western USA, the upper Clemente Formation in northwestern Mexico, and the Nikol'skaya, Alyanchskaya and Kholychskaya formations in Siberia (Figs 1 and 2; Table 1). Our petrological investigation in this study is focused on the Doushantuo Formation in South China.

Our compilation (Tables 1–3) shows that many SE-equivalent sections do preserve mineralogical evidence of authigenic sulfate minerals and/or concentration enrichment in carbonate-associated sulfate ([CAS]). We further review stratigraphic trends in barium concentrations ([Ba]), and present new [Ba] data across three SE-equivalent sections, including the Doushantuo Formation at Yangjiaping in South China and the Clemente Formation at two localities in northwestern Mexico. Our findings suggest coupled C, S and Ba cycles in an increasingly oxygenated Earth surface environment during the SE, which may have played a pivotal role in the genesis of the largest globally recorded $\delta^{13}C$ negative excursion in Earth history.

Geological background

The Ediacaran Doushantuo Formation in the Yangtze block of South China overlies the Nantuo diamictite and begins with a *c.* 635 Ma Marinoan cap carbonate (Fig. 2) (Condon *et al.* 2005; Zhu *et al.* 2007*b*; Jiang *et al.* 2011). Stratigraphically overlying the Doushantuo Formation is the dolostone-dominated Dengying Formation. The age of the Doushantuo–Dengying boundary was originally constrained to be *c.* 551 Ma (Condon *et al.* 2005; Zhu *et al.* 2013), but was later proposed to be slightly older on the basis of a different stratigraphic correlation (An *et al.* 2015; see also Zhou *et al.* 2017 for a different interpretation). The more recent age constraints suggest that the SE probably terminated at *c.* 560 Ma (Gong and Li 2020; Rooney *et al.* 2020).

Deposition of the Doushantuo Formation in the Yangtze block can largely be divided into two stages, beginning with an open ramp shelf that gradually transitioned into a rimmed shelf protecting an intra-shelf basin (Jiang *et al.* 2011; Cui *et al.* 2015). Stratigraphic data and palaeogeographic reconstructions indicate an increase in water depth from proximal intertidal environments in the west and NW to distal deep basinal settings in the SE. Three platform facies belts have been proposed, including a proximal inner shelf dominated by peritidal carbonates, an intra-shelf basin containing mixed carbonates and shales, and a rimmed outer shelf shoal complex consisting of carbonates and phosphorites (Fig. 2) (Jiang *et al.* 2011). A more nuanced depositional model has also been proposed for the Doushantuo Formation, featuring two depositional mega-sequences and multiple stages of deposition (Zhu *et al.* 2007*b*; 2013; 2021).

The SE is widely reported from the upper Doushantuo Formation, which is also referred to as N3 (Negative 3) (Jiang *et al.* 2007; Wang *et al.* 2016), EN3 (Ediacaran Negative 3) (Zhou and Xiao 2007; McFadden *et al.* 2008) or DOUNCE (Doushantuo negative carbon isotope excursion) (Zhu *et al.* 2007*a*; 2013; Lu *et al.* 2013). Six sections of the Doushantuo Formation with the N3/EN3/DOUNCE (= SE) on top were investigated in this study, including the inner shelf Dongdahe section (Yunnan Province), the intra-shelf Jiulongwan section (Hubei Province), the outer shelf Yangjiaping, Zhongling and Nanbeizhen sections (Hunan Province) and the upper slope Siduping section (Hunan Province) (Figs 1 and 2; Table 2). The Nanbeizhen section is located very close to the Zhongling section to the SW. These broadly correlative sections represent a range of water depths from shallow to deeper environments. Chemostratigraphic studies reveal that the SE is recorded in the uppermost intervals of these sections, although the stratigraphic completeness of some successions has been questioned (Cui *et al.* 2015). Detailed investigations of these sections can be found in previously published papers on the Dongdahe section (Zhu *et al.* 2007*b*; Lu *et al.* 2013), the Jiulongwan section (Jiang *et al.* 2007; 2011; McFadden *et al.* 2008; Zhou *et al.* 2012; Ling *et al.* 2013; Zhu *et al.* 2013), the Zhongling and Yangjiaping sections (Zhu *et al.* 2007*b*; Jiang *et al.* 2011; Cui *et al.* 2015; 2017) and the Siduping section (Jiang *et al.* 2011; Wang *et al.* 2016; Li *et al.* 2017; Shi *et al.* 2018).

The inner-shelf Dongdahe section is located near the Dongdahe reservoir, 5 km east of Chengjiang county, Yunnan Province (Fig. 2b). The $\delta^{13}C$ profile of this section reveals a large negative excursion in the upper part of the Doushantuo Formation (i.e. DOUNCE) that has been correlated with the SE (Zhu *et al.* 2007*b*; Lu *et al.* 2013). Lenticular limestone beds with an edgewise structure in this section indicate frequent storm-wave influence in a shallow basin. The dark-grey dolomitic limestone shows distinct calcite pseudomorphs after gypsum (Fig. 3a, b), which are indicative of a restricted inner-shelf environment.

The EN3 interval at intra-shelf Jiulongwan has been further divided into EN3a, EN3b and EN3c on the basis of the characteristics of the $\delta^{13}C$ profiles (Fig. 1j) (McFadden *et al.* 2008). The EN3a interval shows a decrease in $\delta^{13}C$ from 0 to −9‰, whereas the EN3b shows largely consistent $\delta^{13}C$ values of *c.* −9‰. The EN3c interval represents a recovery of the SE from −9‰ to 0‰, as documented in carbonate concretions in Member IV black shales (McFadden *et al.* 2008). It should be noted that the basin-scale correlation of the Member IV shale interval at Jiulongwan (i.e.

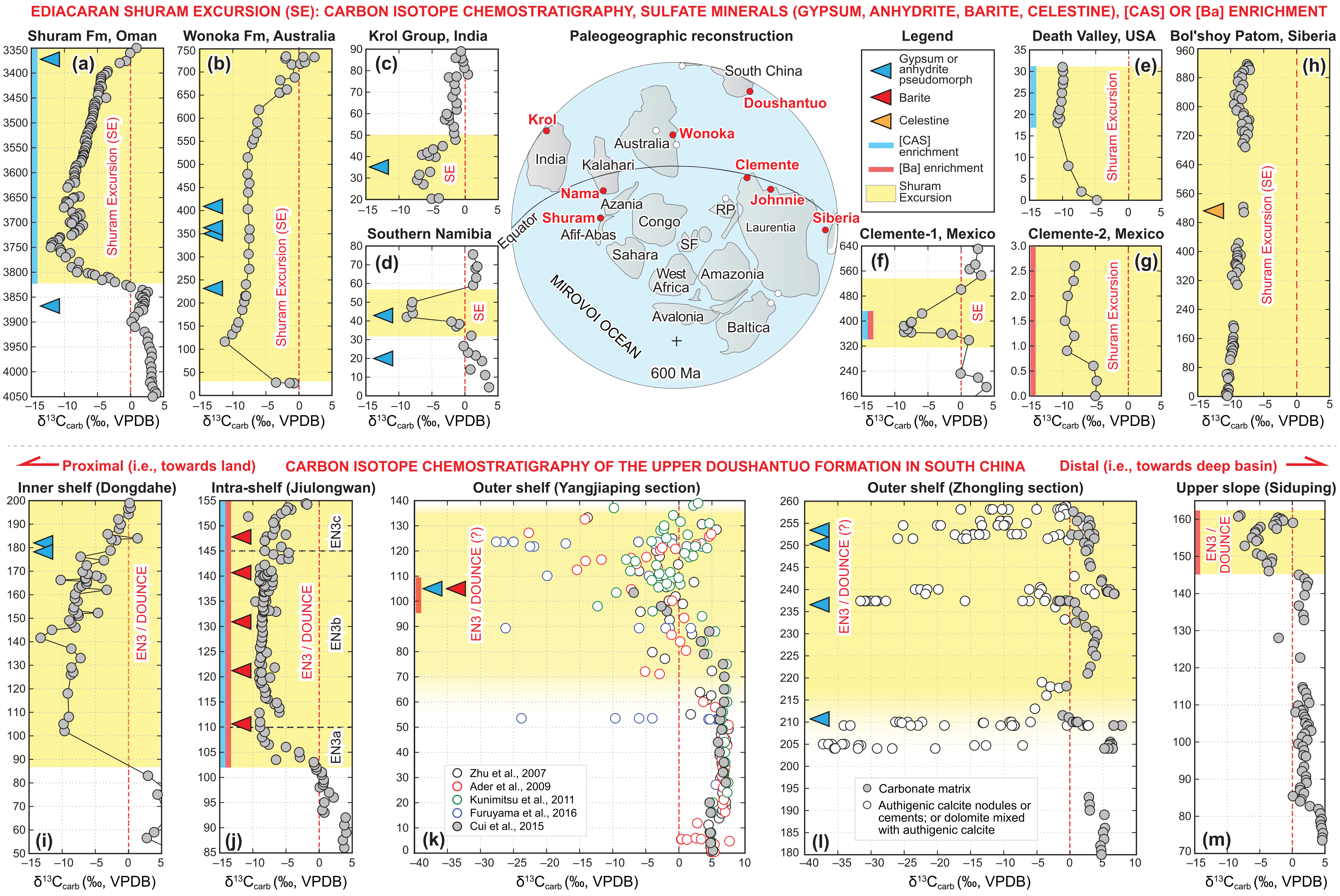
EDIACARAN SHURAM EXCURSION (SE): CARBON ISOTOPE CHEMOSTRATIGRAPHY, SULFATE MINERALS (GYPSUM, ANHYDRITE, BARITE, CELESTINE), [CAS] OR [Ba] ENRICHMENT
Shuram Fm, Oman
(a)
Shuram Excursion (SE)
Wonoka Fm, Australia
(b)
Shuram Excursion (SE)
Krol Group, India
(c)
SE
Southern Namibia
(d)
SE
Paleogeographic reconstruction
South China
Doushantuo
Krol
Wonoka
Australia
India
Kalahari
Clemente
Nama
Azania
Johnnie
Shuram
RP
Siberia
Afif-Abas
Congo
Laurentia
Equator
SF
Sahara
West Africa
Amazonia
MIROVOI OCEAN
Avalonia
Baltica
600 Ma
Legend
Gypsum or anhydrite pseudomorph
Barite
Celestine
[CAS] enrichment
[Ba] enrichment
Shuram Excursion
Death Valley, USA
(e)
Shuram Excursion
Clemente-1, Mexico
(f)
SE
Clemente-2, Mexico
(g)
Shuram Excursion
Bol'shoy Patom, Siberia
(h)
Shuram Excursion (SE)
δ13Ccarb (‰, VPDB)
−15 −10 −5 0 5
Proximal (i.e., towards land)
CARBON ISOTOPE CHEMOSTRATIGRAPHY OF THE UPPER DOUSHANTUO FORMATION IN SOUTH CHINA
Distal (i.e., towards deep basin)
Inner shelf (Dongdahe)
(i)
EN3 / DOUNCE
Intra-shelf (Jiulongwan)
(j)
EN3 / DOUNCE
EN3c
EN3b
EN3a
Outer shelf (Yangjiaping section)
(k)
EN3 / DOUNCE (?)
Zhu et al., 2007
Ader et al., 2009
Kunimitsu et al., 2011
Furuyama et al., 2016
Cui et al., 2015
−40 −35 −30 −25 −20 −15 −10 −5 0 5 10
Outer shelf (Zhongling section)
(l)
EN3 / DOUNCE (?)
Carbonate matrix
Authigenic calcite nodules or cements; or dolomite mixed with authigenic calcite
Upper slope (Siduping)
(m)
EN3 / DOUNCE
δ13Ccarb (‰, VPDB)

Fig. 1 Carbonate carbon isotope ($\delta^{13}C_{carb}$) chemostratigraphy, sulfate mineral distribution and [CAS] or [Ba] enrichment of the Ediacaran SE. The SE in the upper Doushantuo Formation of South China is also widely referred to as EN3 (Jiang *et al.* 2007; Zhou and Xiao 2007; McFadden *et al.* 2008) or DOUNCE (Zhu *et al.* 2007*a*; 2013; Lu *et al.* 2013). The *y* axes of all sections represent the thickness in metres. Yellow background shading shows SE/EN3/DOUNCE intervals. Blue triangles mark the horizons with potential gypsum ($CaSO_4 \cdot 2H_2O$) or anhydrite ($CaSO_4$). Red triangles mark the horizons with authigenic barite ($BaSO_4$). The orange triangle represents celestine ($SrSO_4$). Field and petrographic images of these marked sulfate-bearing intervals can be found in Figures 3–13. (**a**) Shuram Formation of the Miqrat-1 drill hole in the South Oman Salt Basin, Oman. (**b**) Wonoka Formation, Bunyeroo Gorge section, Southern Australia. (**c**) Krol Group at the Nigalidhar section. (**d**) Nama Group, Grens section, Witputs Sub-Basins, Namibia. (**e**) Rainstorm Member at Winters Pass Hills, Death Valley, western USA. (**f**) Upper Clemente Formation at the CR-1 section, Cerro Rajón, Sonora State, Mexico. (**g**) Upper Clemente Formation at the CR-2 section, Cerro Rajón, Sonora State, Mexico. (**h**) Nikol'skaya, Alyanchskaya, and Kholychskaya formations, Bol'shoy Patom section, Siberia, Russia. (**i–m**) Broadly correlative sections of the upper Doushantuo Formation that record EN3/DOUNCE in South China. Sections are listed from left (towards land) to right (towards the deep basin). (**i**) Upper Doushantuo Formation at the inner-shelf Dongdahe section. (**j**) Upper Doushantuo Formation at the intra-shelf Jiulongwan section. (**k**) Upper Doushantuo Formation at the outer-shelf Yangjiaping section. (**l**) Upper Doushantuo Formation at the outer-shelf Zhongling section. (**m**) Upper Doushantuo Formation at the upper-slope Siduping section. The palaeogeographic map shows the locatilites of Shuram sections at the global scale. Key sections for the SE are indicated by filled circles (Shuram; Wonoka; Doushantuo; Johnnie; Clemente; Nama; Siberia) and the positions of other potential sections that may correlate with the SE are shown as open circles. Red circles represent the localities discussed in this study. RP, Rio de La Plata; SF, São Francisco. The map is modified from Pisarevsky *et al.* (2008); Grotzinger *et al.* (2011), and Gong and Li (2020). The $\delta^{13}C$ data are from: Shuram Formation (Fike *et al.* 2006); Wonoka Formation (Calver 2000); Krol Group (Kaufman *et al.* 2006); Nama Group (Wood *et al.* 2015); Rainstorm Member (Kaufman *et al.* 2007); Clemente Formation (Loyd *et al.* 2012, 2013); Siberia (Melezhik *et al.* 2009); Doushantuo at Dongdahe (Zhu *et al.* 2007*b*; Lu *et al.* 2013); Doushantuo at Jiulongwan (Jiang *et al.* 2007; McFadden *et al.* 2008); Doushantuo at Yangjiaping (Zhu *et al.* 2007*b*; Ader *et al.* 2009; Kunimitsu *et al.* 2011; Cui *et al.* 2015; Furuyama *et al.* 2016); Doushantuo at Zhongling (Cui *et al.* 2015, 2017); Doushantuo at Siduping (Li *et al.* 2017). Source of sulfate minerals: Khufai Formation at the WS section (Le Guerroué 2006); Wonoka Formation (Calver 2000); Krol Group (Jiang *et al.* 2002); Nama Group (Kaufman *et al.* 2015; Wood *et al.* 2015; this study); Siberia (Melezhik *et al.* 2009); Doushantuo at Dongdahe (Lu *et al.* 2013); Doushantuo at Jiulongwan (Cui *et al.* 2017; this study); Doushantuo at Yangjiaping (Cui *et al.* 2016*a*; this study); Doushantuo at Zhongling (Cui *et al.* 2017; this study). The concentration enrichment data are from: [CAS] enrichment in the Shuram Formation (Fike *et al.* 2006); [CAS] enrichment in the Rainstorm Member (Kaufman *et al.* 2007); [Ba] enrichment in the Clemente Formation (this study); [CAS] enrichment at Jiulongwan (McFadden *et al.* 2008; Li *et al.* 2010; Shi *et al.* 2018); [Ba] enrichment at Jiulongwan (Cui *et al.* 2017; Zhang *et al.* 2019; Wei *et al.* 2021*b*); [Ba] enrichment at Siduping (Cao *et al.* 2020). See Appendix A for abbreviations.

EN3c) has been questioned, and appears to be increasingly controversial (An *et al.* 2015; Zhou *et al.* 2017; Bridger *et al.* 2021).

A striking feature of the upper Doushantuo Formation at Zhongling and Yangjiaping is the occurrence of strongly ^{13}C-depleted authigenic calcite nodules and cements with carbonate $\delta^{13}C$ ($\delta^{13}C_{carb}$) values down to −37‰ (Fig. 1k, l) (Macouin *et al.* 2004; Ader *et al.* 2009; Kunimitsu *et al.* 2011; Furuyama *et al.* 2016; Cui *et al.* 2016*a*; 2017). It is notable that similar methane-derived $\delta^{13}C_{carb}$ signals have also been reported from the cap carbonate interval in the basal Doushantuo Formation, with controversial origins that could be either early authigenic (Jiang *et al.* 2003*a*; 2006*a*; 2006*b*; Wang *et al.* 2008; Peng *et al.* 2015; Zhou *et al.* 2016) or post-depositional (Bristow *et al.* 2011; Lin *et al.* 2011; Cui *et al.* 2019*c*). In contrast, based on multiple lines of sedimentological and geochemical evidence, the authigenic calcite in the upper Doushantuo Formation of outer shelf sections has been interpreted as an early diagenetic phase formed in shallow marine sediments (Macouin *et al.* 2004; 2012; Ader *et al.* 2009; Furuyama *et al.* 2016; Cui *et al.* 2016*a*; 2017). Our conceptual model in this study on biogeochemical S and Ba cycles during the SE is independent of the interpretations of these enigmatic methane-derived calcites.

The precise stratigraphic position of the EN3/DOUNCE interval at Zhongling and Yangjiaping remains unclear. Given the much more scattered and expanded $\delta^{13}C_{carb}$ values (including methane-derived signals) in the upper part of these two sections (Fig. 1k, l), it is challenging to pinpoint the EN3 or SE using the $\delta^{13}C_{carb}$ profiles alone. It has recently been proposed that the highly negative $\delta^{13}C_{carb}$ signals may represent an atypical expression of the SE in response to various local redox conditions across the basin (Cui *et al.* 2017; 2019*b*). The potential for a stratigraphic hiatus has also been proposed in the upper part of the Doushantuo Formation (Kaufman 2005; Zhu *et al.* 2007*b*; Cui *et al.* 2015; Zhou *et al.* 2017). Nevertheless, this uncertainty in the exact chemostratigraphic correlation does not affect the interpretation presented here.

In addition to the Doushantuo Formation in South China, we also evaluate mineralogical and geochemical data in correlative sections worldwide (Fig. 1; Table 2). Detailed geological descriptions and chemostratigraphy of these sections have been published for the Wonoka Formation in South Australia (Calver 2000), the Clemente Formation in northwestern Mexico (Stewart *et al.* 1984; Loyd *et al.* 2012; 2013; Li *et al.* 2020*b*), the Nama Group in southern Namibia (Wood *et al.* 2015), the Johnnie Formation in the western USA (Corsetti and Kaufman 2003; Kaufman *et al.* 2007; Bergmann *et al.* 2011), the Krol Group in northern India (Jiang *et al.* 2002; 2003*b*) and the Nikol'skaya, Alyanchskaya and Kholychskaya formations in the Bol'shoy Patom section, Siberia, Russia (Melezhik *et al.* 2009; Zhang *et al.* 2019).

Samples and methods

Sample sets

In this study, ten samples from the EN3/DOUNCE interval of the upper Doushantuo Formation at Jiulongwan were examined for sulfate minerals or pseudomorphs after sulfates. Each sample was prepared as a 2.5-mm-diameter glass thin section or epoxy mount for detailed secondary ion mass spectrometry (SIMS)-SEM investigation. Detailed SIMS results of these ten samples can be found in Cui *et al.* (2021). Among the ten samples, four reveal the presence of diagenetic barite (Table 2). The sample numbers and stratigraphic positions of these four barite-bearing samples are SSFT39.6 (110.6 m), HND9.1 (121.9 m), HND18.05 (130.9 m) and HND27.75 (140.55 m). Together, they cover the full range of the EN3b interval of the Jiulongwan section (Fig. 1j).

In addition to a mineralogical investigation, we also present new [Ba] data for three SE-equivalent sections, including the upper Clemente Formation at the CR-1 and CR-2 sections, northwestern Mexico (Fig. 1f, g), and the upper Doushantuo Formation at the outer shelf Yangjiaping section (Fig. 1k), South China. The Yangjiaping and Clemente sample sets for [Ba] analysis were described in the studies by Zhu *et al.* (2007*b*) and Loyd *et al.* (2012), respectively.

SEM

The thin sections and epoxy mounts of the Jiulongwan EN3/DOUNCE samples in this study were prepared at the Department of Geoscience, University of Wisconsin–Madison. Petrographic

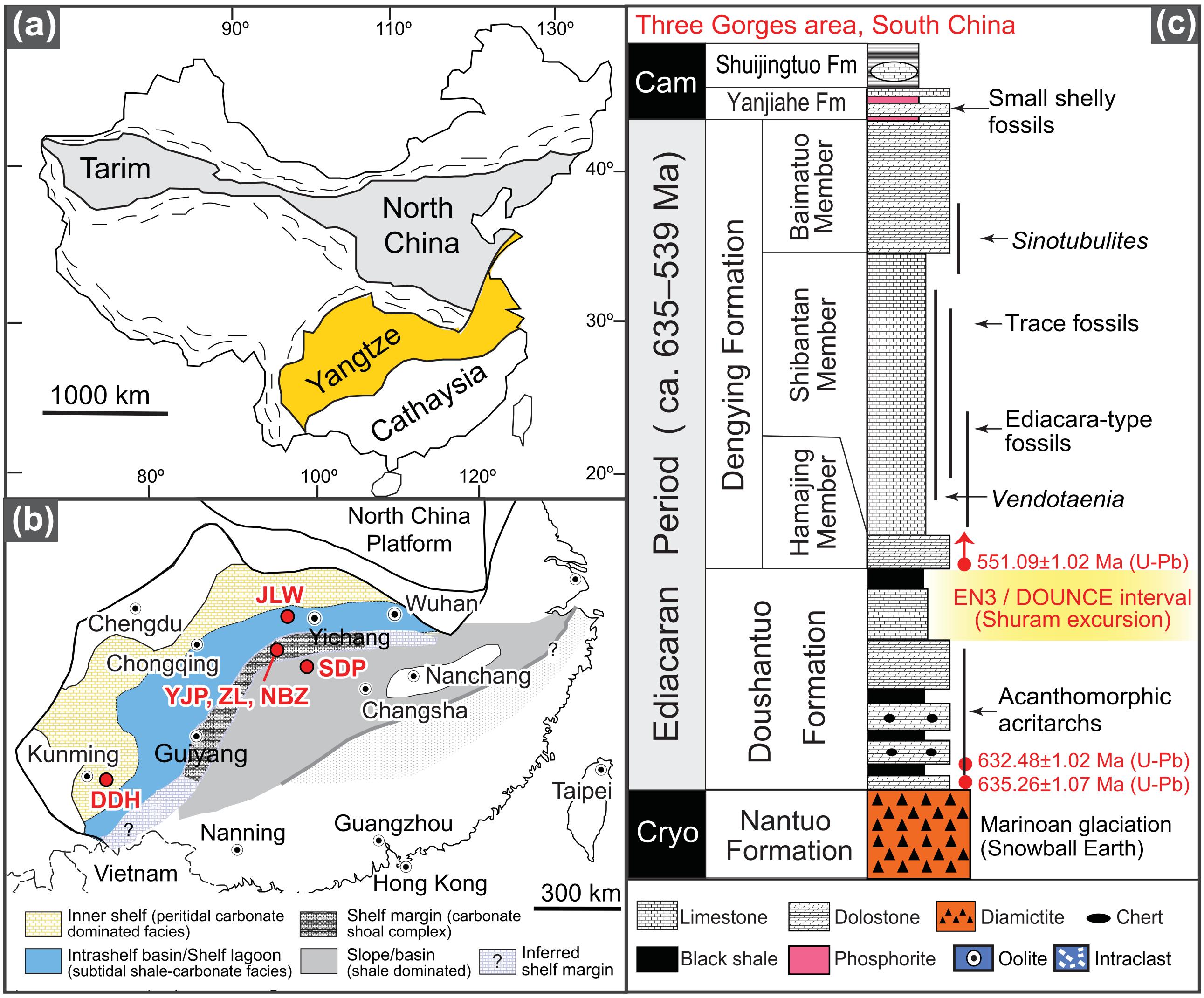

Fig. 2 Maps and stratigraphic columns. (**a**) Geological map of China, with the Yangtze block in yellow. (**b**) Reconstructed Ediacaran depositional environments on the Yangtze block (Jiang *et al.* 2011). Red dots denote the locations of upper Doushantuo sections discussed in this study (see Appendix A for abbreviations). (**c**) Simplified litho-, bio- and chrono-stratigraphy of the Ediacaran Doushantuo and Dengying formations in South China. The yellow highlighted interval shows the stratigraphic position of EN3/DOUCE, which is correlative to the SE on a global scale. Thickness is not to scale. Note that the 551 Ma age was initially placed at the Doushantuo–Dengying boundary by Condon *et al.* (2005), but was later reassigned to the Shibantan Member of the Dengying Formation on the basis of a more recent chemostratigraphic study (An *et al.* 2015), although it remains a matter of debate (Zhou *et al.* 2017). Figure modified from Chen *et al.* (2013) and Cui *et al.* (2017). Radiometric ages are from Condon *et al.* (2005) and Schmitz (2012).

imaging was conducted in the SEM and energy-dispersive spectrometry (EDS) laboratory at the PARI (Plateforme d'Analyses haute Résolution) platform of IPGP (Institut de Physique du Globe de Paris), Université de Paris. Backscattered electron (BSE) images of samples were acquired with an SEM EVO MA10 Zeiss coupled with EDS. SEM images were acquired using an accelerating voltage of 15 keV at a working distance of *c.* 10 mm. Currents of 30 and 3 nA were used for mapping and quantitative analysis, respectively.

Micro X-ray fluorescence

High-resolution elemental abundance maps of the polished sample surfaces were produced using the M4 Tornado micro X-ray fluorescence (µXRF) scanner (Bruker nano GmbH, Berlin, Germany) at the Vrije Universiteit Brussel, Belgium. The µXRF mapping was performed along a 2D grid with 25 µm spacing, a spot size of 25 µm and an integration time of 1 ms per pixel. The X-ray source was operated under maximum energy settings (600 µA, 50 kV) with no source filters. This µXRF mapping approach resulted in qualitative element concentration distributions in the form of elemental maps.

[Ba] analyses

The [Ba] of three SE-equivalent sections are newly analysed in this study, including the upper Clemente Formation at the CR-1 and CR-2 sections, Mexico (Fig. 2f, g), and the upper Doushantuo Formation at the outer shelf Yangjiaping section, South China (Fig. 2j). The [Ba] of both formations was analysed via dilute acid extraction: 0.4 M HNO_3 for the Doushantuo Formation and 1 M HCl for the Clemente Formation. Detailed analytical methods of the [Ba] analyses follow the studies of Liu *et al.* (2016) and Liu *et al.* (2021) for the Doushantuo samples, and Zhang *et al.* (2019) for the Clemente samples.

Different concentrations of acid can extract barium phases (e.g. carbonate-associated barium, witherite, barite) to different degrees. To better evaluate the [Ba] data of SE-equivalent sections, we compared the different methods used for [Ba] analyses in published studies (Table 4). In this study, all of our plotted [Ba] data were determined through dissolution using dilute acids with concentration <1 M (shown as $[\mathrm{Ba}]_{\mathrm{dilute\ acid}}$ hereafter). In what follows we tentatively set a somewhat arbitrary threshold value of $[\mathrm{Ba}]_{\mathrm{dilute\ acid}}$ = 50 ppm to differentiate background (<50 ppm) and elevated (>50 ppm) [Ba] throughout the text.

Table 1 *Sulfate mineral content and [CAS] and [Ba] enrichment in the sections of the Ediacaran SE investigated in this study*

Section	SE	Stratigraphy	Section	Palaeoenvironment	$\delta^{13}C_{carb}$ profile	Nadir $\delta^{13}C$ value (VPDB)	Sulfate minerals or textures	[CAS] enrichment	[Ba] enrichment	Sources
1	Oman	Shuram Fm	Miqrat-1 drill hole	Carbonate ramp	Figure 1a	−12.0‰	N.A.	✓	N.A.	(Fike *et al.* 2006)
2	Australia	Wonoka Fm	Bunyeroo Gorge	Shallow shelf	Figure 1b	−11.2‰	✓	N.A.	N.A.	(Calver 2000)
3	India	Krol B and C intervals	Nigalidhar	Shallow subtidal to carbonate sand shoal	Figure 1c	−8.8‰	✓	N.A.	N.A.	(Jiang *et al.* 2002)
4	Namibia	Kanies and Mara members, Dabis Fm, Nama Group	Grens	Shallow inner ramp	Figure 1d	−7.2‰	✓	N.A.	N.A.	(Wood *et al.* 2015)
5	Namibia	Mara Member, Dabis Fm, Nama Group	Pockenbank	Carbonate ramp	N.A.	N.A.	✓	N.A.	N.A.	This study
6	USA	Rainstorm Member, Johnnie Fm	Winters Pass Hills	Carbonate ramp	Figure 1e	−10.8‰	N.A.	✓	N.A.	(Kaufman *et al.* 2007)
7	Mexico	Upper Clemente Fm	CR-1 section	Carbonate shoal	Figure 1f	−8.6‰	N.A.	✓	✓	(Loyd *et al.* 2012, 2013); This study
8	Mexico	Upper Clemente Fm	CR-2 section	Carbonate shoal	Figure 1g	−9.6‰	N.A.	N.A.	✓	(Loyd *et al.* 2012, 2013); This study
9	Russia	Nikol'skaya, Alyanchskaya, and Kholychskaya fms	Bol'shoy Patom section	Carbonate ramp and peritidal rimmed shelf	Figure 1h	−10.7‰	✓	N.A.	N.A.	(Melezhik *et al.* 2009)
10	China	Upper Doushantuo Fm	Dongdahe	Inner shelf	Figure 1i	−13.3‰	✓	✓	✓	(Zhu *et al.* 2007*b*; Lu *et al.* 2013)
11	China	Upper Doushantuo Fm	Jiulongwan	Intra-shelf	Figure 1j	−9.0‰	✓	✓	✓	(McFadden *et al.* 2008); This study
12	China	Upper Doushantuo Fm	Yangjiaping	Rimmed outer-shelf shoal	Figure 1k	−27.6‰	✓	N.A.	✓	(Macouin *et al.* 2004, 2012; Ader *et al.* 2009; Cui *et al.* 2015, 2016*a*, 2017; Furuyama *et al.* 2016); This study
13	China	Upper Doushantuo Fm	Zhongling	Rimmed outer-shelf shoal	Figure 1l	−37.2‰	✓	N.A.	N.A.	(Cui *et al.* 2017); This study
14	China	Upper Doushantuo Fm	Nanbeizhen	Rimmed outer-shelf shoal	N.A.	N.A.	✓	N.A.	N.A.	This study
15	China	Upper Doushantuo Fm	Siduping	Upper slope	Figure 1m	−8.3‰	N.A.	N.A.	✓	(Li *et al.* 2010; Shi *et al.* 2018; Cao *et al.* 2020); This study

Fm, Formation; N.A., not available.

Table 2 *Sections of the upper Doushantuo Formation in South China*

Part of the Doushantuo Formation	Original sample code (McFadden *et al.* 2008)	Sample number (Cui *et al.* 2021)	Height above Nantuo diamictite (m)	Stratigraphic position	Lithology	$\delta^{13}C_{carb}$ (VPDB)	Sulfate minerals	[CAS] enrichment	[Ba] enrichment
Inner-shelf Dongdahe section (Fig. 1i)			N.A.	Uppermost Doushantuo Fm	Limestone and dolostone	−2.7‰	Pseudomorph of evaporite minerals (Fig. 3a, B)	N.A.	N.A.
Intra-shelf Jiulongwan section (Fig. 1j)	SSFT39.6	Sample S4	110.6	EN3b, Mb. III	Dolomitic limestone	−8.9‰	Diagenetic barite, disseminated pyrite (Fig. 10)	✓	✓
	HND9.1	Sample S5	121.9	EN3b, Mb. III	Dolomitic limestone	−9.1‰	Diagenetic barite, disseminated and euhdral pyrite (Fig. 11)		
	HND18.05	Sample S7	130.9	EN3b, Mb. III	Dolomitic limestone	−8.6‰	Barite, pyrite pseudomorphs of evaporite minerals (Figs 9 and 12)		
	HND27.75*	Sample S8	140.55	EN3b, Mb. III	Dolomitic limestone	−8.4‰	Barite veins, disseminated (Fig. 13)		
	N.A.	N.A.	145–155	EN3b, Mb. IV	Shale with early diagenetic carbonate nodules	*c.* −5.0‰	Authigenic barite crystal fans surrounding early diagenetic carbonate nodules (Fig. 3e and f)		
Outer-shelf Yangjiaping section (Fig. 1k)				Uppermost Doushantuo Fm	Limestone and phosphorite	*c.* −5.0‰	Calcite nodules and lenses after gypsum; chicken-wire texture (Fig. 4f–h,7)	N.A.	✓
Outer-shelf Zhongling section (Fig. 1l)				Uppermost Doushantuo Fm	Dolostone and phosphorite	*c.* −7.3 to −26.0‰	Calcite nodules and lenses after gypsum; chicken-wire texture (Fig. 4d–e,6, 7)	N.A.	N.A.
Outer-shelf Nanbeizhen section				Uppermost Doushantuo Fm	Carbonate and phosphorite	N.A.	Calcite nodules and lenses after gypsum (Fig. 4a–c)	N.A.	N.A.
Upper-slope Siduping section (Fig. 2m)				Uppermost Doushantuo Fm	Carbonates	−7.3‰	N.A.	N.A.	✓

*There are no micro-drilled data for sample HND27.75. The value of −8.4‰ presented in the table was measured from sample HND 27.1, which is stratigraphically 0.6 m below sample HND27.75. More petrographic results for sulfate minerals are available in the Supplementary material.

Table 3 *Global distribution of sulfate minerals in Ediacaran and early Cambrian strata*

Period	Sulfate minerals	Stratigraphy	Country	Source
Early Cambrian				
Early Cambrian	Barite nodules	Yurtus Fm	China	(Zhou *et al.* 2015)
Early Cambrian	Barite and witherite deposits	Liujiaping Fm	China	(Wang and Li 1991; Xu *et al.* 2016)
Early Cambrian	Gypsum and barite	Niutitang Fm	China	(Tang *et al.* 2014)
Ediacaran (after the SE)				
Ediacaran (post-SE)	Calcite pseudomorphs after gypsum	Gaojiashan Member, Dengying Fm	China	(Cui *et al.* 2016*c*, 2019*a*)
Ediacaran (post-SE)	Celestine and abundant organic sulfur	Shibantan Member, Dengying Fm	China	(Matsu'ura *et al.* 2021)
Late Ediacaran (post-SE)	Calcite pseudomorphs after gypsum	Algal Dolomite Member, Dengying Fm	China	(Ding *et al.* 2019)
Ediacaran (post-SE)	Calcite pseudomorphs after gypsum; collapse breccia and dissolution vugs of former evaporites	Hamajing and Baimatuo members, Dengying Fm	China	(Duda *et al.* 2015)
Ediacaran (post-SE)	Platy and acicular gypsum	Dengying Fm	China	(Peng *et al.* 2017)
Ediacaran (post-SE)	Calcite pseudomorphs after gypsum and anhydrite	Dengying Fm	China	(Luo *et al.* 2017)
Ediacaran to early Cambrian (post-SE)	Anhydrite	Hormuz evaporites	Iran, Qatar, UAE and Saudi Arabia	(Smith 2012)
Ediacaran to early Cambrian (post-SE)	Anhydrite	Hansen Evaporite Group/ Salt Range Fm	Pakistan and India	(Smith 2012)
Ediacaran to early Cambrian (post-SE)	Anhydrite	Ara Group	Oman	(Fike and Grotzinger 2008, 2010; Smith 2012; Grotzinger and Al-Rawahi 2014)
Ediacaran (post-SE)	Fenestrae with gypsum, or partially filled with mega-quartz with anhydrite inclusions	Buah Fm	Oman	(Wright *et al.* 1990)
Ediacaran (post-SE)	Gypsum pseudomorphs with swallowtail morphologies; fenestral mudstone with spar-filled fenestrae and anhydrite laths or gypsum rosettes	Buah Fm	Oman	(Bergmann 2013; Cantine *et al.* 2020)
Ediacaran (post-SE)	Calcite or chert pseudomorphs after anhydrite	Buah Fm	Oman	(Gorin *et al.* 1982)
During the SE				
Ediacaran (SE)	Gypsum	Wonoka Fm	Australia	(Calver 2000), Figure 5a and b
Ediacaran (SE)	Evaporite crystals	Uppermost Doushantuo Fm at Dongdahe	China	(Lu *et al.* 2013); This study (Fig. 3a and b)
Ediacaran (SE)	Barite crystal fans; diagenetic barite cements or veins; pyrite pseudomorphs of evaporites	Uppermost Doushantuo Fm at Jiulongwan	China	(Cui *et al.* 2017); This study (Figs 3c, d, 8–13)
Ediacaran (SE)	Sulfate dominated by CAS, with a minor contribution from gypsum (based on XANES analysis)	Uppermost Doushantuo Fm, Three Gorges section	China	(Matsu'ura *et al.* 2021)
Ediacaran (SE)	Calcite lenses and nodules after gypsum	Uppermost Doushantuo Fm at Nanbeizhen (close to Zhongling)	China	This study (Fig. 4a–c)
Ediacaran (SE)	Barite cement; calcite lenses and nodules after gypsum	Uppermost Doushantuo Fm at Yangjiaping and Zhongling	China	(Cui *et al.* 2016*a*); This study (Figs 4 and 7)
Ediacaran (SE)	Calcified chicken-wire texture	Uppermost Doushantuo Fm at Zhongling and Yangjiaping	China	(Cui *et al.* 2017); This study (Fig. 6)
Ediacaran (SE)	Gypsum cast	Krol B, Krol Group	India	(Jiang *et al.* 2002)
Ediacaran (SE)	Calcified gypsum nodule	Mara Member, Nama Group, Pockenbank	Namibia	(Kaufman *et al.* 2015); This study (Fig. 5)
Ediacaran (SE)	Evaporitic texture	Mara Member, Grens section:	Namibia	(Wood *et al.* 2015)
Ediacaran (SE)	Celestine and strontianite in oolitic limestone	Alyanchskaya Fm	Russia	(Melezhik *et al.* 2009)
Ediacaran (SE)	Desiccation cracks and probable evaporite casts	Rainstorm Member, Johnnie Fm	USA	(Summa 1993)
Before the SE (pre-SE)				
Ediacaran (pre-SE)	Silicified anhydrite rosettes with anhydrite inclusions	Khufai Fm	Oman	(Wright *et al.* 1990)
Ediacaran (pre-SE)	Centimetre-thick lenses of chertified evaporite	Khufai Fm	Oman	(Le Guerroué 2006), (Fig. 5j)

(continued)

Table 3 *(Continued)*

Period	Sulfate minerals	Stratigraphy	Country	Source
Ediacaran (pre-SE)	Fenestral mudstone with evaporite lathes; silicified beds with evaporite molds	Khufai Fm	Oman	(Osburn *et al.* 2014)
Ediacaran (pre-SE)	Evaporite collapse breccias associated with anhydrite	Khufai Fm	Oman	(Gorin *et al.* 1982)
Ediacaran (pre-SE)	Barite nodules	Doushantuo Fm (Member II)	China	This study
Early Ediacaran	Barite mamelons and veins	Jbéliat Group (cap carbonate)	Mauritania	(Shields *et al.* 2007)
Early Ediacaran	Barite fans	Doushantuo Fm (cap carbonate)	China	(Bao *et al.* 2008; Zhou *et al.* 2010; Peng *et al.* 2011; Killingsworth *et al.* 2013)
Early Ediacaran	Barite fans	Sete Lagoas Fm (cap carbonate)	Brazil	(Crockford *et al.* 2018; Okubo *et al.* 2020)
Early Ediacaran	Dolomite pseudomorph after gypsum	Puga cap carbonate	Brazil	(Santos *et al.* 2021)
Early Ediacaran	Barite fans	Ravensthroat Fm (cap carbonate)	Canada	(Macdonald *et al.* 2013; Crockford *et al.* 2016)
Early Ediacaran	Barite fans	Nyborg Fm (cap carbonate)	Norway	(Crockford *et al.* 2018)
Early Ediacaran	Barite fans	Ol Fm (cap carbonate)	Mongolia	(Bold *et al.* 2016)

XANES, X-ray absorption near-edge structure.

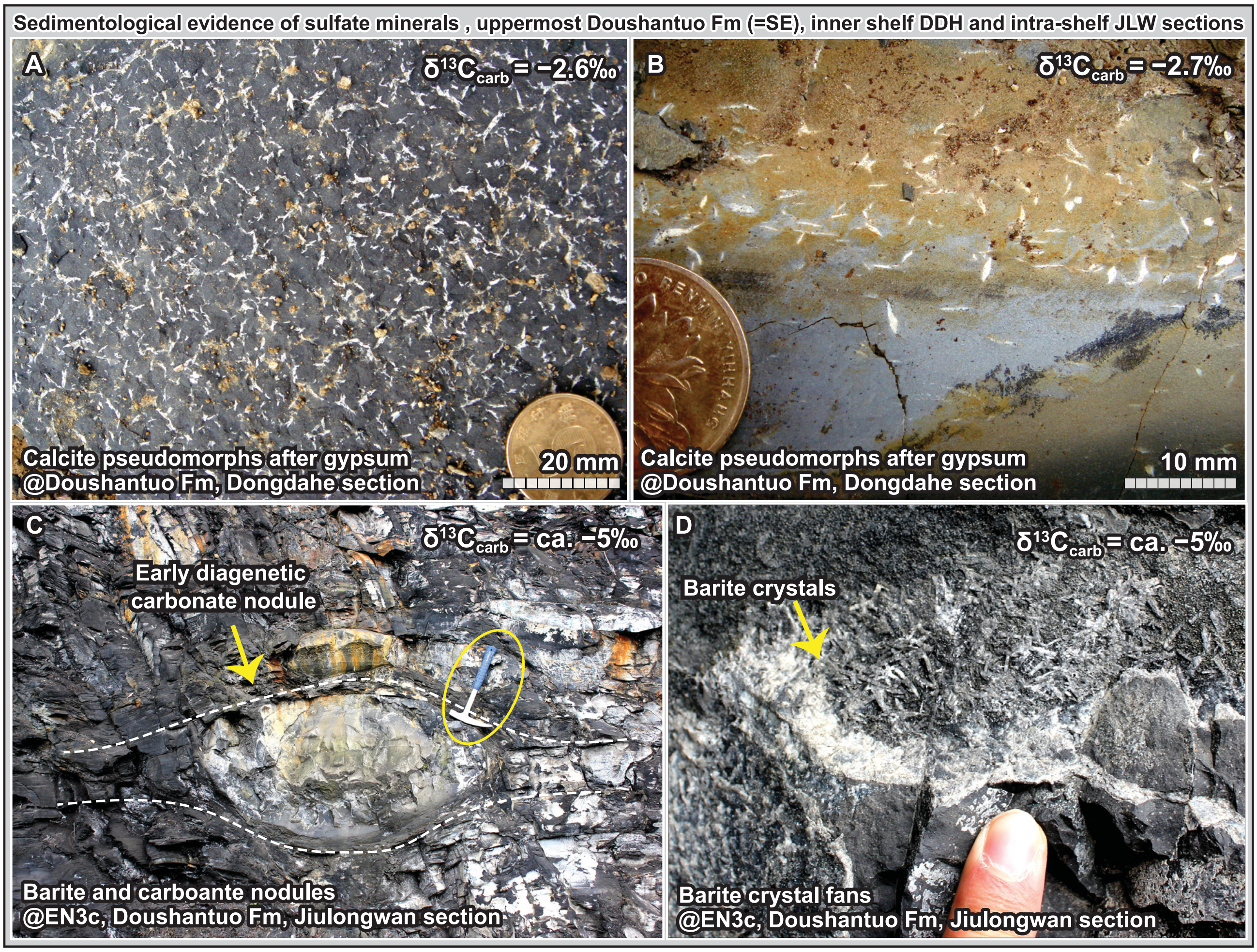

Fig. 3 Sedimentological evidence of sulfate minerals in the SE-equivalent upper Doushantuo Formation, inner-shelf Dongdahe section and intra-shelf Jiulongwan section, South China. The stratigraphic positions of these sulfate minerals can be found in Figure 1i (Dongdahe) and Figure 1j (Jiulongwan). (**a**, **b**) Massive gypsum cements in the uppermost Doushantuo Formation at the inner-shelf Dongdahe section, Yunnan Province, South China. Coin for scale (20.5 mm in diameter). (**c**) Field image showing a metre-scale carbonate nodule (arrow) in the Member IV shale interval of the Doushantuo Formation at Jiulongwan. Geological hammer for scale. Note the warping laminations surrounding the carbonate nodule, indicating that this nodule is syndepositional, and formed before sediment compaction. (**d**) Massive barite crystals (arrow) surrounding the carbonate nodule shown in (**c**). Images are from: **a** and **b** (Zhu *et al.* 2007*b*; Lu *et al.* 2013); **c** and **d** (Cui *et al.* 2017). See Appendix A for abbreviations.

Compilation of sulfate minerals

In this study, we actively searched for sulfate minerals in 15 SE-equivalent sections worldwide (Table 1). Both published results (e.g. EN3/DOUNCE at the Dongdahe section, Wonoka at the Bunyeroo Gorge section) and new results (e.g. all the SEM and µXRF images in this study) are compiled (Tables 1–3). Owing to the high solubility of gypsum and anhydrite in Earth surface environments, direct evidence for gypsum or anhydrite precipitates in SE-equivalent strata has not been found. Instead, we found a variety of pseudomorphs or textures that are indicative of original sulfate mineral precipitation, as summarized below (Figs 3–13). Our compilation is based on both literature surveys and lab investigations, with the latter primarily focused on the Doushantuo Formation in South China.

Doushantuo Formation at the inner shelf

Calcite pseudomorphs of evaporite minerals have been reported in carbonate intervals of the uppermost Doushantuo Formation at the inner-shelf Dongdahe section (Figs 1i, 3a, b) (Lu *et al.* 2013). The $\delta^{13}C_{carb}$ profile of the upper Doushantuo Formation at Dongdahe shows a large negative excursion from +5‰ down to −13.3‰ (Fig. 1i) (Zhu *et al.* 2007*b*; Lu *et al.* 2013), suggesting a correlation between sulfate minerals and the SE.

Doushantuo Formation at the outer shelf

The chemostratigraphy of the uppermost Doushantuo Formation at the outer-shelf Zhongling and Yangjiaping sections has been established in multiple published studies (Fig. 1k, l) (Zhu *et al.* 2007*b*; Ader *et al.* 2009; Kunimitsu *et al.* 2011; Cui *et al.* 2015; Furuyama *et al.* 2016). Calcite nodules and lenses have been found at three outer-shelf sections, including the Zhongling, Yangjiaping and Nanbeizhen sections in Hunan Province, South China (Fig. 4). Constraining the origin and paragenesis of these calcite nodules and lenses requires detailed field observations and fabric-specific geochemical analysis. These calcite nodules and lenses are typically horizontally aligned with respect to the sedimentary bedding surface, and are not associated with any late cross-cutting veins. The Nanbeizhen section notably preserves delicate textures with calcite lenses surrounded by fine warping phosphatic dolomite laminations (Figs 4a–c, S1–2), which strongly suggest that these lenses were formed before sediment compaction. Most, if not all, of the calcite nodules and lenses show silica rims. The silica rims often preserve elongate crystal shapes that are probably pseudomorphs of pre-existing sulfate minerals (Fig. 7). Extremely negative $\delta^{13}C_{carb}$ values down to *c.* −37‰ (VPDB), as well as $^{87}Sr/^{86}Sr$ ratios that fall within the typical Ediacaran seawater values (*c.* 0.7080 to 0.7083; see fig. 17 in Cui *et al.* 2020), were found in these authigenic calcite nodules and lenses. These observations suggest a significant carbon contribution from the oxidation of biogenic methane during early diagenesis (Cui *et al.* 2017).

At the Zhongling and Yangjiaping sections, chicken-wire textures indicative of original gypsum precipitation were observed in phosphatic carbonates (Fig. 6). This mosaic texture of loaded and compressed nodular gypsum in some samples (Fig. 6a–f, i–o) is typical in evaporative environments (Hardie 2003). Elemental maps produced by µXRF reveal the white-coloured phase to be calcite, often cemented by quartz as the ‘chicken wire’ (Fig. 6j–o). In addition, discrete horizontal layers of calcite with vertically aligned boundaries have also been found (Fig. 6g, h), which resemble the so-called ghost gypsum texture and indicate a subaqueous gypsum precursor (Warren 2016).

Petrographic observations via optical microscopy reveal barite crystal fans and quartz pseudomorphs of sulfate minerals (Fig. 7). It has been noted that, ‘gypsum, celestite, and barite can be extremely

Table 4 *Summary of the dissolution methods used to analyse [Ba] and [CAS] during the Ediacaran SE*

Concentration	Acid used for sample dissolution	Stratigraphy	Country	Chemostratigraphy	Data source
[CAS]	6 M HCl	Shuram Fm	Oman	Figure 14b	(Fike *et al.* 2006)
[CAS]	3 M HCl	Upper Doushantuo Fm at Jiulongwan	China	Figure 14f	(McFadden *et al.* 2008; Li *et al.* 2010)
[CAS]	4 M HCl	Upper Doushantuo Fm at Siduping	China	Figure 14j	(Shi *et al.* 2018)
[CAS]	3 M HCl	Upper Clemente Fm	Mexico	Figure 14m	(Loyd *et al.* 2012, 2013)
[CAS]	3 M HCl	Rainstorm Member, Johnnie Fm	USA	Figure 14p	(Kaufman *et al.* 2007)
[Ba]	$HNO_3 + HClO_4 + HF + HCl$	Upper Doushantuo Fm at Jiulongwan and Songlin	China	N.A.	(Fang *et al.* 2019)
[Ba]	$HNO_3 + HClO_4 + HF$	Upper Doushantuo Fm at Huangniuyan	China	N.A.	(Tian and Luo 2017)
[Ba]	1 M HCl	Upper Doushantuo Fm at Jiulongwan and Siduping	China	Figure 15c, d, j–l	(Zhang *et al.* 2019; Cao *et al.* 2020)
[Ba]	0.5 M CH_3COOH[a]	Upper Doushantuo Fm at Jiulongwan	China	Figure 15c, d	(Cui *et al.* 2017)
[Ba]	1 M CH_3COOH	Upper Doushantuo Fm at Jiulongwan	China	Figure 15e	(Wei *et al.* 2021*b*)
[Ba]	0.4 M HNO_3 [b]	Upper Doushantuo Fm at Yangjiaping	China	Figure 15n	This study
[Ba]	1 M HCl[c]	Upper Clemente Fm	Mexico	Figure 15q, r, u	This study

[CAS] analyses in the compiled studies were analysed from carbonate-dominated samples. [Ba] analyses by concentrated strong acid do not differentiate any lithology, whereas [Ba] analyses by dilute acid with concentrations <1 M are mostly focused on carbonate-rich samples. In this study, only $[Ba]_{dilute\ acid}$ data were plotted and discussed.

[a] Ba concentration data for the Jiulongwan EN3/DOUNCE interval in Cui *et al.* (2017) were measured following the method in Zhou *et al.* (2012).

[b] Detailed method can be found in Liu *et al.* (2016) and Liu *et al.* (2021).

[c] Detailed method can be found in Zhang *et al.* (2019) and Cao *et al.* (2020).

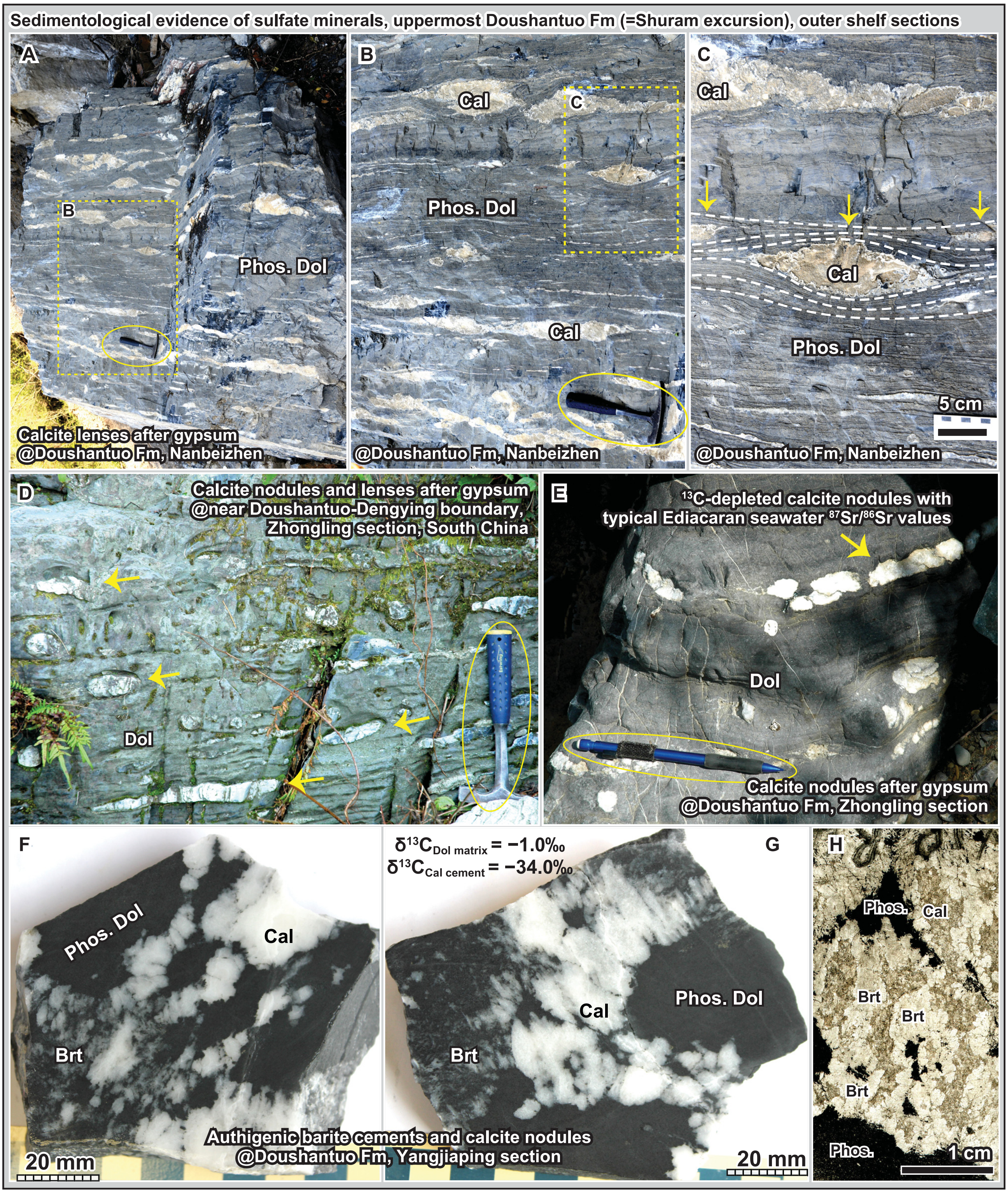

Fig. 4 Sedimentological evidence of sulfate minerals in the SE-equivalent strata at outer-shelf sections of the upper Doushantuo Formation. The stratigraphic positions of these sulfate minerals can be found in Figure 1k (Yangjiaping) and Figure 1l (Zhongling). (**a**) A fallen outcropt showing calcite lenses and nodules after gypsum, uppermost Doushantuo Formation, outer-shelf Nanbeizhen section. The Nanbeizhen section is located very close to the Zhongling section to the SW. (**b**, **c**) Closer views of the dashed boxes marked in (**a**) and (**b**), respectively. Note the warping laminations surrounding the nodules, indicating that the nodules formed before sediment compaction. The nodules and lenses (arrows) now consist of mostly calcite, with thin quartz rims. Enlarged photos of (**c**) can be found in the Supplementary material. (**d**) Calcitized gypsum lenses (arrows) within dolostones, Zhongling section, South China. Stratigraphic position: 30 m above the Doushantuo–Dengying boundary (i.e. the uppermost phosphorite interval). (**e**) Calcitized gypsum nodules (arrows) within dolostones of the upper Doushantuo Formation, Zhongling section, South China. Stratigraphic position: 210 m in Figure 1l. (**f**, **g**) Authigenic barite and calcite in the phosphorite interval of uppermost Doushantuo Formation at the outer shelf Yangjiaping section, South China. The $\delta^{13}C_{carb}$ values of micro-drilled powders of phosphatic dolostone matrix and calcite nodule in this sample are −1‰ and −34.0‰, respectively (Cui *et al.* 2016*a*). Sample number: YJP-R4 in Cui *et al.* (2016*a*); stratigraphic position: 105 m in Figure 1k. (**h**) A scanned thin-section image of the sample shown in (**g**). Note that the barite crystals grow centripetally towards the calcite nodule, suggesting that they formed before or simultaneously with the calcite. Petrographic images of barite in this thin section can be found in Figure 7. Images are from: **a**–**c**, **f** (this study); **d**, **e** (Cui *et al.* 2017); **g**, **h** (Cui *et al.* 2016*a*). See Appendix A for abbreviations.

difficult to differentiate from each other in thin sections' (Scholle and Ulmer-Scholle 2003). They all have low relief and birefringence (grey to white). All three sulfate minerals can form elongate, fibrous or bladed crystals, as well as aggregates of crystals (Scholle and Ulmer-Scholle 2003). Barite and gypsum can also form crystal rosettes (Scholle and Ulmer-Scholle 2003). Therefore, in this study, we do not differentiate between gypsum, celestite and barite pseudomorphs. It is notable that the barite and quartz pseudomorphs of sulfate minerals at the Zhongling and Yangjiaping sections are often associated with authigenic calcite that is highly depleted in ^{13}C (Fig. 1k, l) (Cui *et al.* 2016*a*; 2017). Petrographic observation shows that the barite crystals or quartz pseudomorphs often grow centripetally towards calcite nodules, suggesting that they formed before, or simultaneously with, the calcite (Cui *et al.* 2016*a*; 2017).

Doushantuo Formation at the intra-shelf basin

We report a new finding here: pyrite pseudomorphs after sulfate minerals in the EN3/DOUNCE interval at the intra-shelf Jiulongwan section (Fig. 9a–h). These pyrite pseudomorphs show a radial texture that resembles the morphology of modern gypsum analogues (Fig. 9i–l) (Tang *et al.* 2014), although original barite or celestine precipitation is also possible. Despite the uncertainty in the

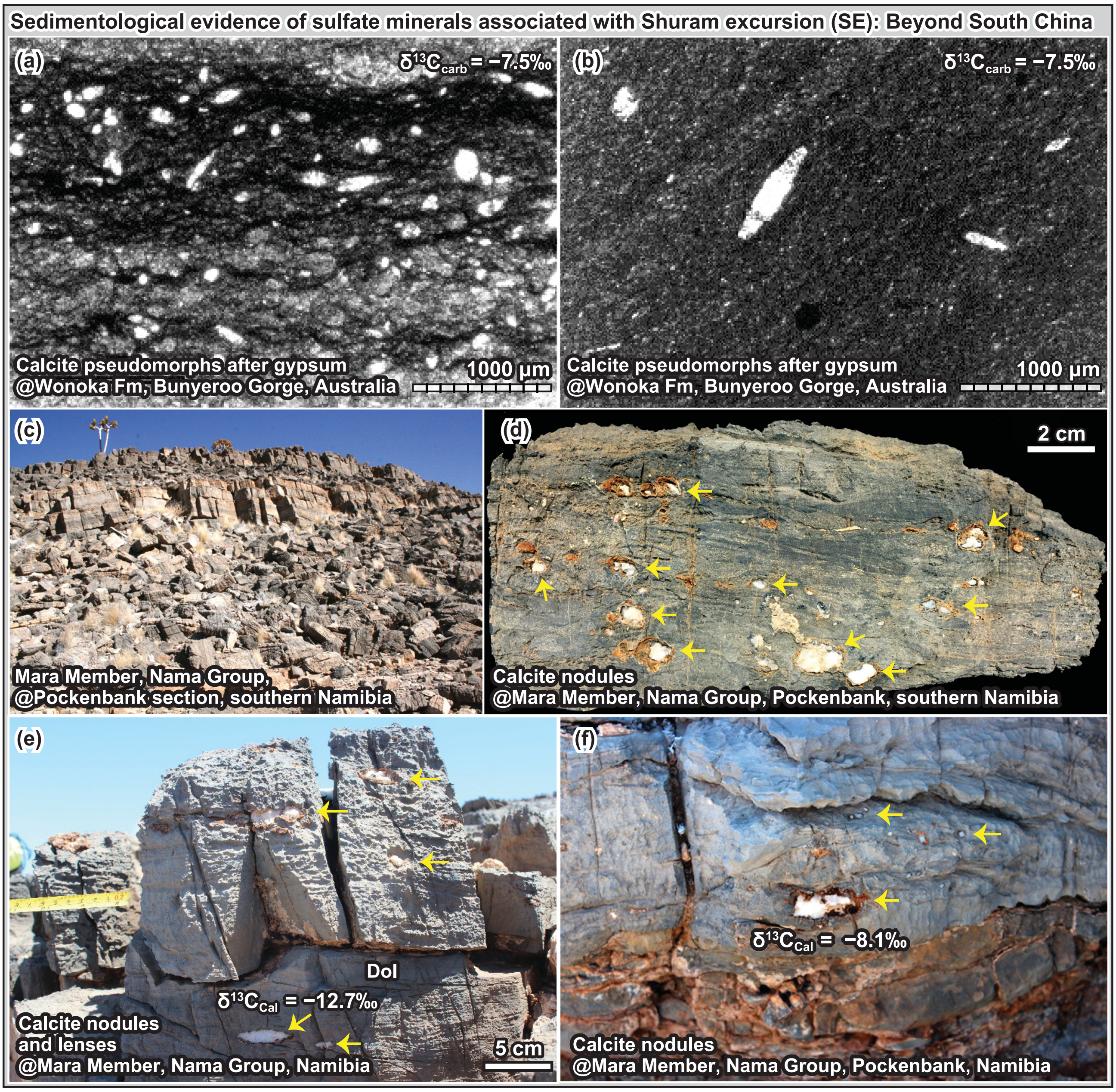

Fig. 5 Sedimentological evidence of sulfate minerals associated with the SE in Australia, Oman and Namibia. The stratigraphic positions of these sulfate minerals can be found in Figure 1a (Oman), Figure 1b (Wonoka) and Figure 1d (Nama). (**a**, **b**) Petrographic images of gypsum from Member 4 and Member 5 of the Wonoka Formation, Bunyeroo Gorge section, southern Australia (Calver 2000). (**c**) Outcrops of the Mara Member, Nama Group, Pockenbank section, southern Namibia. (**d–i**) Calcitized gypsum nodules or lenses within dolostones, Mara Member, Nama Group, Pockenbank section, southern Namibia. Arrows in (**d**–**f**) and (**i**) denote the calcitized gypsum nodules or lenses. Note that similar to the Doushantuo nodules in the outer-shelf environment (Fig. 4), these Mara calcite nodules or lenses (white) are all surrounded by thin quartz rims (brownish) and have highly negative $\delta^{13}C_{carb}$ values (Kaufman *et al.* 2015). (**g–i**) Calcitized gypsum nodules or lenses within dolostones, Mara Member, Nama Group, Pockenbank section, southern Namibia. (**j**) Centimetre-thick lenses of chertified evaporite, Khufai Fromation, WS section, Huqf area, Oman. Images are from: **a** and **b** (Calver 2000); **c–i** (this study); **j** (Le Guerroué 2006).

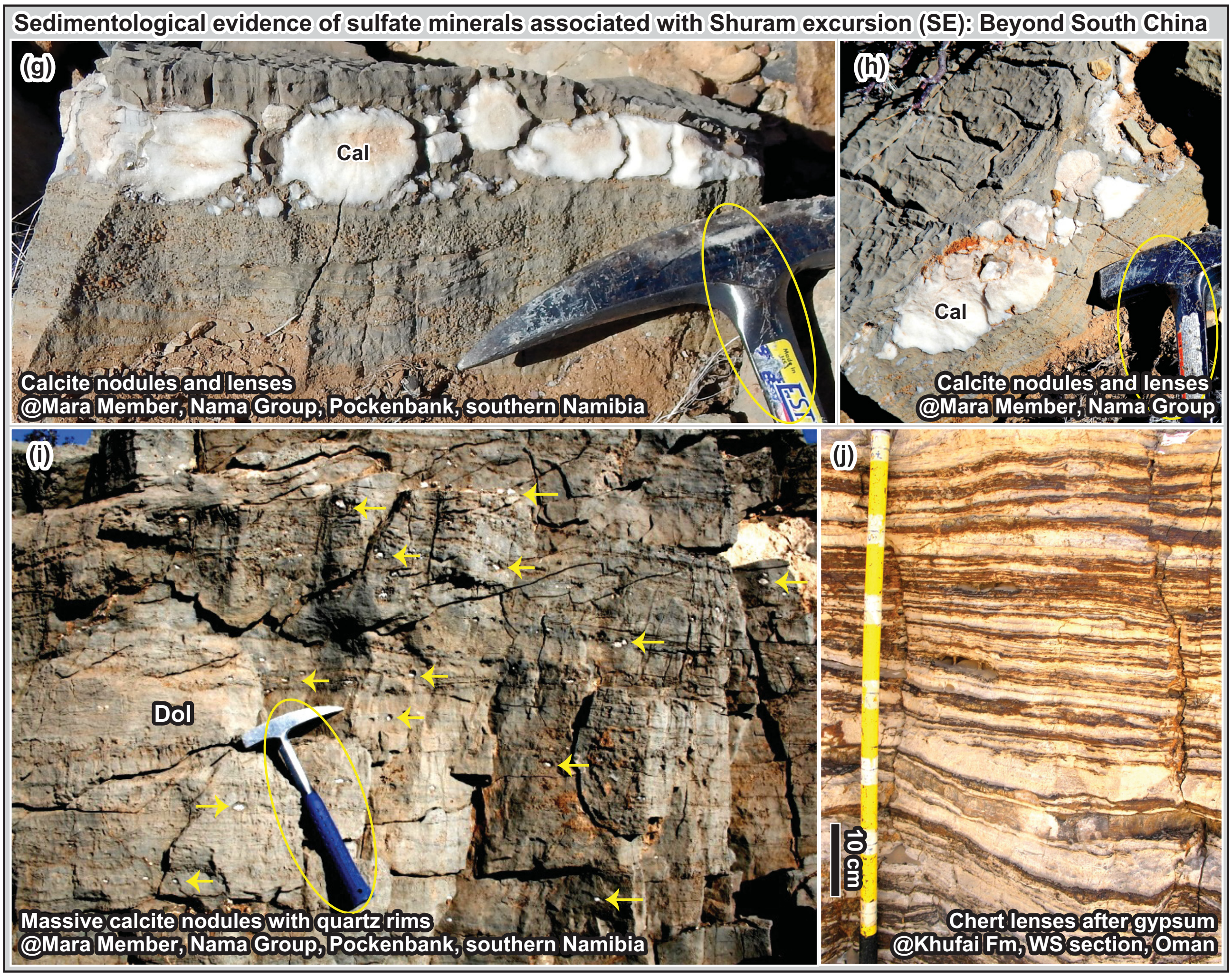

Fig. 5 (Continued.)

exact mineral, we regard this observation as indirect evidence for the presence of sulfate minerals during the SE.

Four samples from the Jiulongwan EN3/DOUNCE interval reveal petrographic evidence of diagenetic barite (Figs 8, 10–13). Together with our field observations (Fig. 3c, 3d), four distinct types of barite can be summarized.

(1) Relatively large diagenetic barite with grain size >100 µm (Figs. 10a, b, 11a, 12a). These barite crystals often show sharp crystal boundary (Fig. 10a, c, 11a) and are associated with zoned dolomite (Figs. 10a, c, 11a, 12a) and quartz (Figs 10a, 12a) crystals.

(2) Disseminated diagenetic barite inclusions within quartz (Fig. 12c, e, g). The size of these quartz-hosted barite inclusions can be as small as 1 or 2 µm, or up to 30 µm. The barite-bearing quartz precipitates normally show irregular shapes, are randomly distributed within the calcite matrix and are often far away from each other.

(3) Diagenetic barite veins (Fig. 13). It is worth noting that vertical barite veins in limestone sample HND27.75 (Fig. 13; height = 140.55 m at the Jiulongwan section, $\delta^{13}C_{carb} = -8.4‰$) cross-cut a dolomite-rich stylolite, suggesting the occurrence of barite precipitation after deposition. Although no clear evidence for hydrothermal alteration was found in the EN3/DOUNCE outcrop, it is possible that these vertical barite veins formed via local hydrothermal fluids that intruded into the partially dolomitized limestone strata.

(4) Large barite crystal fans have also been found at the outcrops of the uppermost Doushantuo Formation at the Jiulongwan section (Fig. 3d) (Cui *et al.* 2017). The barite crystal fans in the EN3c interval of the Jiulongwan section are often associated with early diagenetic carbonate nodules (Fig. 3c). The warping laminations surrounding the carbonate nodules indicate that these nodules are syndepositional, and formed before sediment compaction (Fig. 3c).

SE beyond China

Sulfate minerals or evaporative textures that are closely associated with the SE have also been found in Oman, Australia, India, Namibia and Russia.

(a) Oman. Although no sulfate mineral has been directly reported from the Shuram Formation, both the underlying Khufai Formation and the overlying Buah Formation show evidence of gypsum. Silicified anhydrite rosettes with anhydrite inclusions (Wright *et al.* 1990), silicified gypsum laminae (Fig. 5j) (Le Guerroué 2006), and fenestral mudstone with evaporite lathes (Osburn *et al.* 2014) were found in the Khufai Formation. Stratigraphically upward, the Buah Formation show fenestrae with gypsum, or partially filled with mega-quartz with anhydrite inclusions (Wright *et al.* 1990). In addition, massive anhydrite deposits

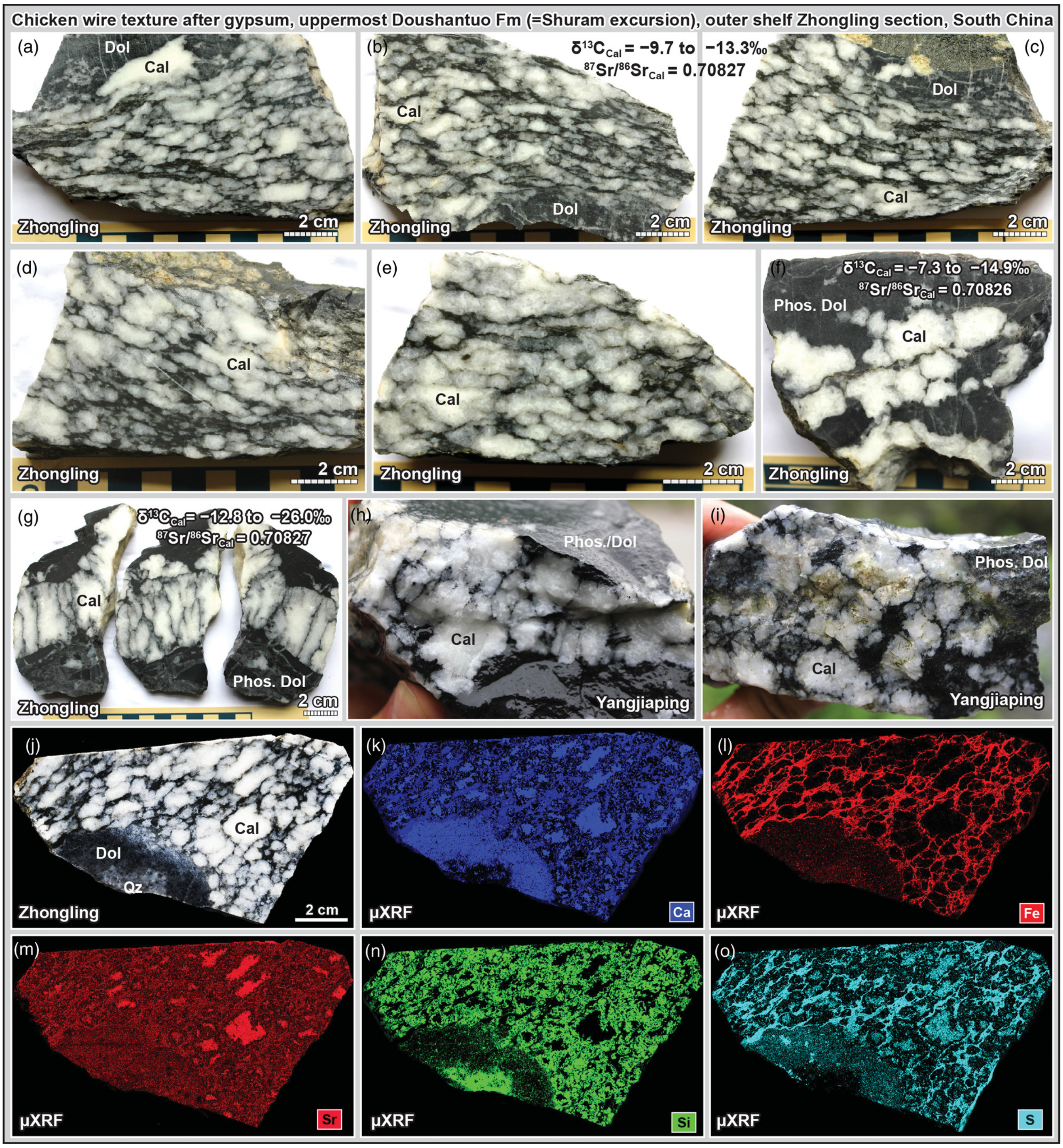

Fig. 6 Chicken-wire texture in the uppermost Doushantuo Formation (= SE) at the Zhongling and Yangjiaping sections (rimmed outer-shelf environment), South China. Note the contorted stringers at the nodule boundaries. (**a–g**) Samples collected from the Zhongling section. (**h–i**) Samples collected from the Yangjiaping section. (**j–o**) Elemental maps of slabs in image J generated by µXRF. Note that the white-coloured phases are now calcite or quartz, which probably formed via dissolution and replacement of original sulfate minerals by calcite and quartz. Detailed $\delta^{13}C_{carb}$ and $^{87}Sr/^{86}Sr$ values of the Yangjiaping and Zhongling samples measured via micro-drilling can be found in Cui *et al.* (2016*a*) and Cui *et al.* (2017), respectively. These calcites show extremely negative $\delta^{13}C_{carb}$ values down to −37‰ (Fig. 1k, l) and $^{87}Sr/^{86}Sr$ values within the range of typical Ediacaran seawater signals (i.e. 0.7083), suggesting an early authigenic origin via sulfate-driven AOM (Cui *et al.* 2017). The stratigraphic positions of these samples can be found in Figure 1k (Yangjiaping) and Figure 11 (Zhongling), respectively. Sample codes and stratigraphic positions: **a**–**d** (14ZL-4.5, 254.5 m, Zhongling), **e** (14ZL-3.5, 255.5 m, Zhongling), **f** (14ZL-6.5, 252.5 m, Zhongling), **g** (14ZL-7.5, 251.5 m and14ZL-6.6, 252.4 m, Zhongling), **h** and **i** (105 m, Yangjiaping), **j** (14ZL-4.5, 254.5 m, Zhongling). See Appendix A for abbreviations.

were preserved in the Ara Group in Oman (Fike and Grotzinger 2008, 2010; Smith 2012; Grotzinger and Al-Rawahi 2014).

(b) Australia. Unambiguous petrographic evidence of gypsum has been reported from the Unit 4 and Unit 5 of the Wonoka Formation at the Bunyeroo Gorge section, southern Australia (Fig. 5a, b), which shows typical SE with a nadir $\delta^{13}C_{carb}$ value of −11.2‰ (Fig. 1b) (Calver 2000).

(c) India. Gypsum casts have been reported from the Krol B interval at the Nigalidhar section, northern India (Fig. 1c) (Jiang *et al.* 2002), where a SE-like $\delta^{13}C_{carb}$ negative excursion with a nadir value of −8.8‰ was preserved in the Krol B and the overlying Krol C intervals (Kaufman *et al.* 2006).

(d) Namibia. Evaporite textures have also been reported from a limestone/grainstone interval of the Lower Mara Member,

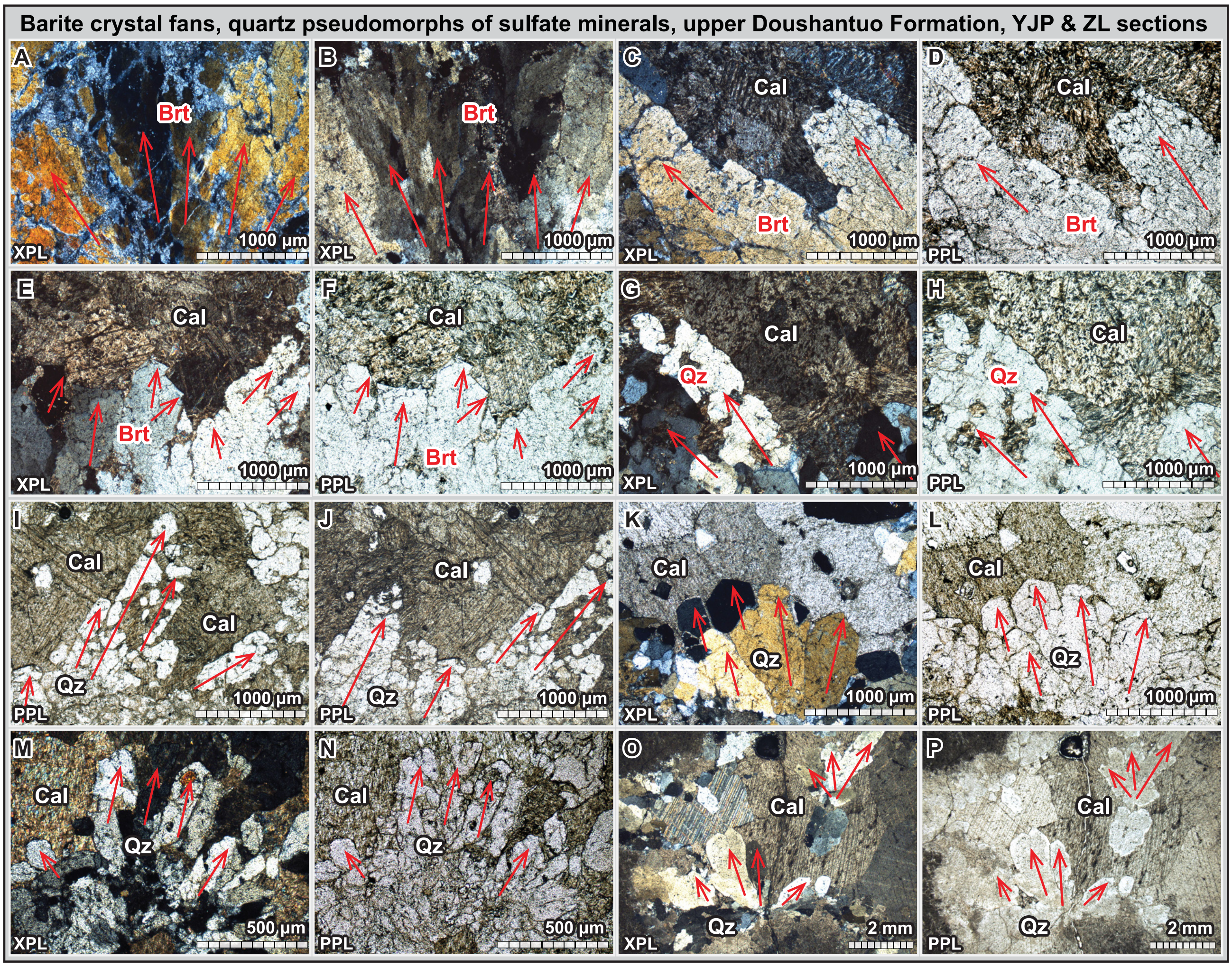

Fig. 7 Petrographic images of sulfate minerals from the upper Doushantuo Formaiton, Yangjiaping and Zhongling sections (rimmed outer-shelf environment), South China. Red arrows denote the crystal directions of sulfate minerals (or their pseudomorphs when they are silicified). (**a–f**) Barite crystals associated with ^{13}C-depleted calcite. Note the undulatory extinction of barite crystals. (**g–p**) Quartz pseudomorphs of sulfate minerals. Sample codes and stratigraphic positions: **a–f** (YJP-R4, 105 m, Yangjiaping); **g** and **h** (YJP-R5, 105 m, Yangjiaping); **i–n** (14ZL-4.5, 254.5 m, Zhongling); **o** and **p** (12ZL-21.6, 237.4 m, Zhongling). Images in **o** and **p** are from Cui *et al.* (2017); all the other images are new in this study. See Appendix A for abbreviations.

Nama Group at the Grens section, Witpus Sub-Basin, southern Namibia, where a $\delta^{13}C_{carb}$ negative excursion with a nadir value of −7.2‰ is preserved (Fig. 1d) (Wood *et al.* 2015).

In this study, we also report calcite lenses and nodules throughout the Mara Member. These Mara calcite nodules and lenses (white colour) are mostly surrounded by thin quartz rims (brownish colour) (Fig. 5), and show highly negative $\delta^{13}C_{carb}$ values (Kaufman *et al.* 2015). Both the sedimentological and geochemical features of these Mara nodules are similar to what we found in the upper Doushantuo Formation at the outer shelf sections (Fig. 4), indicating the same early diagenetic origin after evaporites.

(e) Russia. Celestine ($SrSO_4$) and strontianite ($SrCO_3$) have been reported in oolitic limestones of the Alyanchskaya Formation, Siberia, Russia (Melezhik *et al.* 2009). These minerals are coupled with remarkably high concentrations of Sr (>25 000 ppm) in the host limestones (Melezhik *et al.* 2009). The $\delta^{13}C_{carb}$ value of the celestine-bearing oolitic limestone sample is −8.0‰, which is consistent with signals during the SE (Fig. 1h) (Melezhik *et al.* 2009).

Geochemical profiles

In addition to field and petrographic investigations of sulfate minerals, we compiled published data for [CAS] and [Ba] in the SE-equivalents worldwide (Figs 14 and 15; Table 4). New [Ba] data of three SE sections are also provided in this study (Fig. 15n, q, r, u).

[CAS] enrichment and ^{34}S depletion

Published [CAS] profiles of five SE-equivalent sections are revisited in this study, including the Shuram Formation (Oman), the Doushantuo Formation at Jiulongwan and Siduping (China), the Clemente Formation (Mexico) and the Rainstorm Member (USA) (Fig. 14). Among all these sections, the SE intervals show higher [CAS] than pre- or post-SE intervals. The pyrite sulfur isotope ($\delta^{34}S_{pyrite}$) profiles of these sections, when available, show progressively lower values (<−5‰, VCDT, Fig. 14c, g, k). The CAS sulfur isotope ($\delta^{34}S_{CAS}$) profiles often show much larger sample-to-sample variability (Fig. 14g, k, n), which might result from diagenetic alteration (Peng *et al.* 2014) or potential contamination by pyrite oxidation (Marenco *et al.* 2008).

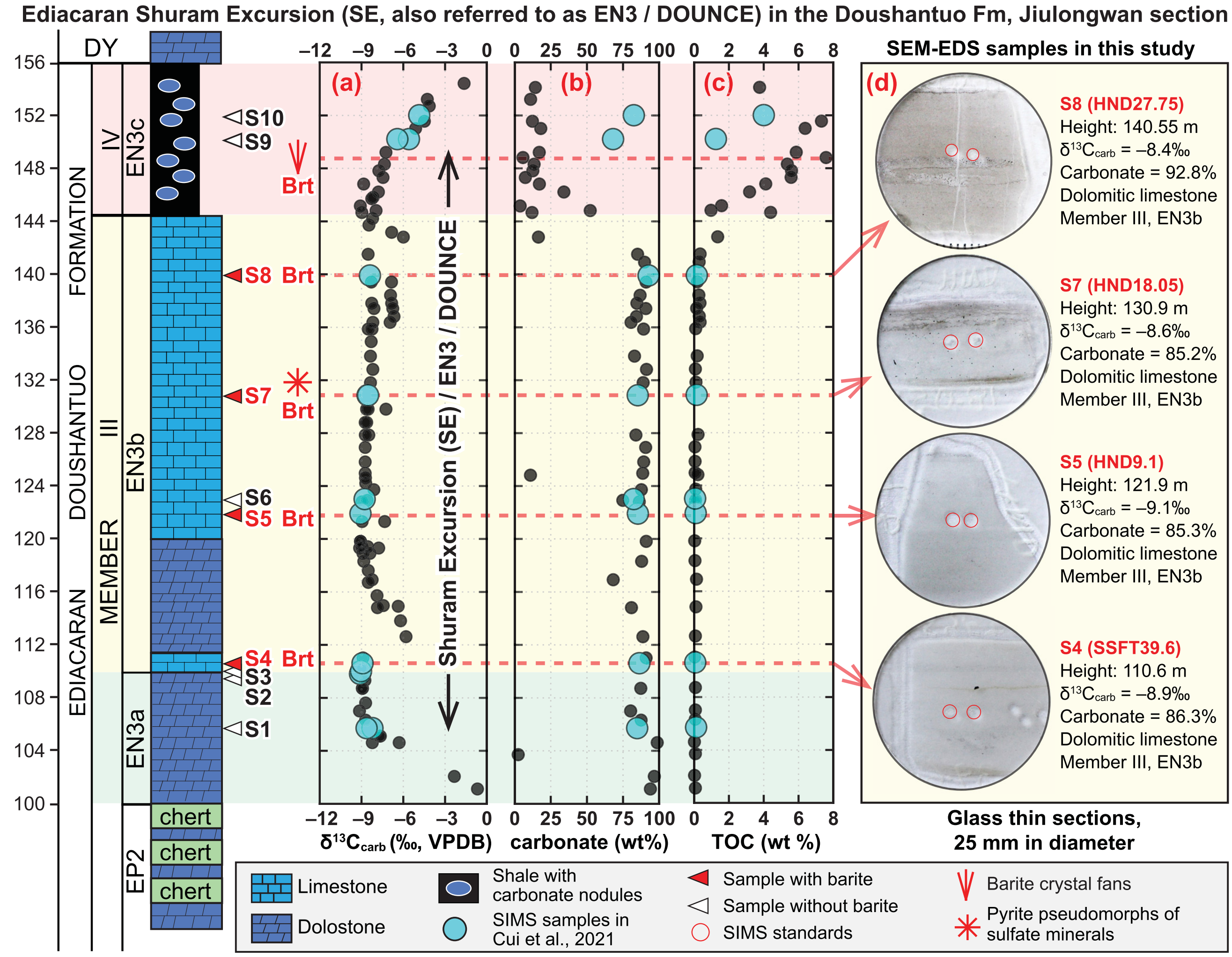

Fig. 8 Chemostratigraphy and sulfate mineral distribution of the Ediacaran SE in the Doushantuo Formation at the intra-shelf Jiulongwan section, Hubei Province, South China. The SE in the upper Doushantuo Formation of South China is also widely referred to as EN3 (Jiang *et al.* 2007; Zhou and Xiao 2007; McFadden *et al.* 2008) or DOUNCE (Lu *et al.* 2013; Zhu *et al.* 2013). Green, yellow and red background colours denote EN3a, EN3b and EN3c, respectively. (**a**) Chemostratigraphic $\delta^{13}C_{carb}$ profile based on $\delta^{13}C_{carb}$ values of micro-drilled powders. (**b**) Carboante content. (**c**) Total organic carbon (TOC) content. (**d**) Glass thin sections of the four samples with diagenetic barite. Each glass thin section is mounted with WiscSIMS calcite and dolomite standard materials for SIMS analysis. Detailed SIMS data of samples S1 to S10 can be found in Cui *et al.* (2021). SIMS samples S9 and S10 are carbonate concretion samples, hence they have high carbonate contents but low TOC compared with adjacent black shale samples. Data are from: Chemostratigraphic data (McFadden *et al.* 2008); images of glass thin sections (Cui *et al.* 2021); stratigraphic distribution of sulfate minerals (this study). See Appendix A for abbreviations.

Regardless, general decreasing trends are still evident in many $\delta^{34}S_{CAS}$ profiles of the SE sections (Fig. 14).

[Ba] enrichment

In this study, only $[Ba]_{dilute\ acid}$ are plotted and discussed. The $[Ba]_{dilute\ acid}$ profiles of five SE-equivalent sections include the upper Doushantuo Formation at the Jiulongwan, Siduping and Yangjiaping sections, and the upper Clemente Formation at the CR-1 and CR-2 sections (Fig. 15). All of these sections are dominated by carbonates. It is notable that these five sections all show significant enrichment in barium within the SE intervals (Fig. 15). Based on the $[Ba]_{dilute\ acid}$ profiles, a threshold value of $[Ba]_{dilute\ acid} = 50$ ppm is tentatively chosen to differentiate background (<50 ppm) and elevated (>50 ppm) [Ba], and this is denoted by the vertical dashed line in Figure 15. Some plots show extremely high $[Ba]_{dilute\ acid}$ values that dwarf the other $[Ba]_{dilute\ acid}$ data (Fig. 15j, q), therefore results are also shown in a log scale (Fig. 15c, k) or replotted across a smaller range (Fig. 15l, r) to better display the details of $[Ba]_{dilute\ acid}$ variation across the SE. Generally, the pre- and post-SE intervals show $[Ba]_{dilute\ acid} < 50$ ppm, whereas the SE intervals often show $[Ba]_{dilute\ acid}$ considerably higher than 50 ppm (Fig. 15).

Given that the adopted method of dilute-acid extraction should mostly dissolve the carbonate phase, the excess of Ba in the Ba-enriched intervals is probably derived from carbonate-hosted barium, instead of barite. It was recently proposed that the potential existence of witherite ($BaCO_3$) in the EN3/DOUNCE interval may account for the Ba enrichment (Wei *et al.* 2021*b*), although supporting XRD or petrographic evidence is still lacking. In this study, no clear evidence of witherite has been found at the Jiulongwan section after a thorough SEM-EDS investigation. It is likely that the leached barium is from the calcium carbonate lattice (i.e. carbonate-associated barium), and therefore the measured $[Ba]_{dilute\ acid}$ variation reflects dissolved [Ba] in seawater and/or porewater.

The above interpretation assumes that dilute acid with concentrations <1 M should only extract barium from carbonates. Caution should be taken when interpreting the [Ba] data analysed by various concentrations of acid (Table 4). Increasing concentrations of acid would progressively attack barite during sample dissolution.

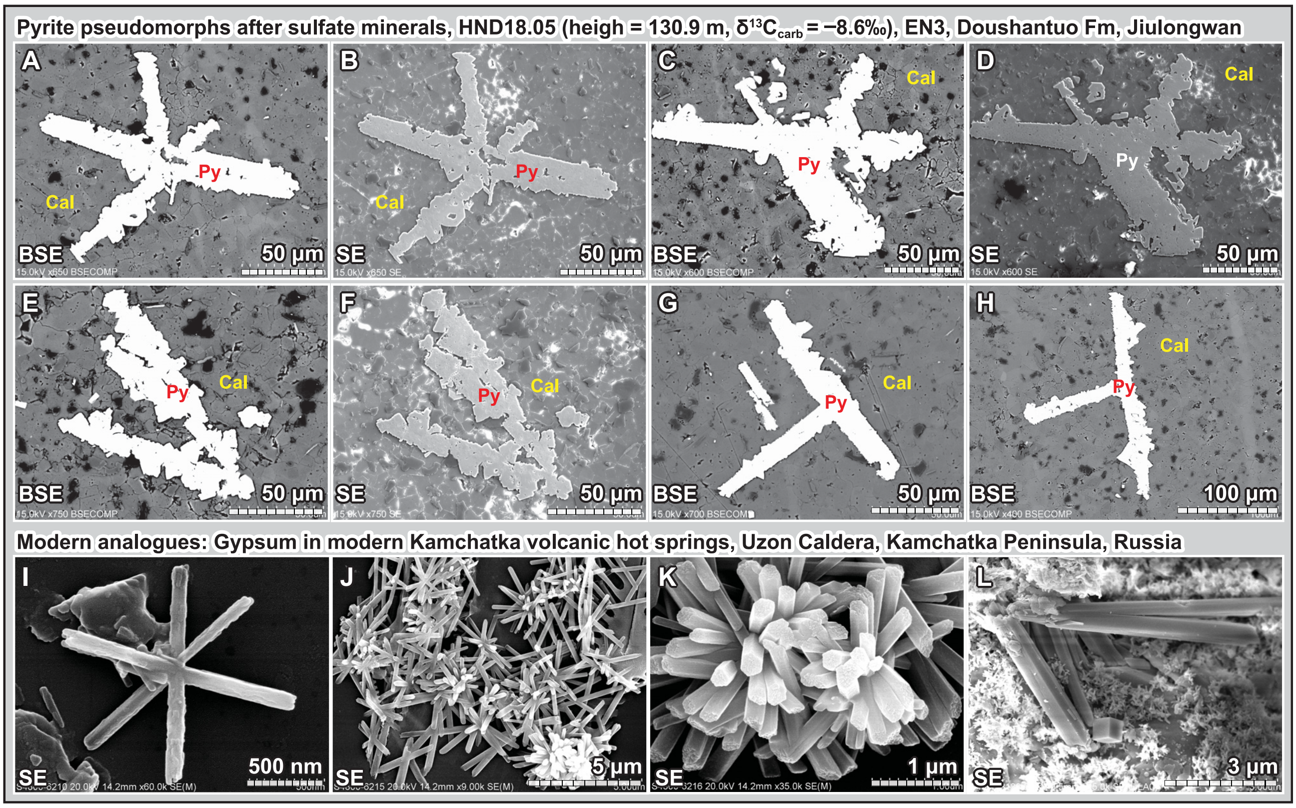

Fig. 9 Evidence of sulfate minerals from the upper Doushantuo Formation in South China and modern hot springs in Russia. (**a–h**) Pyrite pseudomorphs of sulfate minerals in limestone sample HND18.05 (stratigraphic height: 130.9 m, $\delta^{13}C_{carb} = -8.6‰$) of the EN3/DOUNCE interval, upper Doushantuo Formation, intra-shelf Jiulongwan section, South China. More detailed SEM-EDS results are available in the online supplementary material. (**i–l**) Modern gypsum analogues from the Kamchatka volcanic hot springs, Uzon Caldera, Kamchatka Peninsula, Russia (Tang *et al.* 2014). Note that the pyrite pseudomorphs show textures that are very similar to the modern gypsum crystals reported in Kamchatka Peninsula, Russia. Considering that gypsum, celestite and barite can show very similar textures in thin sections, we do not differentiate between these three minerals for pseudomorphs in this study. Data are from: $\delta^{13}C_{carb}$ value (McFadden *et al.* 2008); images **a**–**h** (this study); images **i–l** (Tang *et al.* 2014).

Therefore, the measured [Ba] and δ^{138}Ba values may reflect a mixture of both dissolved barium in seawater and barite within sediments. The finding of vertical barite veins that cut across dolomite-rich stylolites in sample HND27.75 (height 140.55 m, $\delta^{13}C_{carb} = -8.4‰$, Fig. 13) may further complicate the interpretation of the [Ba] and δ^{138}Ba data. We interpret these vertical barite veins as being caused by post-depositional Ba-rich fluids. The impact of these post-depositional Ba-rich fluids on the strata remains to be further evaluated.

Discussion

Mechanisms of C, S and Ba cycling

The coupled C, S and Ba anomalies presented in this study (Figs 15 and 16) indicate a dynamic interplay of the C, S and Ba cycles during the SE. Before we interpret the data, a brief review of biogeochemical C–S–Ba cycles in modern marine environments is necessary.

In modern marine environments where sulfate concentrations remain at around 28 mM, sulfate diffuses into shallow sediments and decreases in concentration at greater depths (Fig. 16a). In such environments, microbial sulfate reduction is the main mechanism by which organic matter is consumed, including methane (Bowles *et al.* 2014). Typically, the downward diffusing sulfate reacts with the upward diffusing methane, leading to the highest rate of anaerobic oxidation of methane (AOM) in the sulfate–methane transition zone (SMTZ) (Fig. 16a) (Jørgensen and Kasten 2006).

$$2CH_2O + SO_4^{2-} \rightarrow 2HCO_3^- + H^+ + HS^- \quad (1)$$

$$CH_4 + SO_4^{2-} \rightarrow HCO_3^- + HS^- + H_2O \quad (2)$$

Microbial sulfate reduction is a key factor in mediating carbonate mineral precipitation in sediments because it provides the majority of the alkalinity required for authigenic mineralization (Turchyn *et al.* 2021). During this process, alkalinity accumulates in pore fluids, leading to widespread mineralization of authigenic carbonates that often show highly negative $\delta^{13}C_{carb}$ signals (Meister *et al.* 2007). It has been estimated that authigenic carbonate precipitation accounts for at least 10% of global carbonate accumulation, representing a non-negligible component of the global carbon cycle in modern oceans (Sun and Turchyn 2014).

$$Ca^{2+} + 2HCO_3^- \rightarrow CaCO_3 + CO_2 + H_2O \quad (3)$$

Similar to the above interactions between sulfate and methane, downward diffusing sulfate and upward diffusing barium also react at a certain depth, forming the so-called authigenic barite front (Fig. 16b) (Torres *et al.* 1996; Dickens 2001; Dickens *et al.* 2003; Jørgensen and Kasten 2006; Riedinger *et al.* 2006).

$$Ba^{2+} + SO_4^{2-} \rightarrow BaSO_4 \quad (4)$$

Integrated profiles of dissolved [Ba^{2+}], dissolved [SO_4^{2-}] and barite contents in marine sediments show that authigenic barite is most abundant at the base of the sulfate reduction zone, and starts to dissolve at a greater depth where sulfate is close to complete exhaustion (Gingele *et al.* 1999; Jørgensen and Kasten 2006). The complete depletion of porewater sulfate leads to an undersaturation condition with respect to barite and to its subsequent dissolution

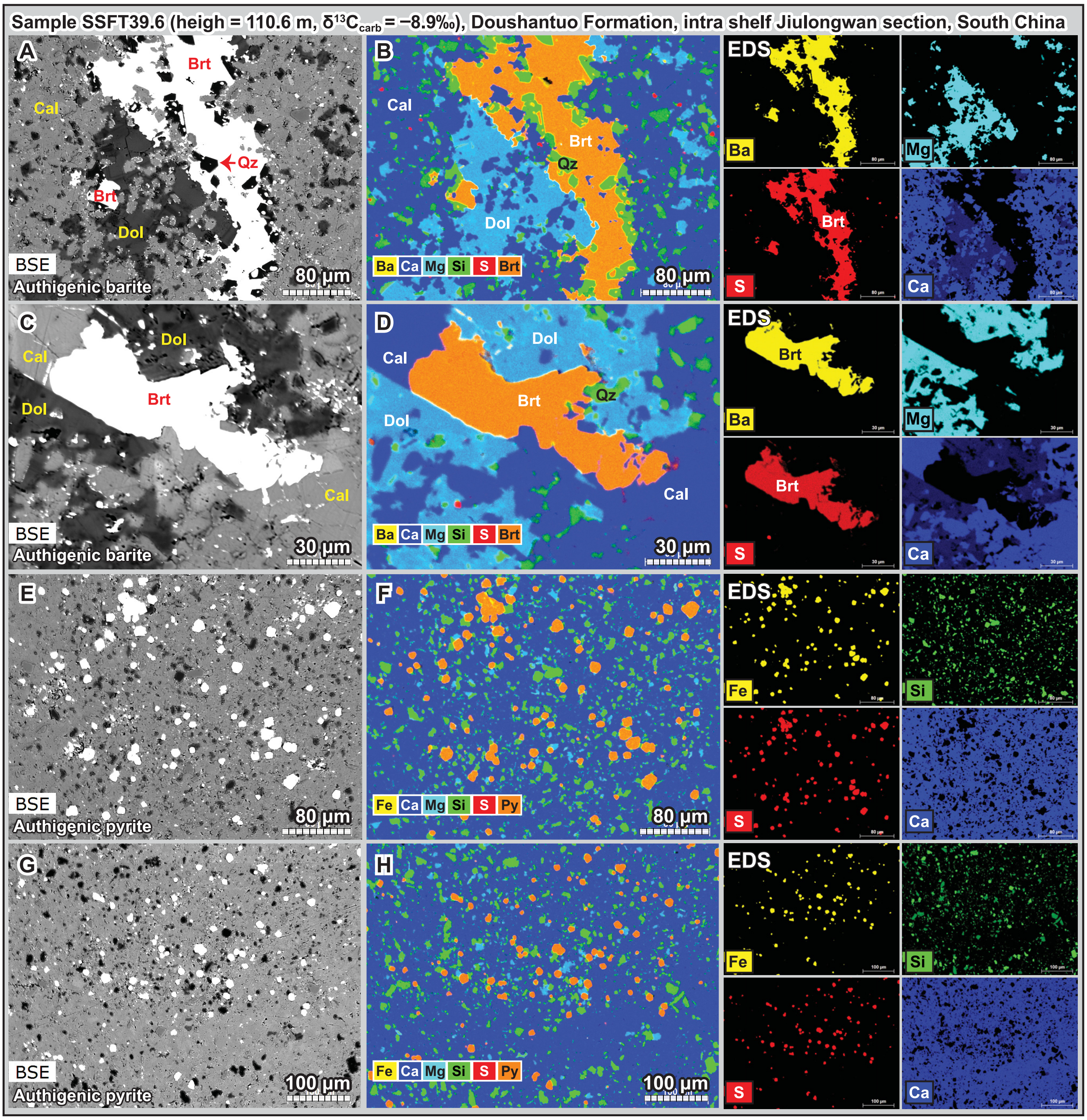

Fig. 10 Petrographic evidence of authigenic barite and pyrite in limestone sample SSFT39.6 (height above the Nantuo diamictite: 110.6 m) from the EN3/DOUNCE interval (= SE) at the Jiulongwan section, South China. The corresponding $\delta^{13}C_{carb}$ value of this limestone sample is −8.9‰ based on measurements of the micro-drilled powder. Images (**a**), (**c**), (**e**) and (**g**) are BSE images, and all others are EDS elemental maps. Note that barite and pyrite in EDS images appear as an orange colour, which results from the superimposition of yellow (Ba or Fe) and red (S) colours. Data are from: $\delta^{13}C_{carb}$ value (McFadden *et al.* 2008); all of the SEM-EDS results are newly presented in this study. See Appendix A for abbreviations. More detailed SEM-EDS results are available in the online supplementary material.

(Von Breymann *et al.* 1992; Torres *et al.* 1996; Gingele *et al.* 1999).

$$BaSO_4 \rightarrow Ba^{2+} + SO_4{}^{2-} \quad (5)$$

It has been argued that barite cannot form in euxinic conditions (Wei *et al.* 2021*b*). In fact, euxinic conditions alone do not prohibit barite precipitation. It is necessary to note that undersaturation and dissolution of barite in porewater or seawater occur only when sulfate is quantitively exhausted (Gingele *et al.* 1999; Jørgensen and Kasten 2006). Based on the petrographic results for barite within the Jiulongwan EN3/DOUNCE interval (Figs 10–13), it is likely that dissolution and remobilization of barite occurred after deposition.

Redox zonation in deep time

With the above framework in mind, it is necessary to note that, in contrast to the modern environment, the ocean in most of the Precambrian was dominated by anoxic redox conditions (Lyons *et al.* 2014). Therefore, biogeochemical C, S and Ba cycles may have functioned in a different fashion. In light of this, a non-actualistic view is crucial to gain insight into the functioning of biogeochemical cycles in deep time (Schrag *et al.* 2013; Meister 2015).

Compared with modern analogues, it is likely that the depths of the sulfate reduction zone, SMTZ and authigenic barite front could

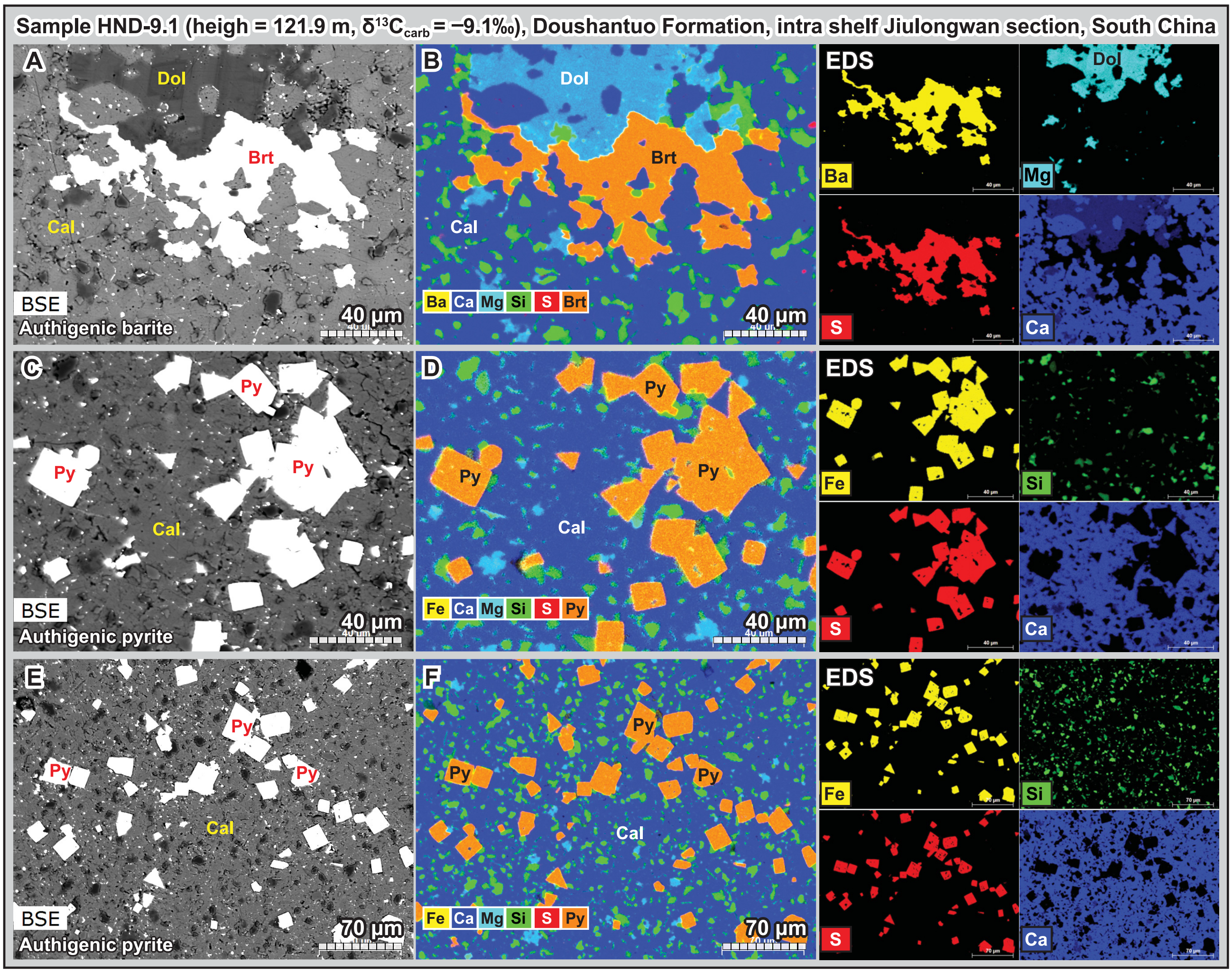

Fig. 11 Petrographic evidence of authigenic barite and pyrite in limestone sample HND-9.1 (height above the Nantuo diamictite: 121.9 m) from the EN3/DOUNCE interval (= SE) at the Jiulongwan section, South China. The corresponding $\delta^{13}C_{carb}$ value of this limestone sample is −9.1‰ based on measurements of the micro-drilled powder. Images (**a**), (**c**) and (**e**) are BSE images, and all others are EDS elemental maps. Note that barite or pyrite in EDS images appear as an orange colour, which results from the superimposition of yellow (Ba or Fe) and red (S) colours. Data are from: $\delta^{13}C_{carb}$ value (McFadden *et al.* 2008); all the SEM-EDS results are newly presented in this study. See Appendix A for abbreviations. More detailed SEM-EDS results are available in the online supplementary material.

have been much shallower in Precambrian sediments than in modern marine sediments (Fig. 16c, d). This inference is largely derived from evidence and arguments for much lower concentrations of sulfate (Habicht *et al.* 2002; Kah *et al.* 2004; Canfield and Farquhar 2009; Algeo *et al.* 2015) and much higher concentrations of barium (Crockford *et al.* 2019*a*; Wei *et al.* 2021*a*) in a dominantly anoxic Precambrian ocean. The potential for a shallower sulfate reduction zone in the Precambrian ocean opens the possibility of the continuous syndeposition of authigenic carbonates, which would no longer occur after the rise of sulfate to a modern level and the emergence of bioturbation – except in local cold seep environments (Cui *et al.* 2017). Quantitative modelling for the Jiulongwan EN3 interval estimates that seawater sulfate concentrations in intra-shelf environments increased from 3.5 mM to *c.* 8.7 mM, and possibly up to 14.5 mM (Shi *et al.* 2018). Therefore, the SE may have witnessed a progressive deepening of the SMTZ (Cui *et al.* 2017).

Following the scheme of a largely low-sulfate, high-barium and increasingly oxygenated Precambrian ocean, it is possible that past oceans could have witnessed episodes of transient increases in barite mineralization driven by a progressive growth of the seawater sulfate reservoir (Fig. 16e). Indeed, a recently published compilation of time-series [Ba] data based on mudstone records throughout Earth history reveals a notable peak in [Ba] during the Ediacaran–Cambrian transition (Fig. 17) (Wei *et al.* 2021*a*). This [Ba] peak is remarkably consistent with the view of an increasingly oxygenated Earth surface environment based on Ce/Ce* and $\delta^{34}S$ proxies (Fig. 17).

Large sulfate and barium reservoirs during the SE

On the basis of the finding of sulfate minerals and higher [CAS] and $[Ba]_{\text{dilute acid}}$ during the SE (Figs 1, 3–15; Tables 1–4), we propose that seawater sulfate and barium concentrations during the SE may have been significantly elevated, at least for transient episodes. Higher seawater sulfate concentrations during the SE not only promoted the deposition of gypsum and anhydrite, but also appear to have facilitated barite mineralization and burial. Our interpretation is consistent with published geochemical profiles that show lower $\delta^{34}S$, higher $^{87}Sr/^{86}Sr$ and more positive $\delta^{238}U$ signals during the SE (Figs 14 and 15). The progressively lower $\delta^{34}S$ and higher [CAS] values during the SE suggest a rise in sulfate concentrations with a considerable input of a ^{34}S-depleted source (probably from pyrite oxidation). Higher $^{87}Sr/^{86}Sr$ ratios reflect enhanced silicate weathering and a larger riverine flux (Burns *et al.* 1994; Melezhik *et al.* 2009; Sawaki *et al.* 2010; Li *et al.* 2017), which could bring

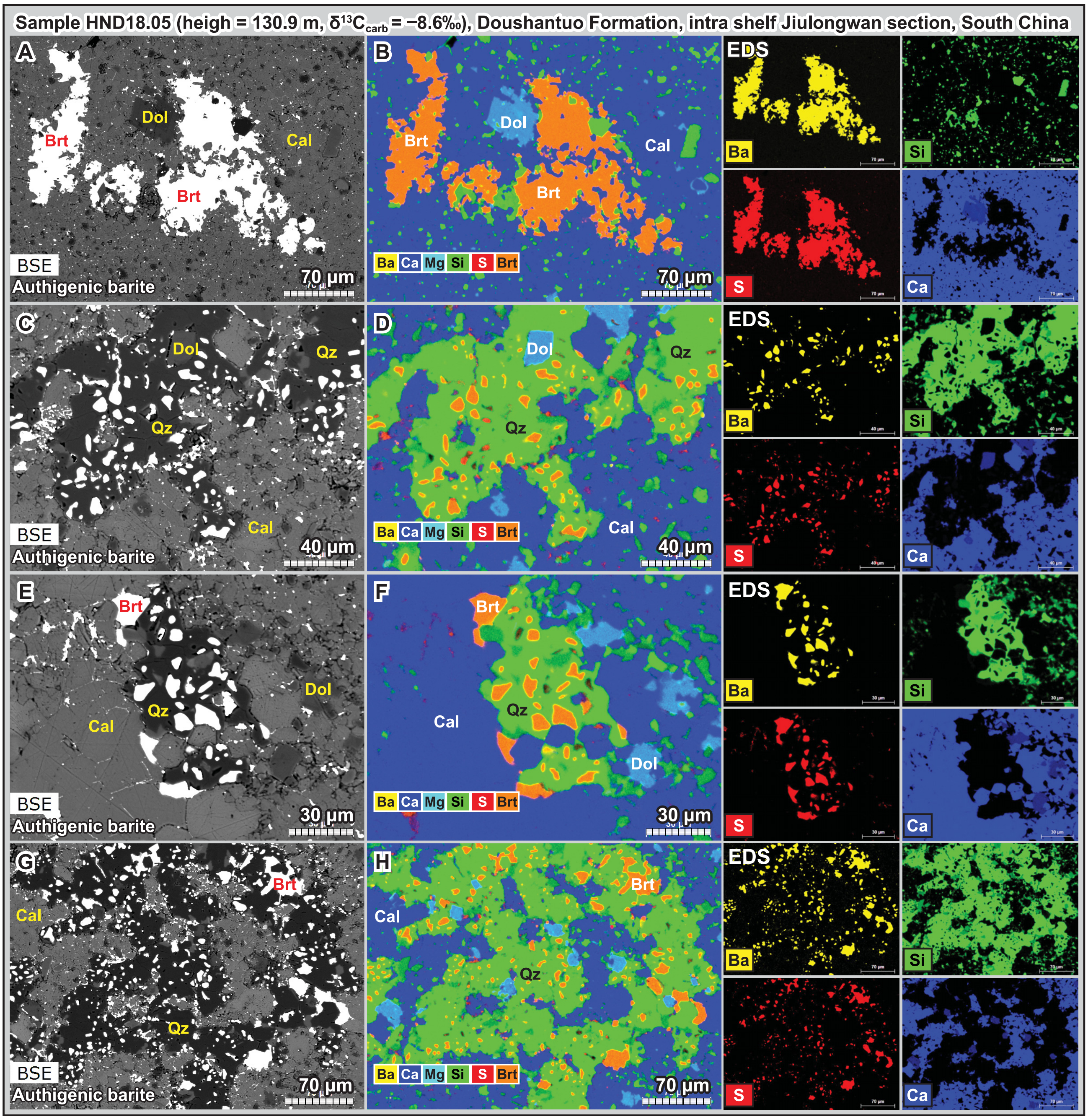

Fig. 12 Petrographic evidence of authigenic barite in limestone sample HND18.05 (height above the Nantuo diamictite: 130.9 m) from the EN3/DOUNCE interval (= SE) at the Jiulongwan section, South China. The corresponding $\delta^{13}C_{carb}$ value of this limestone sample is −8.6‰ based on measurements of the micro-drilled powder. Images (**a**), (**c**), (**e**) and (**g**) are BSE images, and all others are EDS elemental maps. Authigenic barite crystals in (**c**), (**e**) and (**g**) are mostly hosted within authigenic quartz, suggesting a diagenetic origin. Note that barite in EDS images appears as an orange colour, which results from the superimposition of yellow (Ba) and red (S) colours. Dara are from: $\delta^{13}C_{carb}$ value (McFadden *et al.* 2008); all the SEM-EDS results are newly presented in this study. See Appendix A for abbreviations. More detailed SEM-EDS results are available in the online supplementary material.

more sulfate and dissolved barium to the ocean. The rapid shift of $\delta^{238}U$ towards higher values strongly argues for an oceanic oxygenation event on a global scale (Zhang *et al.* 2019; Li *et al.* 2020*b*). Taken together, the overall more oxidizing conditions may have promoted widespread oxidation of terrestrial pyrite, leading to the rapid growth of the marine sulfate reservoir at that time.

The finding of a close coupling between sulfate minerals and the SE may shed light on the origin of this profound $\delta^{13}C_{carb}$ negative excursion. Multiple ^{13}C-depleted reduced carbon reservoirs have been invoked to explain the SE, including (listed in chronological order of publication) dissolved organic carbon in a stratified ocean (Fike *et al.* 2006; McFadden *et al.* 2008), terrestrial fossil organic carbon (Kaufman *et al.* 2007), methane hydrate (Bjerrum and Canfield 2011), biogenic methane or other organic matter within shallow marine sediments (Schrag *et al.* 2013; Cui *et al.* 2017) and expelled petroleum from deep subsurface source rocks (Lee *et al.* 2015). All of these hypotheses require an essential trigger – a large flux of oxidant that can oxidize these purported reduced carbon sources to drive the $\delta^{13}C$ of dissolved inorganic carbon towards lower values, either in globally distributed basins or in the open ocean.

Besides atmospheric oxygen, potential oxidants for the SE also include SO_4^{2-}, iron oxide (Fe_2O_3), and manganese oxide (MnO_2). However, the availability and significance of the oxidant budget for

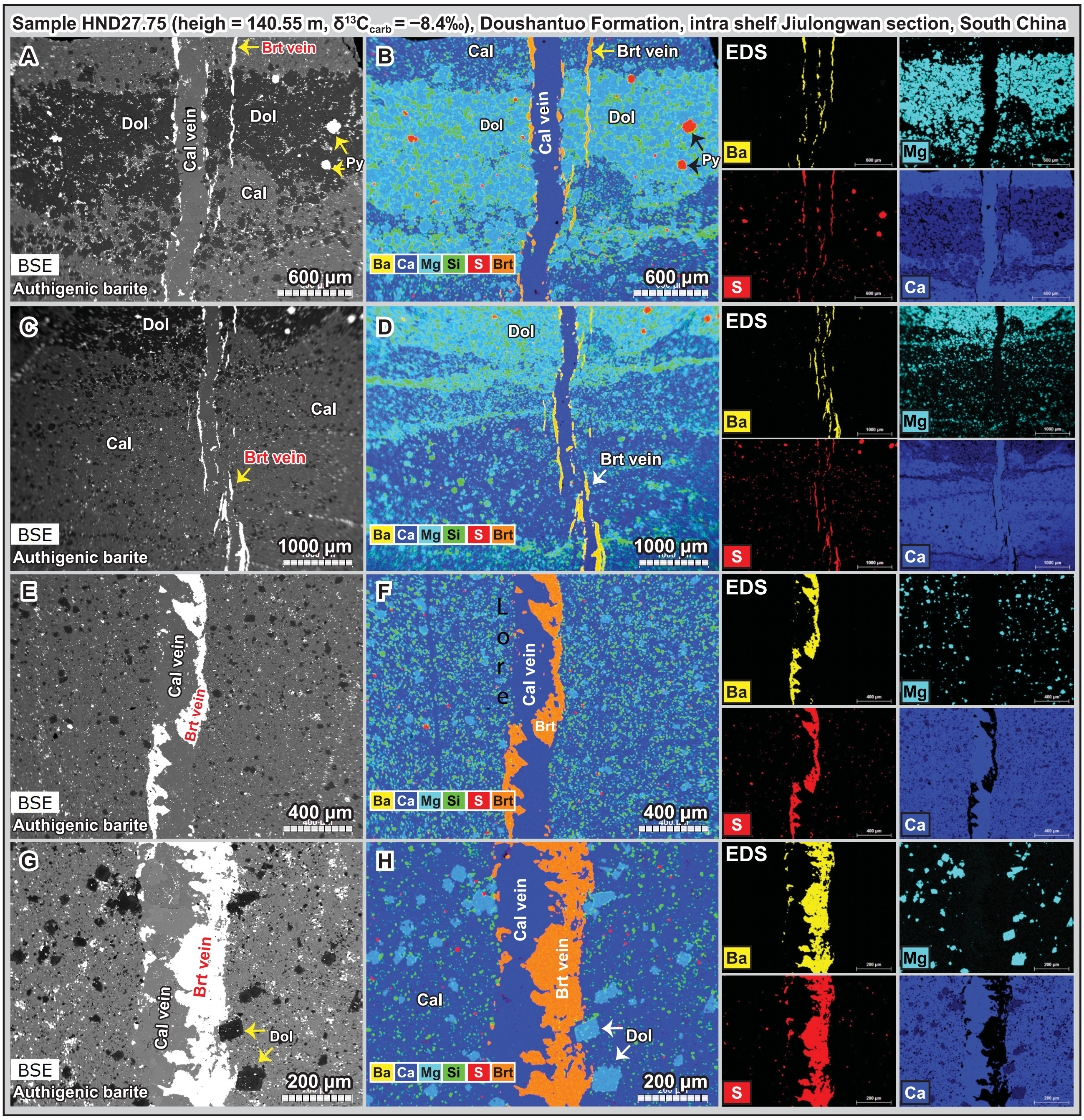

Fig. 13 Petrographic evidence of authigenic barite in sample HND27.75 (height above the Nantuo diamictite: 140.55 m) from the EN3/DOUNCE interval (= SE) at the Jiulongwan section, South China. The corresponding $\delta^{13}C_{carb}$ value of this limestone sample is not available. The value −8.4‰ presented in the figure was measured from a nearby sample HND 27.1, which is stratigraphically 0.6 m below sample HND27.75. Images (**a**), (**c**), (**e**) and (**g**) are BSE images, and all others are EDS elemental maps. Barite in EDS images appears as an orange colour, which results from the superimposition of yellow (Ba) and red (**S**) colours. Note that barite in this sample is shown as vertical veins that cut across a dolomite-rich stylolite. Considering that no clear evidence for hydrothermal alteration is found in the EN3/DOUNCE interval, it is likely that these barite veins formed via barite dissolution and reprecipitation during burial diagenesis. Data are from: $\delta^{13}C_{carb}$ value (McFadden *et al.* 2008); all the SEM-EDS results are newly presented in this study. See Appendix A for abbreviations. More detailed SEM-EDS results are available in the online supplementary material.

the SE remains a matter of debate (Bristow and Kennedy 2008; Shi *et al.* 2017). It has been proposed that a larger flux of sulfate derived either from pyrite oxidation (Kaufman *et al.* 2007; Li *et al.* 2010) or from evaporite recycling (Shields *et al.* 2019) may have contributed to the SE. Here, we provide petrographic and geochemical evidence for elevated sulfate concentrations associated with strata that preserve the SE, which supports the hypothesis that a larger sulfate influx may have played an essential role in oxidizing a large reduced carbon reservoir during the SE (Kaufman *et al.* 2007; Shields *et al.* 2019). Enhanced oxidative weathering, evaporite recycling, microbial sulfate reduction and pyrite burial may have formed a biogeochemical loop with positive feedback, contributing to the long-lasting oxygenation event recorded by the SE. The existence of sulfate minerals (this study) and Fe oxides (Bergmann 2013; Song *et al.* 2017) in the SE-equivalent strata suggests that oxidants were not depleted during the SE, which challenges the modelling results of Bristow and Kennedy (2008).

The finding of sulfate minerals associated with the SE also calls for a reappraisal of sulfate concentrations in the Ediacaran basins. A sulfate gradient model has been proposed largely on the

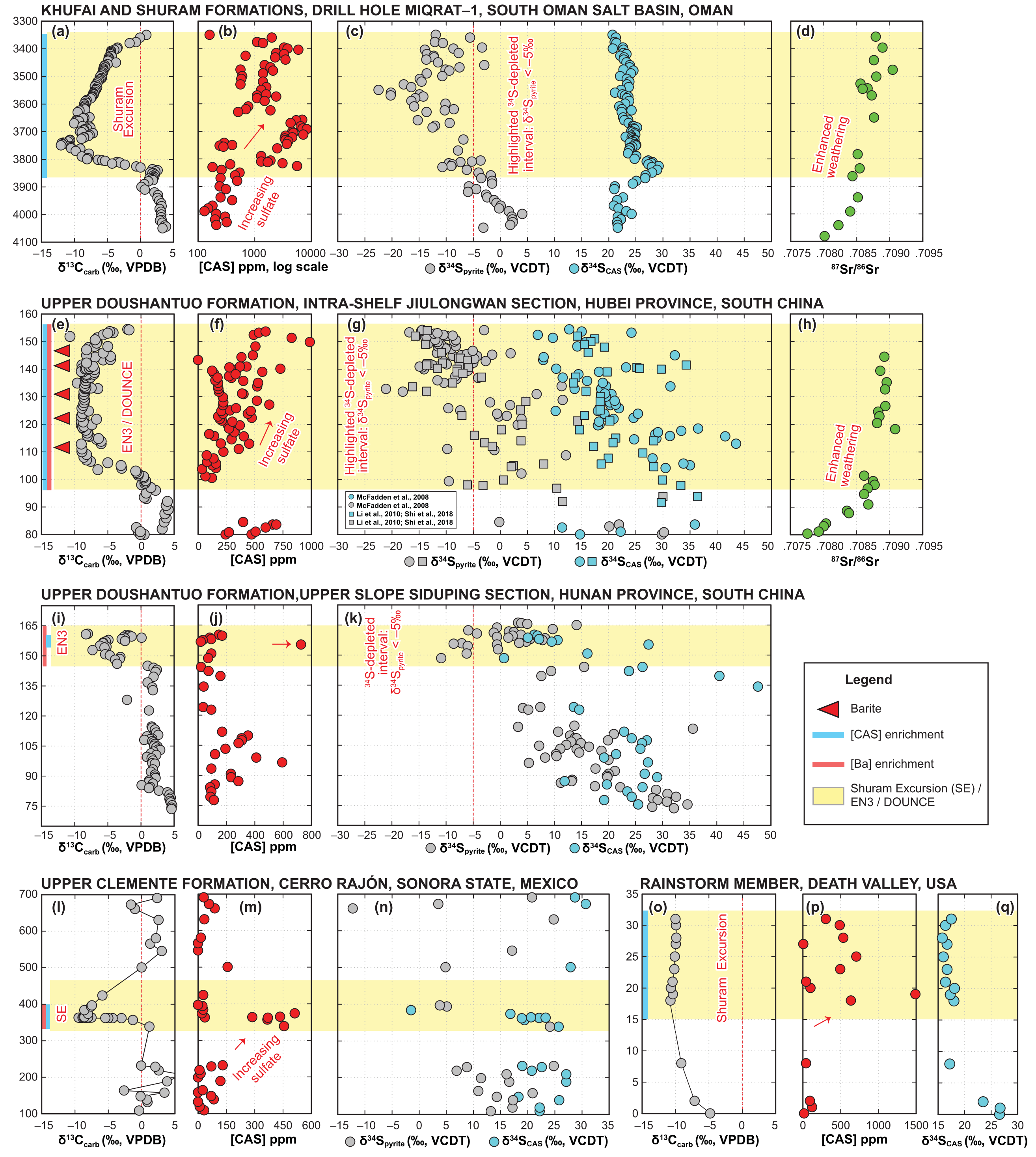

Fig. 14. Chemostratigraphy of the sections that record the Ediacaran SE. The SE in the uppermost Doushantuo Formation of South China is also widely referred to as EN3 (Jiang *et al.* 2007; Zhou and Xiao 2007; McFadden *et al.* 2008) or DOUNCE (Lu *et al.* 2013; Zhu *et al.* 2013). Intervals shaded in yellow show coupled negative δ^{13}C values and lower $\delta^{34}S_{pyrite}$ values (<−5‰). (**a–d**) Khufai and Shuram formations in South Oman salt basin, Oman. (**e–h**) Upper Doushantuo Formation at the intra-shelf Jiulongwan section, South China. Red triangles show the horizons with authigenic barite described in this study. (**i–k**) Upper Doushantuo Formation at the upper-slope Siduping section, South China. (**l–n**) Upper Clemente Formation at the CR-1 section, Cerro Rajón, Sonora State, Mexico. (**o–q**) Rainstorm Member at Winters Pass Hills, Death Valley, western USA. Note the elevated CAS concentrations during the SE in (**b**), (**f**) and (**m**). The close coupling of the higher sulfate concentrations, lower $\delta^{34}S_{pyrite}$ values (<−5‰) and higher $^{87}Sr/^{86}Sr$ ratios during the SE suggest a causal link between biogeochemical carbon and sulfur cycling in a period with enhanced chemical weathering. Data are from: Oman (Burns *et al.* 1994; Fike *et al.* 2006); Jiulongwan (McFadden *et al.* 2008; Li *et al.* 2010; Sawaki *et al.* 2010; Shi *et al.* 2018), Siduping (Li *et al.* 2017; Shi *et al.* 2018), Mexico (Loyd *et al.* 2012), Death Valley (Kaufman *et al.* 2007). See Appendix A for abbreviations.

basis of the Doushantuo Formation at the Jiulongwan and Zhongling sections (Li *et al.* 2010). In this model, sulfate concentrations show a gradual decrease from intra-shelf environments to outer-shelf environments (Li *et al.* 2010; Shi *et al.* 2018). This model has been applied to explain the heterogeneous $\delta^{13}C_{carb}$ excursions in the uppermost Doushantuo Formation (Li *et al.* 2017). However, if our interpretation of the chicken-wire evaporites at Zhongling and Yangjiaping (Fig. 6) is correct, it

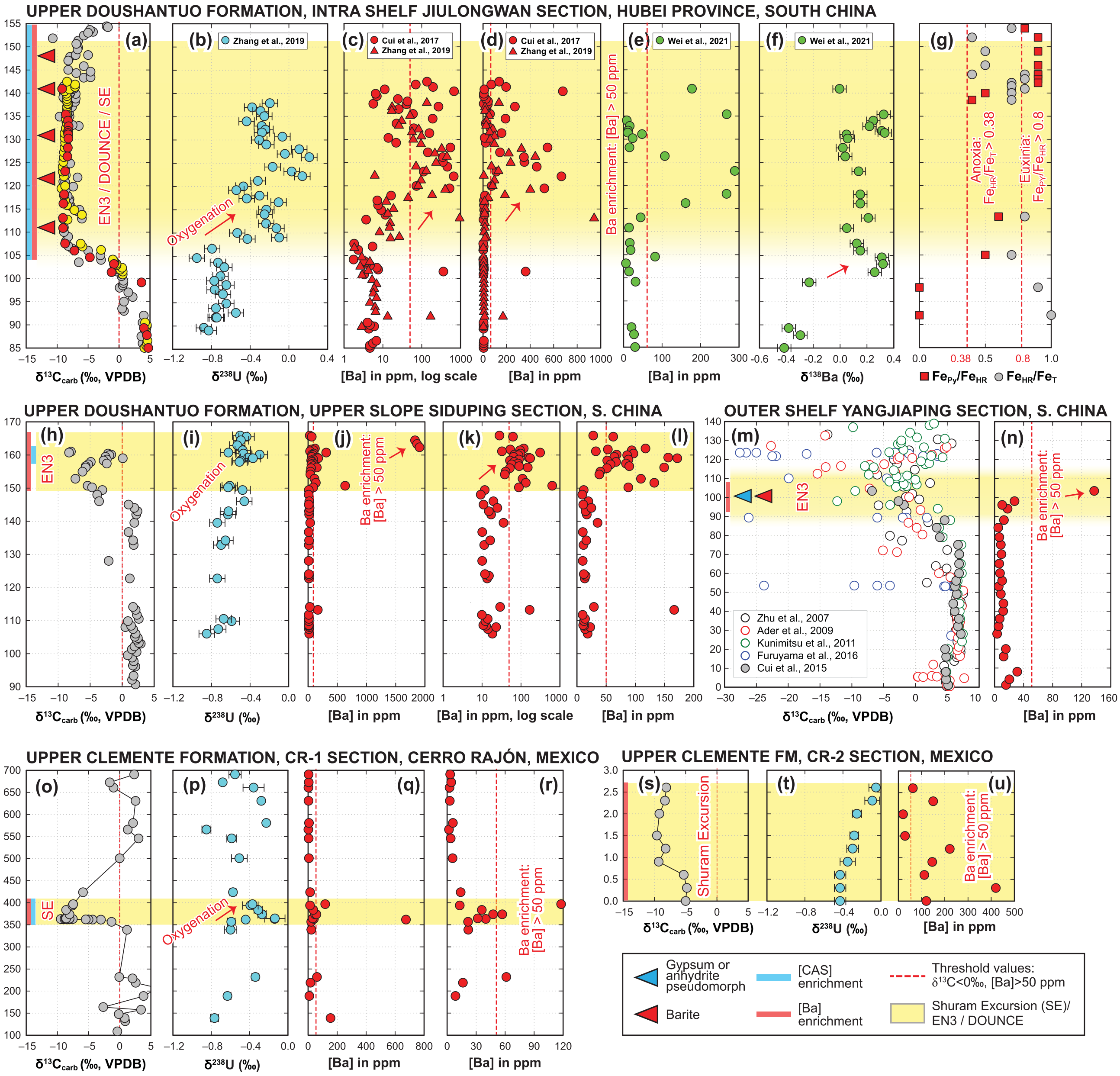

Fig. 15 Chemostratigraphy of the SE in South China and Mexico. The SE in the uppermost Doushantuo Formation of South China is also widely referred to as EN3 (Jiang *et al.* 2007; Zhou and Xiao 2007; McFadden *et al.* 2008) or DOUNCE (Lu *et al.* 2013; Zhu *et al.* 2013). All of the [Ba] data were generated via dilute acid dissolution (shown as $[\mathrm{Ba}]_{\mathrm{dilute\ acid}}$). Intervals shaded in yellow denote Ba enrichment with $[\mathrm{Ba}]_{\mathrm{dilute\ acid}}$ higher than 50 ppm. Note that all the SE profiles are closely coupled with an increase in δ^{238}U and Ba concentrations, which are interpreted as a direct response to enhanced sulfate concentration in a more oxygenated ocean. Some data are plotted on log scales to show the full range of variation (e.g. **c**, **k**), and also in a smaller scale (e.g. **l**, **r**) to visualize the variation in $[\mathrm{Ba}]_{\mathrm{dilute\ acid}}$ across the SE. (**a–g**) Upper Doushantuo Formation at the intra-shelf Jiulongwan section, South China. (**h–l**) Upper Doushantuo Formation at the upper-slope Siduping section, South China. (**m–n**) Upper Doushantuo Formation at the outer-shelf Yangjiaping section, South China. (**o–r**) Upper Clemente Formation at the CR-1 section, Cerro Rajón, Sonora State, Mexico. (**s–u**) Upper Clemente Formation at the CR-2 section, Cerro Rajón, Sonora State, Mexico. Data are from: cyan dots in **a** (McFadden *et al.* 2008); red dots in **a** (Ling *et al.* 2013); yellow dots in **a** (Zhou *et al.* 2012); **b** (Zhang *et al.* 2019); **c** and **d** (Cui *et al.* 2017; Zhang *et al.* 2019); **e** and **f** (Wei *et al.* 2021*b*); **g** (Li *et al.* 2010); **h** (Li *et al.* 2017); **i–l** (Cao *et al.* 2020); **m** (Zhu *et al.* 2007*b*; Ader *et al.* 2009; Kunimitsu *et al.* 2011; Cui *et al.* 2015; Furuyama *et al.* 2016); **o** and **s** (Loyd *et al.* 2012, 2013); **p** and **t** (Li *et al.* 2020*b*); **n**, **q**, **r** and **u** (this study).

seems that the seawater sulfate concentration in the outer-shelf environment was much higher than previously inferred; the interpretations of the δ^{34}S chemostratigraphy of some Ediacaran sections should therefore be revisited (Wang *et al.* 2021). Currently, most of our knowledge about the purported Ediacaran sulfate gradient model is based on the studies of the Doushantuo Formation (Li *et al.* 2010; Shi *et al.* 2018). More studies that compare correlative sections at different water depths are needed to test the sulfate gradient model in South China and other Ediacaran sedimentary basins.

Distribution of sulfate minerals

It is worth noting that not all the SE-equivalent sections preserve sulfate minerals. In fact, sulfate minerals have not been reported in most of the published SE-equivalent sections. There may be several reasons for this phenomenon. First, given the high solubility of gypsum and anhydrite, searching for these minerals in Precambrian strata is particularly challenging. It is possible that many evaporite sulfate minerals, once precipitated, may have soon dissolved away (Prince *et al.* 2019; Shields *et al.* 2019).

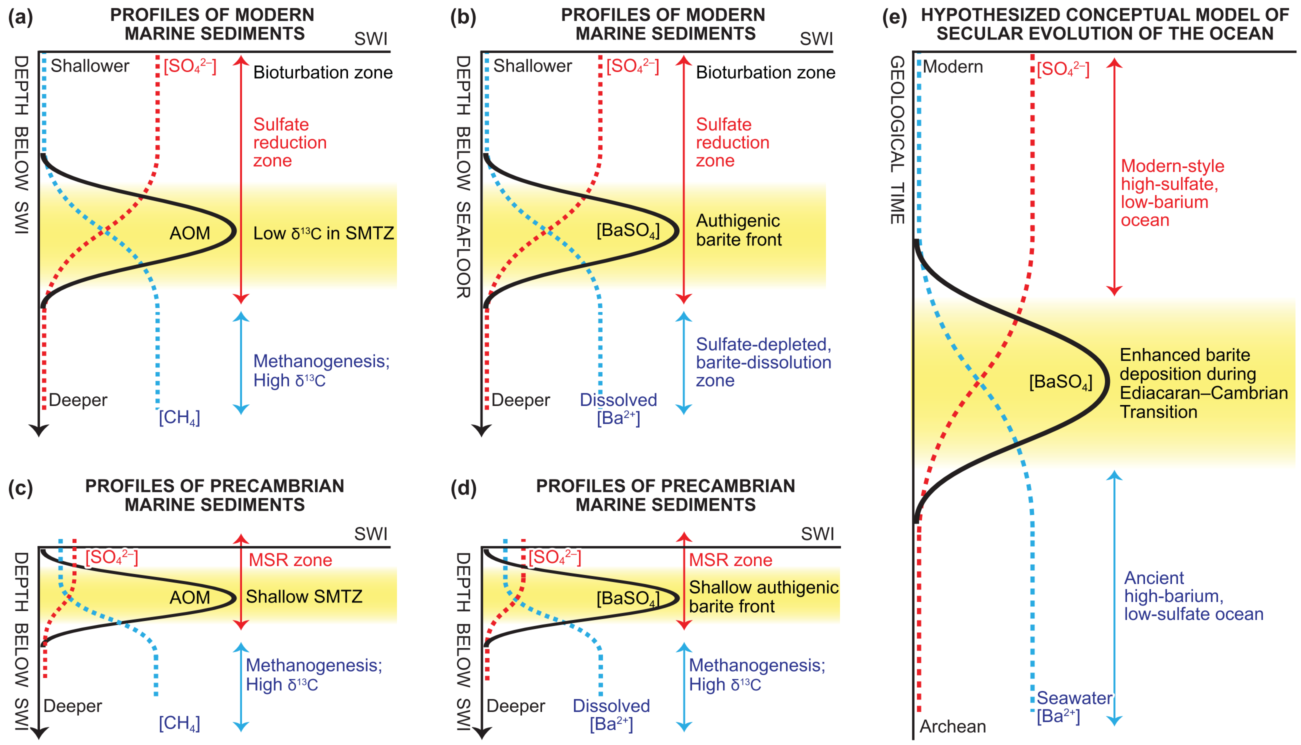

Fig. 16. Conceptual models for the biogeochemical carbon, sulfur and barium cycles. (**a**) [SO_4^{2-}] and methane [CH_4] profiles below the SWI in the modern marine environment. The interval shaded yellow shows the SMTZ, where the enhanced rate of sulfate-driven AOM typically leads to the mineralization of authigenic carbonate with extremely low $\delta^{13}C_{carb}$ signals. (**b**) [SO_4^{2-}] and dissolved barium [Ba^{2+}] profiles below the SWI in the modern marine environment. Typically, barite is most abundant in the base of the sulfate reduction zone (yellow interval), and is subjected to dissolution at a greater depth where sulfate is depleted (Torres *et al.* 1996; Gingele *et al.* 1999; Jørgensen 2006). (**c**, **d**) Hypothesized concentration profiles for marine sediments in the Precambrian ocean, where sulfate concentration was arguably much lower than that of the modern ocean. Note that the SMTZ and authigenic barite front are maintained at a much shallower depth due to the overall low concentration of seawater sulfate. (**e**) Hypothesized first-order trend in marine barium and sulfate concentrations throughout Earth history. Note that the *y* axis is deep time. Owing to the overall anoxic redox conditions of the Precambrian ocean, the dissolved barium concentration could be much higher than that in the modern ocean (Crockford *et al.* 2019*a*; Wei *et al.* 2021*a*). Therefore, a gradual increase in seawater sulfate concentration during the Ediacaran–Cambrian transition may have promoted barite deposition at that time (yellow interval; see also a mudrock-based study in Wei *et al.* 2021*a* for a comparison). When the seawater sulfate concentration reaches a modern level, dissolved barium in the ocean becomes depleted due to the quantitative removal of dissolved barium by sulfate. Short-term fluctuations in [CAS] and [Ba] – as found during the SE in this study – add more nuance to this first-order trend. See Appendix A for abbreviations.

Second, given the generally lower sulfate concentrations in Precambrian oceans relative to their modern counterparts, high sulfate levels were probably limited to restricted basins. Although multiple lines of evidence suggest a rise in sulfate during the Ediacaran–Cambrian transition, published chemostratigraphic studies indicate that the oxygenation events at that time might be local, transient and episodic (McFadden *et al.* 2008; Loyd *et al.* 2012; Sahoo *et al.* 2016; Cui *et al.* 2018; Wei *et al.* 2018; Zhang *et al.* 2018, 2019; Tostevin *et al.* 2019); and the complete ventilation of the deep ocean may have occurred much later (Sperling *et al.* 2015; Lu *et al.* 2018; Stolper and Keller 2018; Wei *et al.* 2021*a*).

Third, even in the modern marine environment with much higher levels of seawater sulfate (28 mM), the deposition of evaporite sulfate minerals strongly relies on local or regional hydrologic conditions, and is therefore not ubiquitous. Generally, local net evaporative conditions are required to concentrate seawater sulfate. This might explain why evaporative sulfate minerals in the Doushantuo Formation have only been found at relatively shallow water depths, including both the inner shelf (Fig. 3a, b) and rimmed outer-shelf shoal (Figs 4, S1–2) sections.

Nevertheless, sulfate minerals are largely associated with the SE and can occur below, within and/or above the SE interval (Fig. 1). What complements this scattered mineralogical dataset and reinforces the notion of increased sulfate concentrations during the SE is the high-resolution chemostratigraphic [CAS] and [Ba] profiles (Figs 14 and 15). These chemostratigraphic datasets show clear enrichments during the SE, and therefore support the view of a larger sulfate (and possibly Ba) reservoir at that time. A larger sulfate pool in the Ediacaran ocean may have played an essential role (as an oxidizer) in the genesis of the SE.

Barium cycle during the SE

In this study, all of the $[Ba]_{dilute\ acid}$ profiles reveal higher values during the SE compared with the pre- and post-SE intervals. This Ba enrichment is potentially consistent with higher concentrations of dissolved Ba^{2+} in Ediacaran seawater, and probably requires an increased barium influx to maintain the barium mass balance. However, the origin and source of this enhanced barium flux to both maintain higher marine [Ba] and an increased outflux to sediments remain unclear. Several hypotheses are conceivable and need further testing.

First, the higher $[Ba]_{dilute\ acid}$ values during the SE could result from an enhanced riverine Ba flux during a period of intensive chemical weathering. This scenario is supported by the higher $\delta^{138}Ba$ and higher $^{87}Sr/^{86}Sr$ signals in the EN3/DOUNCE interval relative to pre-SE intervals, which have been interpreted as reflecting a considerable contribution from a riverine source (Wei *et al.* 2021*b*).

Second, the higher $[Ba]_{dilute\ acid}$ values during the SE could be a local phenomenon triggered by upwelling events. In this scenario, a significant amount of dissolved Ba^{2+} accumulated in the anoxic

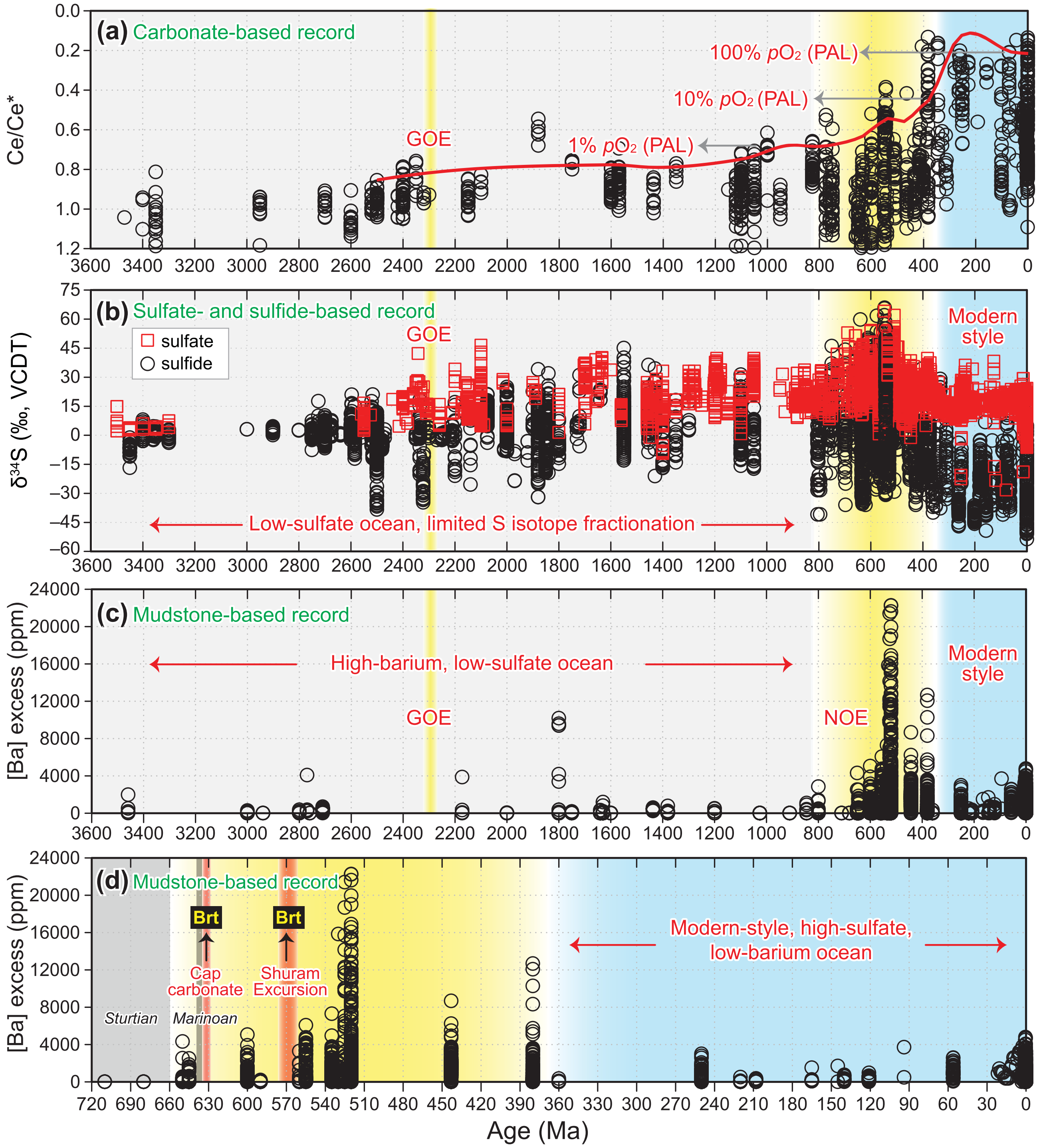

Fig. 17. Time-series Ce/Ce*, $\delta^{34}S$ and [Ba] data throughout Earth history. The grey interval represents the low-sulfate, high-barium ocean during most of the Precambrian. The yellow interval represents a period with increasing sulfate influx to the ocean and enhanced barite burial. The blue interval represents a period with a modern-style high-sulfate, low-barium ocean. (**a**) Compilation of Ce anomaly data. Note the reversed *y* axis of this panel. The red line indicates the best fit for 100 Ma intervals using the local polynomial regression curve fitting method. Estimated partial pressures of atmospheric oxygen, pO_2 (% PAL), throughout Earth history are also provided (Liu *et al.* 2021). (**b**) Compilation of $\delta^{34}S$ values of sulfate (empty squares) and sulfide (empty circles) in sedimentary records. (**c**) Excess [Ba] values based on a compilation of mudstones in Earth history. These values are calculated on the basis of measured [Ba] substracted by the Ba component of a detrital source (Wei *et al.* 2021*a*). (**d**) A closer view of the mudstone-based [Ba] record since the beginning of the Cryogenian Period. In light of this study (i.e. a carbonate-based compilation specifically for the SE), the Ediacaran Period may have witnessed at least two episodes of enhanced barite precipitation on a global scale: during the deposition of the cap carbonate (Hoffman *et al.* 2011) and during the SE (this study). Both of the above-mentioned episodes are characterized by negative $\delta^{13}C_{carb}$ signals and enhanced barite mineralization, which was probably driven by enhanced sulfate influx into an increasingly oxygenated ocean. Data are from: Ce/Ce* data and estimated pO_2 (Liu *et al.* 2021); $\delta^{34}S$ data (Canfield 1998; Canfield and Raiswell 1999; Canfield and Farquhar 2009; Och and Shields-Zhou 2012; Sahoo *et al.* 2012; Cui *et al.* 2016*b*, 2016*c*; Crockford *et al.* 2019*b*); [Ba] data (Wei *et al.* 2021*a*); age constraint for the GOE (Luo *et al.* 2016); age constraint for the two Snowball Earth glaciations (Rooney *et al.* 2015); age constraints for the SE (Rooney *et al.* 2020). See Appendix A for abbreviations.

deep basin might be transferred to shallow shelf environments via upwelling during the SE. Here, Ba^{2+} and nutrient-rich waters may have stimulated intense primary productivity and allowed significant transport of barium to sediments via barite formation associated with organic matter (Horner *et al.* 2017). This scenario is appealing because it also explains the low $\delta^{13}C$ signals during the SE. The oxidation of a putative large dissolved organic carbon (DOC) reservoir could transfer a significant amount of light carbon from the deep basin to shallow to seawater, leading to the SE (Rothman *et al.* 2003; Fike *et al.* 2006; McFadden *et al.* 2008; Shields *et al.* 2019).

Third, following on from the second hypothesis and considering that barite has been widely used as a proxy for palaeoproductivity (Dymond *et al.* 1992; Carter *et al.* 2020; Yao *et al.* 2020), it is possible that enhanced local primary productivity during the SE facilitated barite mineralization and burial at that time. However, the use of barite as a palaeoproductivity proxy is based on studies of the highly oxygenated, sulfate-rich, modern-style ocean (Dymond *et al.* 1992). Whether these dynamics directly translate to Precambrian oceans requires further study. Therefore, caution needs to be exercised when applying this proxy to the Precambrian strata.

Fourth, it has been proposed that a gas hydrate reservoir could potentially store a large amount of dissolved barium (Dickens *et al.* 2003), essentially serving as a barium capacitor. Oxidizing this potential barium reservoir could release both light C and dissolved Ba^{2+} to the ocean, leading to coupled C and Ba anomalies. The massive release of methane from clathrate hydrates has been invoked for both the Paleocene–Eocene Thermal Maximum event (Dickens *et al.* 2003) and the SE (Bjerrum and Canfield 2011). How it affected the Ba cycle in the case of the SE remains to be determined.

Fifth, enhanced phosphate levels in the Ediacaran ocean during the SE may have also played a role in facilitating barite mineralization. It has been shown that barite saturation and mineralization can occur in microenvironments where barium binds to phosphate groups (Martinez-Ruiz *et al.* 2019). In such a microenvironment, barium sorbs onto phosphate, which is then slowly substituted by sulfate, leading to the genesis of barite crystals (Horner *et al.* 2017; Martinez-Ruiz *et al.* 2019). This phosphate-shuttle mechanism is particularly appealing given that enhanced phosphogenesis has been found during the SE (Muscente *et al.* 2015; Cui *et al.* 2016*a*).

Sixth, upwelling or discharge of a euxinic water mass that is rich in both sulfide and barium could have caused enhanced barite deposition in the ocean (Jewell 2000). This mechanism could explain the concentration enrichments of both [CAS] and [Ba] during the SE. Oxidation of such a sulfide- and barium-rich water mass along chemocline is also consistent with the view of a redox-stratified Ediacaran ocean at that time (Li *et al.* 2010, 2015, 2020*a*; Ader *et al.* 2014).

It is worth mentioning that the above hypotheses are not mutually exclusive. It is possible that multiple controlling factors may have played a role in this coupled Ba and C cycle. Open questions about whether these potential processes occur at a local, regional or global scales, and in restricted or open oceans, still remain. More studies are therefore needed to test these hypotheses.

Barium burial in Earth history

Here, based on the secular trends of Ce/Ce*, $\delta^{34}S$ and [Ba] compilations (Fig. 17), three stages of barite burial can be recognized. (1) Before the Neoproterozoic, the ocean was largely anoxic, with a low concentration of sulfate. This is evidenced by relatively high Ce/Ce* in carbonates, limited S isotope fractionation between sulfate and sulfide and low barite burial. The dissolved barium concentration in Precambrian times could have been much higher than that of the modern ocean due to the more anoxic redox conditions (Crockford *et al.* 2019*a*). It was recently estimated that the marine dissolved Ba reservoir during the Neoproterozoic was potentially three orders of magnitude larger than that of the modern ocean (Wei *et al.* 2021*a*); however, this hypothesis requires further evaluation.

(2) The Ediacaran–Cambrian transition may have witnessed a rise in sulfate concentrations and barite mineralization that were locally amplified in an increasingly oxygenated ocean. The evidence for this scenario comprises increasingly lower Ce/Ce* in carbonates, much larger S isotope fractionation between sulfate and sulfide, and significantly enhanced barite deposition. Enhanced chemical weathering potentially tied to oxygenation during the Ediacaran–Cambrian transition could also bring a larger Ba flux into the ocean, further contributing to enhanced barite burial.

Together with the published compilation of barite within early Ediacaran cap carbonates (Shields *et al.* 2007; Bao *et al.* 2008; Zhou *et al.* 2010; Hoffman *et al.* 2011; Peng *et al.* 2011; Killingsworth *et al.* 2013; Macdonald *et al.* 2013; Bold *et al.* 2016; Crockford *et al.* 2016, 2018; Okubo *et al.* 2020), our study suggests that the Ediacaran Period witnessed at least two episodes of enhanced barite burial on a global scale: during the deposition of the cap carbonate, and during the SE (Fig. 17d) (Table 3). Both episodes are characterized by negative $\delta^{13}C_{carb}$ excursions and enhanced barite mineralization, which are probably driven by intensive oxidative weathering and greater influx of sulfate and barium into the depositional basin.

The model of enhanced barite burial is potentially consistent with positive shifts in $\delta^{138}Ba$ during the EN3/DOUNCE (Fig. 15f). This positive shift in $\delta^{138}Ba$ has been interpreted as resulting from enhanced riverine Ba fluxes into the intra-shelf basin (Wei *et al.* 2021*b*). Alternatively, given that barite is the major sink of light Ba (Horner *et al.* 2017; Horner and Crockford 2021) and that barite cements do exist within the EN3/DOUNCE interval (Figs 3c, d, 10–13), enhanced burial of barite during EN3/DOUNCE may have promoted the removal of light Ba from the intra-shelf environment, driving the seawater $\delta^{138}Ba$ of the intra-shelf basin towards increasingly higher values.

(3) For the last *c.* 400 Ma years, the ocean may have evolved to a modern-style, fully oxygenated, high-sulfate and low-barium conditions. The low Ce/Ce* signals in carbonates, much lower $\delta^{34}S$ values and limited barite content in the rock record are evidence of this stage. Statistical evaluations of global datasets throughout Earth history will be essential to test this inferred evolution (Farrell *et al.* 2021; Mehra *et al.* 2021).

Conclusions

To test the potential role of sulfate in the SE, we revisited 15 SE-equivalent sections, including the upper Doushantuo Formation in South China, the Shuram Formation in Oman, the Wonoka Formation in Australia, the Krol B + C intervals in India, the Nama Group in Southern Namibia, the Rainstorm Member in the western USA, the upper Clemente Formation in Mexico and the Nikol'skaya, Alyanchskaya and Kholychskaya formations in Siberia. All of the above sections show sulfate minerals and/or enrichment in [CAS] in the SE intervals. The $\delta^{34}S$ values of sulfate and sulfide in the SE intervals, when available, show progressively decreasing values, suggesting a larger marine sulfur reservoir with enhanced input from a ^{34}S-depleted source.

In addition, we also actively searched for barite minerals and explored [Ba] in three SE sections. Detailed SEM-EDS investigation revealed that diagenetic barite is present in the most typical SE-equivalent interval (i.e. the Jiulongwan EN3 interval) in South China. Where [Ba] data are available, they show considerable enrichment within the SE.

On the basis of the close coupling of C, S and Ba signatures, we propose that enhanced weathering may have caused elevated seawater sulfate and barium concentrations during the SE. A larger sulfate pool in the Ediacaran ocean may have facilitated the precipitation of sulfate minerals, microbial sulfate reduction and anaerobic oxidation of organic matter (including methane), leading to the SE. The existence of sulfate minerals in SE-equivalent strata suggests that oxidant pools were not depleted at that time, which challenges previous modelling results by Bristow and Kennedy (2008). Our study highlights the dynamic interplay of the biogeochemical C, S and Ba cycles in an increasingly oxygenated Earth surface environment.

Acknowledgements This paper is a contribution to the JGS thematic collection 'Sulfur in the Earth System'. The authors thank Brian Hess (UW-Madison) and James Kern (UW-Madison) for assistance in thin section preparation; Bil Schneider (UW-Madison) and Stephan Borensztajn (IPGP) for assistance in the SEM laboratory; Chief Editor Graham Shields (UCL) and Subject Editor Rosalie Tostevin (UCT) for handling this manuscript; and three anonymous reviewers for constructive comments. Although the views expressed are those of the authors, many thoughts were refined via kind discussions with the following colleagues, which are listed not in any particular order: Wei Wei (USTC), Erwan Le Guerroué (Beicip Franlab), John Warren (Chulalongkorn & Saltwork Consultants), Graham Shields (UCL), Genming Luo (CUG-Wuhan), Weiqi Yao (SUSTech), Guang-Yi Wei (NJU), Zhiyong Lin (Münster), Jiarui Liu (UCLA), Zheng Gong (Yale), Ganqing Jiang (UNLV), Yi Ding (CDUT), Jon Husson (Victoria), Xiqiang Zhou (IGG-CAS), Mao Luo (NIGPAS), Zhou Wang (CUG-Wuhan), and Jan-Peter Duda (Tübingen). HC thanks Min Tang (YNU) and Yi-Liang Li (HKU) for providing the published modern gypsum photos; Erwan Le Guerroué (Beicip Franlab) for sharing the published Khufai chertified evaporite photo. This paper is dedicated to baby Ruogu Cui, who accompanied HC by his side most of the time when HC worked on this manuscript.

Funding HC acknowledges joint support from the CIFAR (Canadian Institute for Advanced Research) 'Earth 4D: Subsurface Science and Exploration' program at Université de Paris and University of Toronto. AJK acknowledges National Science Foundation (NSF-EAR2020593). SX acknowledges NASA Exobiology for support (80NSSC18K1086). MZ and CZ acknowledge the support from the Strategic Priority Research Program (B) of the Chinese Academy of Sciences (XDB18000000, XDB26000000) and National Natural Science Foundation of China (41921002).

Conflict of interests The authors declare that they have no known competing financial interests or personal relationships that could have appeared to influence the work reported in this paper.

Author contributions **HC**: conceptualization (lead), data curation (lead), investigation (lead), project administration (lead), writing – original draft (lead), writing – review & editing (lead); **AJK**: writing – review & editing (supporting); **SX**: writing – review & editing (supporting); **CZ**: writing – review & editing (supporting); **MZ**: writing – review & editing (supporting); **MC**: writing – review & editing (supporting); **SL**: writing – review & editing (supporting); **PC**: writing – review & editing (supporting); **X-ML**: writing – review & editing (supporting); **SG**: writing – review & editing (supporting); **WW**: writing – review & editing (supporting); **CG**: writing – review & editing (supporting)

Data availability All data generated or analysed during this study are included in this published article.

Appendix

Appendix A: Abbreviations used

AOM, anaerobic oxidation of methane; Brt, barite; BSE, backscattered electron; Cal, calcite; Cam, Cambrian; CAS, carbonate-associated sulfate; Cryo, Cryogenian; DOUNCE, Doushantuo negative carbon isotope excursion; DDH, Dongdahe section; Dol, dolomite; EDS, Energy-dispersive spectroscopy; EN, Ediacaran negative excursion; EP, Ediacaran positive excursion; GOE, Great Oxygenation Event; JLW, Jiulongwan section; NBZ, Nanbeizhen section; NOE, Neoproterozoic Oxygenation Event; PAL, present atmospheric level; Phos.Dol, phosphatic dolomite; PPL, plane polarized light; Py, pyrite; Qz, quartz; SDP, Siduping section; SE in text, Shuram excursion; SE in SEM images, secondary electron; SEM, scanning electron microscope; SMTZ, sulfate–methane transition zone; SWI, sediment–water interface; TOC, total organic carbon; VCDT, Vienna Canyon Diablo Troilite; VPDB, Vienna Pee Dee Belemnite; XPL, cross polarized light; XRD, X-ray diffraction; YJP, Yangjiaping section; ZL, Zhongling section; µXRF, micro X-ray fluorescence.

Scientific editing by Rosalie Tostevin

Correction notice An incorrect Figure 1, part A was reproduced in the original version. The publisher apologizes for this error.

References

Ader, M., Macouin, M., Trindade, R.I.F., Hadrien, M.-H., Yang, Z., Sun, Z. and Besse, J. 2009. A multilayered water column in the Ediacaran Yangtze platform? Insights from carbonate and organic matter paired $\delta^{13}C$. *Earth and Planetary Science Letters*, **288**, 213–227, https://doi.org/10.1016/j.epsl.2009.09.024

Ader, M., Sansjofre, P., Halverson, G.P., Busigny, V., Trindade, R.I.F., Kunzmann, M. and Nogueira, A.C.R. 2014. Ocean redox structure across the Late Neoproterozoic Oxygenation Event: a nitrogen isotope perspective. *Earth and Planetary Science Letters*, **396**, 1–13, https://doi.org/10.1016/j.epsl.2014.03.042

Algeo, T.J., Luo, G.M., Song, H.Y., Lyons, T.W. and Canfield, D.E. 2015. Reconstruction of secular variation in seawater sulfate concentrations. *Biogeosciences*, **12**, 2131–2151, https://doi.org/10.5194/bg-12-2131-2015

An, Z., Jiang, G., Tong, J., Tian, L., Ye, Q., Song, H. and Song, H. 2015. Stratigraphic position of the Ediacaran Miaohe biota and its constrains on the age of the upper Doushantuo $\delta^{13}C$ anomaly in the Yangtze Gorges area, South China. *Precambrian Research*, **271**, 243–253, https://doi.org/10.1016/j.precamres.2015.10.007

Arndt, N. 2015. Sulfate minerals. *In*: Gargaud, M., Irvine, W.M. *et al.* (eds) *Encyclopedia of Astrobiology*. Springer, Berlin, 2409–2409, https://doi.org/10.1007/978-3-662-44185-5_1534

Bao, H. 2015. Sulfate: a time capsule for Earth's O_2, O_3, and H_2O. *Chemical Geology*, **395**, 108–118, https://doi.org/10.1016/j.chemgeo.2014.11.025

Bao, H., Lyons, J. and Zhou, C. 2008. Triple oxygen isotope evidence for elevated CO_2 levels after a Neoproterozoic glaciation. *Nature*, **453**, 504–506, https://doi.org/10.1038/nature06959

Bergmann, K.D. 2013. *Constraints on the Carbon Cycle and Climate During the Early Evolution of Animals*. PhD thesis, California Institute of Technology, https://dx.doi.org/10.7907/KFJX-7S28

Bergmann, K.D., Zentmyer, R.A. and Fischer, W.W. 2011. The stratigraphic expression of a large negative carbon isotope excursion from the Ediacaran Johnnie Formation, Death Valley. *Precambrian Research*, **188**, 45–56, https://doi.org/10.1016/j.precamres.2011.03.014

Berner, E.K. and Berner, R.A. 2012. *Global Environment: Water, Air, and Geochemical Cycles*. Princeton University Press.

Bjerrum, C.J. and Canfield, D.E. 2011. Towards a quantitative understanding of the late Neoproterozoic carbon cycle. *Proceedings of the National Academy of Sciences*, **108**, 5542–5547, https://doi.org/10.1073/pnas.1101755108

Blättler, C.L., Claire, M.W. *et al.* 2018. Two-billion-year-old evaporites capture Earth's great oxidation. *Science*, **360**, 320–323, https://doi.org/10.1126/science.aar2687

Blättler, C.L., Bergmann, K.D., Kah, L.C., Gómez-Pérez, I. and Higgins, J.A. 2020. Constraints on Meso- to Neoproterozoic seawater from ancient evaporite deposits. *Earth and Planetary Science Letters*, **532**, 115951, https://doi.org/10.1016/j.epsl.2019.115951

Bold, U., Smith, E.F. *et al.* 2016. Neoproterozoic stratigraphy of the Zavkhan terrane of Mongolia: the backbone for Cryogenian and early Ediacaran chemostratigraphic records. *American Journal of Science*, **316**, 1–63, https://doi.org/10.2475/01.2016.01

Bowles, M.W., Mogollón, J.M., Kasten, S., Zabel, M. and Hinrichs, K.-U. 2014. Global rates of marine sulfate reduction and implications for sub–sea-floor metabolic activities. *Science*, **344**, 889–891, https://doi.org/10.1126/science.1249213

Bridger, P., Poulton, S.W., Zhou, Y., Li, C., Zhang, K. and Shields, G.A. 2021. The Ediacaran 'Miaohe Member' of South China: new insights from palaeoredox proxies and stable isotope data. *Geological Magazine*, 1–15, https://doi.org/10.1017/S0016756821000261

Bristow, T.F. and Grotzinger, J.P. 2013. Sulfate availability and the geological record of cold-seep deposits. *Geology*, **41**, 811–814, https://doi.org/10.1130/G34265.1

Bristow, T.F. and Kennedy, M.J. 2008. Carbon isotope excursions and the oxidant budget of the Ediacaran atmosphere and ocean. *Geology*, **36**, 863–866, https://doi.org/10.1130/G24968A.1

Bristow, T.F., Bonifacie, M., Derkowski, A., Eiler, J.M. and Grotzinger, J.P. 2011. A hydrothermal origin for isotopically anomalous cap dolostone cements from south China. *Nature*, **474**, 68–71, https://doi.org/10.1038/nature10096

Burns, S.J., Haudenschild, U. and Matter, A. 1994. The strontium isotopic composition of carbonates from the late Precambrian (∼560–540 Ma) Huqf

Group of Oman. *Chemical Geology*, **111**, 269–282, https://doi.org/10.1016/0009-2541(94)90094-9

Calver, C.R. 2000. Isotope stratigraphy of the Ediacarian (Neoproterozoic III) of the Adelaide Rift Complex, Australia, and the overprint of water column stratification. *Precambrian Research*, **100**, 121–150, https://doi.org/10.1016/S0301-9268(99)00072-8

Canfield, D.E. 1998. A new model for Proterozoic ocean chemistry. *Nature*, **396**, 450–453, https://doi.org/10.1038/24839

Canfield, D.E. and Farquhar, J. 2009. Animal evolution, bioturbation, and the sulfate concentration of the oceans. *Proceedings of the National Academy of Sciences*, **106**, 8123–8127, https://doi.org/10.1073/pnas.0902037106

Canfield, D.E. and Raiswell, R. 1999. The evolution of the sulfur cycle. *American Journal of Science*, **299**, 697–723, https://doi.org/10.2475/ajs.299.7-9.697

Cantine, M.D., Knoll, A.H. and Bergmann, K.D. 2020. Carbonates before skeletons: a database approach. *Earth-Science Reviews*, **201**, 103065, https://doi.org/10.1016/j.earscirev.2019.103065

Cao, M., Daines, S.J. *et al.* 2020. Comparison of Ediacaran platform and slope δ^{238}U records in South China: implications for global-ocean oxygenation and the origin of the Shuram Excursion. *Geochimica et Cosmochimica Acta*, **287**, 111–124, https://doi.org/10.1016/j.gca.2020.04.035

Carter, S.C., Paytan, A. and Griffith, E.M. 2020. Toward an improved understanding of the marine barium cycle and the application of marine barite as a paleoproductivity proxy. *Minerals*, **10**, 421, https://doi.org/10.3390/min10050421

Chen, Z., Zhou, C., Meyer, M., Xiang, K., Schiffbauer, J.D., Yuan, X. and Xiao, S. 2013. Trace fossil evidence for Ediacaran bilaterian animals with complex behaviors. *Precambrian Research*, **224**, 690–701, https://doi.org/10.1016/j.precamres.2012.11.004

Claypool, G.E., Holser, W.T., Kaplan, I.R., Sakai, H. and Zak, I. 1980. The age curves of sulfur and oxygen isotopes in marine sulfate and their mutual interpretation. *Chemical Geology*, **28**, 199–260, https://doi.org/10.1016/0009-2541(80)90047-9

Condon, D., Zhu, M., Bowring, S., Wang, W., Yang, A. and Jin, Y. 2005. U–Pb ages from the Neoproterozoic Doushantuo Formation, China. *Science*, **308**, 95–98, https://doi.org/10.1126/science.1107765

Corsetti, F.A. and Kaufman, A.J. 2003. Stratigraphic investigations of carbon isotope anomalies and Neoproterozoic ice ages in Death Valley, California. *Geological Society of America Bulletin*, **115**, 916–932, https://doi.org/10.1130/B25066.1

Crockford, P.W., Cowie, B.R. *et al.* 2016. Triple oxygen and multiple sulfur isotope constraints on the evolution of the post-Marinoan sulfur cycle. *Earth and Planetary Science Letters*, **435**, 74–83, https://doi.org/10.1016/j.epsl.2015.12.017

Crockford, P.W., Hodgskiss, M.S.W., Uhlein, G.J., Caxito, F., Hayles, J.A. and Halverson, G.P. 2018. Linking paleocontinents through triple oxygen isotope anomalies. *Geology*, **46**, 179–182, https://doi.org/10.1130/G39470.1

Crockford, P.W., Wing, B.A. *et al.* 2019*a*. Barium-isotopic constraints on the origin of post-Marinoan barites. *Earth and Planetary Science Letters*, **519**, 234–244, https://doi.org/10.1016/j.epsl.2019.05.018

Crockford, P.W., Kunzmann, M. *et al.* 2019*b*. Claypool continued: extending the isotopic record of sedimentary sulfate. *Chemical Geology*, **513**, 200–225, https://doi.org/10.1016/j.chemgeo.2019.02.030

Cui, H., Kaufman, A.J., Xiao, S., Zhu, M., Zhou, C. and Liu, X.-M. 2015. Redox architecture of an Ediacaran ocean margin: integrated chemostratigraphic (δ^{13}C–δ^{34}S–^{87}Sr/^{86}Sr–Ce/Ce*) correlation of the Doushantuo Formation, South China. *Chemical Geology*, **405**, 48–62, https://doi.org/10.1016/j.chemgeo.2015.04.009

Cui, H., Xiao, S., Zhou, C., Peng, Y., Kaufman, A.J. and Plummer, R.E. 2016*a*. Phosphogenesis associated with the Shuram excursion: petrographic and geochemical observations from the Ediacaran Doushantuo Formation of South China. *Sedimentary Geology*, **341**, 134–146, https://doi.org/10.1016/j.sedgeo.2016.05.008

Cui, H., Grazhdankin, D.V. *et al.* 2016*b*. Redox-dependent distribution of early macro-organisms: evidence from the terminal Ediacaran Khatyspyt Formation in Arctic Siberia. *Palaeogeography, Palaeoclimatology, Palaeoecology*, **461**, 122–139, https://doi.org/10.1016/j.palaeo.2016.08.015

Cui, H., Kaufman, A.J. *et al.* 2016*c*. Environmental context for the terminal Ediacaran biomineralization of animals. *Geobiology*, **14**, 344–363, https://doi.org/10.1111/gbi.12178

Cui, H., Kaufman, A.J., Xiao, S., Zhou, C. and Liu, X.-M. 2017. Was the Ediacaran Shuram Excursion a globally synchronized early diagenetic event? Insights from methane-derived authigenic carbonates in the uppermost Doushantuo Formation, South China. *Chemical Geology*, **450**, 59–80, https://doi.org/10.1016/j.chemgeo.2016.12.010

Cui, H., Kaufman, A.J., Peng, Y., Liu, X.-M., Plummer, R.E. and Lee, E.I. 2018. The Neoproterozoic Hüttenberg δ^{13}C anomaly: genesis and global implications. *Precambrian Research*, **313**, 242–262, https://doi.org/10.1016/j.precamres.2018.05.024

Cui, H., Xiao, S., Cai, Y., Peek, S., Plummer, R.E. and Kaufman, A.J. 2019*a*. Sedimentology and chemostratigraphy of the terminal Ediacaran Dengying Formation at the Gaojiashan section, South China. *Geological Magazine*, **156**, 1924–1948, https://doi.org/10.1017/S0016756819000293

Cui, H., Orland, I.J. *et al.* 2019*b*. Probing an atypical Shuram Excursion by SIMS. Geological Society of America Abstracts with Programs, GSA Annual Meeting, Phoenix, Arizona, USA, **51**, https://doi.org/10.1130/abs/2019AM-332454

Cui, H., Orland, I.J. *et al.* 2019*c*. Ice or fire? Constraining the origin of isotopically anomalous cap carbonate cements by SIMS. Geological Society of America Abstracts with Programs, GSA Annual Meeting, Phoenix, Arizona, USA, **51**, https://doi.org/10.1130/abs/2019AM-332456

Cui, H., Kaufman, A.J. *et al.* 2020. Primary or secondary? A dichotomy of the strontium isotope anomalies in the Ediacaran carbonates of Saudi Arabia. *Precambrian Research*, **343**, 105720, https://doi.org/10.1016/j.precamres.2020.105720

Cui, H., Kitajima, K. *et al.* 2021. Deposition or diagenesis? Probing the Ediacaran Shuram excursion in South China by SIMS. *Global and Planetary Change*, **206**, 103591 https://doi.org/10.1016/j.gloplacha.2021.103591

Darroch, S.A.F., Smith, E.F., Laflamme, M. and Erwin, D.H. 2018. Ediacaran extinction and Cambrian Explosion. *Trends in Ecology & Evolution*, **33**, 653–663, https://doi.org/10.1016/j.tree.2018.06.003

Derry, L.A. 2010. A burial diagenesis origin for the Ediacaran Shuram–Wonoka carbon isotope anomaly. *Earth and Planetary Science Letters*, **294**, 152–162, https://doi.org/10.1016/j.epsl.2010.03.022

Dickens, G.R. 2001. Sulfate profiles and barium fronts in sediment on the Blake Ridge: present and past methane fluxes through a large gas hydrate reservoir. *Geochimica et Cosmochimica Acta*, **65**, 529–543, https://doi.org/10.1016/S0016-7037(00)00556-1

Dickens, G.R., Fewless, T., Thomas, E. and Bralower, T.J. 2003. Excess barite accumulation during the Paleocene–Eocene thermal maximum: massive input of dissolved barium from seafloor gas hydrate reservoirs. *Geological Society of America Special Paper*, **369**, 11–24, https://doi.org/10.1130/0-8137-2369-8.11

Ding, Y., Chen, D., Zhou, X., Guo, C., Huang, T. and Zhang, G. 2019. Cavity-filling dolomite speleothems and submarine cements in the Ediacaran Dengying microbialites, South China: responses to high-frequency sea-level fluctuations in an 'aragonite–dolomite sea'. *Sedimentology*, **66**, 2511–2537, https://doi.org/10.1111/sed.12605

Duda, J.-P., Zhu, M. and Reitner, J. 2015. Depositional dynamics of a bituminous carbonate facies in a tectonically induced intra-platform basin: the Shibantan Member (Dengying Formation, Ediacaran Period). *Carbonates and Evaporites*, **31**, 87–99, https://doi.org/10.1007/s13146-015-0243-8

Dymond, J., Suess, E. and Lyle, M. 1992. Barium in deep-sea sediment: a geochemical proxy for paleoproductivity. *Paleoceanography*, **7**, 163–181, https://doi.org/10.1029/92PA00181

Fang, X., Wu, L., Geng, A. and Deng, Q. 2019. Formation and evolution of the Ediacaran to Lower Cambrian black shales in the Yangtze Platform, South China. *Palaeogeography, Palaeoclimatology, Palaeoecology*, **527**, 87–102, https://doi.org/10.1016/j.palaeo.2019.04.025

Farrell, Ú.C., Samawi, R. *et al.* 2021. The sedimentary geochemistry and paleoenvironments project. *Geobiology*, first published online 5 July 2021, https://doi.org/10.1111/gbi.12462

Fike, D.A. and Grotzinger, J.P. 2008. A paired sulfate–pyrite δ^{34}S approach to understanding the evolution of the Ediacaran–Cambrian sulfur cycle. *Geochimica et Cosmochimica Acta*, **72**, 2636–2648, https://doi.org/10.1016/j.gca.2008.03.021

Fike, D.A. and Grotzinger, J.P. 2010. A δ^{34}S$_{SO4}$ approach to reconstructing biogenic pyrite burial in carbonate–evaporite basins: An example from the Ara Group, Sultanate of Oman. *Geology*, **38**, 371–374, https://doi.org/10.1130/G30230.1

Fike, D.A., Grotzinger, J.P., Pratt, L.M. and Summons, R.E. 2006. Oxidation of the Ediacaran ocean. *Nature*, **444**, 744–747, https://doi.org/10.1038/nature05345

Furuyama, S., Kano, A., Kunimitsu, Y., Ishikawa, T. and Wei, W. 2016. Diagenetic overprint to a negative carbon isotope anomaly associated with the Gaskiers glaciation of the Ediacaran Doushantuo Formation in South China. *Precambrian Research*, **276**, 110–122, https://doi.org/10.1016/j.precamres.2016.01.004

Gingele, F.X., Zabel, M., Kasten, S., Bonn, W.J. and Nürnberg, C.C. 1999. Biogenic Barium as a Proxy for Paleoproductivity: Methods and Limitations of Application. *In*: Fischer, G., Wefer, G. (eds) *Use of Proxies in Paleoceanography: Examples from the South Arlantic*. Springer Berlin Heidelberg, Berlin, 345–364, https://doi.org/10.1007/978-3-642-58646-0_13

Gong, Z. and Li, M. 2020. Astrochronology of the Ediacaran Shuram carbon isotope excursion, Oman. *Earth and Planetary Science Letters*, **547**, 116462, https://doi.org/10.1016/j.epsl.2020.116462

Gorin, G.E., Racz, L.G. and Walter, M.R. 1982. Late Precambrian-Cambrian sediments of Huqf Group, Sultanate of Oman. *AAPG Bulletin*, **66**, 2609–2627, https://doi.org/10.1306/03B5AC82-16D1-11D7-8645000102C1865D

Grotzinger, J. and Al-Rawahi, Z. 2014. Depositional facies and platform architecture of microbialite-dominated carbonate reservoirs, Ediacaran–Cambrian Ara Group, Sultanate of Oman. *AAPG Bulletin*, **98**, 1453–1494, https://doi.org/10.1306/02271412063

Grotzinger, J.P. and Kasting, J.F. 1993. New constraints on Precambrian ocean composition. *The Journal of Geology*, **101**, 235–243, https://doi.org/10.1086/648218

Grotzinger, J.P., Fike, D.A. and Fischer, W.W. 2011. Enigmatic origin of the largest-known carbon isotope excursion in Earth's history. *Nature Geoscience*, **4**, 285–292, https://doi.org/10.1038/ngeo1138

Habicht, K.S., Gade, M., Thamdrup, B., Berg, P. and Canfield, D.E. 2002. Calibration of sulfate levels in the Archean ocean. *Science*, **298**, 2372–2374, https://doi.org/10.1126/science.1078265

Hardie, L.A. 2003. Anhydrite and gypsum. *In*: Middleton, G.V., Church, M.J., Coniglio, M., Hardie, L.A. and Longstaffe, F.J. (eds) *Encyclopedia of Sediments and Sedimentary Rocks*. Springer Netherlands, Dordrecht, 16–19, https://doi.org/10.1007/978-1-4020-3609-5_7

Hoffman, P.F., Macdonald, F.A. and Halverson, G.P. 2011. Chapter 5. Chemical sediments associated with Neoproterozoic glaciation: iron formation, cap carbonate, barite and phosphorite. *In*: Arnaud, E., Halverson, G.P. and Shields-Zhou, G. (eds) *The Geological Record of Neoproterozoic Glaciations*. *Geological Society, London, Memoirs*, London, **1**, 67–80, https://doi.org/10.1144/m36.5

Holland, H.D. 1984. *The Chemical Evolution of the Atmosphere and Oceans*. Princeton University Press, Princeton, New Jersey, USA.

Horita, J., Zimmermann, H. and Holland, H.D. 2002. Chemical evolution of seawater during the Phanerozoic: implications from the record of marine evaporites. *Geochimica et Cosmochimica Acta*, **66**, 3733–3756, https://doi.org/10.1016/S0016-7037(01)00884-5

Horner, T.J. and Crockford, P.W. 2021. Barium isotopes: drivers, dependencies, and distributions through space and time. *In*: Lyons, T., Turchyn, A. and Reinhard, C. (eds) *Elements in Geochemical Tracers in Earth System Science*. Cambridge University Press, Cambridge, 1–34, https://doi.org/10.1017/9781108865845

Horner, T.J., Pryer, H.V., Nielsen, S.G., Crockford, P.W., Gauglitz, J.M., Wing, B.A. and Ricketts, R.D. 2017. Pelagic barite precipitation at micromolar ambient sulfate. *Nature Communications*, **8**, 1342, https://doi.org/10.1038/s41467-017-01229-5

Husson, J.M., Maloof, A.C., Schoene, B., Chen, C.Y. and Higgins, J.A. 2015. Stratigraphic expression of Earth's deepest $\delta^{13}C$ excursion in the Wonoka Formation of South Australia. *American Journal of Science*, **315**, 1–45, https://doi.org/10.2475/01.2015.01

Jewell, P.W. 2000. Bedded barite in the geologic record. *In*: Glenn, C.R., Prévôt-Lucas, L. and Lucas, J. (eds) *Marine Authigenesis: From Global to Microbial, SEPM Special Publication No. 66*. SEPM (Society for Sedimentary Geology), 147–161, https://doi.org/10.2110/pec.00.66.0147

Jiang, G., Christie-Blick, N., Kaufman, A.J., Banerjee, D.M. and Rai, V. 2002. Sequence stratigraphy of the Neoproterozoic infra Krol formation and Krol Group, lesser Himalaya, India. *Journal of Sedimentary Research*, **72**, 524–542, https://doi.org/10.1306/120301720524

Jiang, G., Kennedy, M.J. and Christie-Blick, N. 2003*a*. Stable isotopic evidence for methane seeps in Neoproterozoic postglacial cap carbonates. *Nature*, **426**, 822–826, https://doi.org/10.1038/nature02201

Jiang, G., Sohl, L.E. and Christie-Blick, N. 2003*b*. Neoproterozoic stratigraphic comparison of the Lesser Himalaya (India) and Yangtze block (south China): paleogeographic implications. *Geology*, **31**, 917–920, https://doi.org/10.1130/G19790.1

Jiang, G., Shi, X. and Zhang, S. 2006*a*. Methane seeps, methane hydrate destabilization, and the late Neoproterozoic postglacial cap carbonates. *Chinese Science Bulletin*, **51**, 1152–1173, https://doi.org/10.1007/s11434-006-1152-y

Jiang, G., Kennedy, M.J., Christie-Blick, N., Wu, H. and Zhang, S. 2006*b*. Stratigraphy, sedimentary structures, and textures of the late Neoproterozoic Doushantuo cap carbonate in South China. *Journal of Sedimentary Research*, **76**, 978–995, https://doi.org/10.2110/jsr.2006.086

Jiang, G., Kaufman, A.J., Christie-Blick, N., Zhang, S. and Wu, H. 2007. Carbon isotope variability across the Ediacaran Yangtze platform in South China: implications for a large surface-to-deep ocean $\delta^{13}C$ gradient. *Earth and Planetary Science Letters*, **261**, 303–320, https://doi.org/10.1016/j.epsl.2007.07.009

Jiang, G., Shi, X., Zhang, S., Wang, Y. and Xiao, S. 2011. Stratigraphy and paleogeography of the Ediacaran Doushantuo Formation (*c*. 635–551 Ma) in South China. *Gondwana Research*, **19**, 831–849, https://doi.org/10.1016/j.gr.2011.01.006

Jørgensen, B.B. 2006. Bacteria and Marine Biogeochemistry. *In*: Schulz, H.D., Zabel, M. (eds.) *Marine Geochemistry*. Springer Berlin Heidelberg, Berlin, Heidelberg, 173–207, https://doi.org/10.1007/978-3-662-04242-7_5

Jørgensen, B.B. and Kasten, S. 2006. Sulfur cycling and methane oxidation. *In*: Schulz, H.D. and Zabel, M. (eds) *Marine Geochemistry*. Springer, Berlin, 271–309, https://doi.org/10.1007/3-540-32144-6

Kah, L.C., Lyons, T.W. and Chesley, J.T. 2001. Geochemistry of a 1.2 Ga carbonate-evaporite succession, northern Baffin and Bylot Islands: implications for Mesoproterozoic marine evolution. *Precambrian Research*, **111**, 203–234, https://doi.org/10.1016/S0301-9268(01)00161-9

Kah, L.C., Lyons, T.W. and Frank, T.D. 2004. Low marine sulphate and protracted oxygenation of the Proterozoic biosphere. *Nature*, **431**, 834–838, https://doi.org/10.1038/nature02974

Kaufman, A.J. 2005. The calibration of Ediacaran time. *Science*, **308**, 59–60, https://doi.org/10.1126/science.1111101

Kaufman, A.J., Jiang, G., Christie-Blick, N., Banerjee, D.M. and Rai, V. 2006. Stable isotope record of the terminal Neoproterozoic Krol platform in the Lesser Himalayas of northern India. *Precambrian Research*, **147**, 156–185, https://doi.org/10.1016/j.precamres.2006.02.007

Kaufman, A.J., Corsetti, F.A. and Varni, M.A. 2007. The effect of rising atmospheric oxygen on carbon and sulfur isotope anomalies in the Neoproterozoic Johnnie Formation, Death Valley, USA. *Chemical Geology*, **237**, 47–63, https://doi.org/10.1016/j.chemgeo.2006.06.023

Kaufman, A.J., Kriesfeld, L., Cui, H., Narbonne, G.M., Vickers-Rich, P., Zhou, C. and Xiao, S. 2015. An authigenic origin for the middle Ediacaran Shuram excursion: the view from Namibia and South China. Paper presented at the Geological Society of America Annual Meeting, Baltimore, Maryland, USA.

Killingsworth, B.A., Hayles, J.A., Zhou, C. and Bao, H. 2013. Sedimentary constraints on the duration of the Marinoan Oxygen-17 Depletion (MOSD) event. *Proceedings of the National Academy of Sciences*, **110**, 17686–17690, https://doi.org/10.1073/pnas.1213154110

Knauth, L.P. and Kennedy, M.J. 2009. The late Precambrian greening of the Earth. *Nature*, **460**, 728–732, https://doi.org/10.1038/nature08213

Kunimitsu, Y., Setsuda, Y., Furuyama, S., Wang, W. and Kano, A. 2011. Ediacaran chemostratigraphy and paleoceanography at a shallow marine setting in northwestern Hunan Province, South China. *Precambrian Research*, **191**, 194–208, https://doi.org/10.1016/j.precamres.2011.09.006

Le Guerroué, E. 2006. *Sedimentology and Chemostratigraphy of the Ediacaran Shuram Formation, Nafun Group, Oman*. PhD thesis, Eidgenössische Technische Hochschule Zürich (ETHZ).

Lee, C., Love, G.D., Fischer, W.W., Grotzinger, J.P. and Halverson, G.P. 2015. Marine organic matter cycling during the Ediacaran Shuram excursion. *Geology*, **43**, 1103–1106, https://doi.org/10.1130/g37236.1

Li, C., Love, G.D., Lyons, T.W., Fike, D.A., Sessions, A.L. and Chu, X. 2010. A stratified redox model for the Ediacaran ocean. *Science*, **328**, 80–83, https://doi.org/10.1126/science.1182369

Li, C., Cheng, M., Algeo, T.J. and Xie, S. 2015. A theoretical prediction of chemical zonation in early oceans (>520 Ma). *Science China Earth Sciences*, **58**, 1901–1909, https://doi.org/10.1007/s11430-015-5190-7

Li, C., Hardisty, D.S. *et al.* 2017. Uncovering the spatial heterogeneity of Ediacaran carbon cycling. *Geobiology*, **15**, 211–224, https://doi.org/10.1111/gbi.12222

Li, C., Shi, W., Cheng, M., Jin, C. and Algeo, T.J. 2020*a*. The redox structure of Ediacaran and early Cambrian oceans and its controls. *Science Bulletin*, **65**, 2141–2149, https://doi.org/10.1016/j.scib.2020.09.023

Li, Z., Cao, M. *et al.* 2020*b*. Transient and stepwise ocean oxygenation during the late Ediacaran Shuram Excursion: insights from carbonate $\delta^{238}U$ of northwestern Mexico. *Precambrian Research*, **344**, 105741, https://doi.org/10.1016/j.precamres.2020.105741

Lin, Z., Wang, Q., Feng, D., Liu, Q. and Chen, D. 2011. Post-depositional origin of highly ^{13}C-depleted carbonate in the Doushantuo cap dolostone in South China: insights from petrography and stable carbon isotopes. *Sedimentary Geology*, **242**, 71–79, https://doi.org/10.1016/j.sedgeo.2011.10.009

Ling, H.-F., Chen, X., Li, D., Wang, D., Shields-Zhou, G.A. and Zhu, M. 2013. Cerium anomaly variations in Ediacaran–earliest Cambrian carbonates from the Yangtze Gorges area, South China: implications for oxygenation of coeval shallow seawater. *Precambrian Research*, **225**, 110–127, https://doi.org/10.1016/j.precamres.2011.10.011

Liu, X.-M., Kah, L.C., Knoll, A.H., Cui, H., Kaufman, A.J., Shahar, A. and Hazen, R.M. 2016. Tracing Earth's O_2 evolution using Zn/Fe ratios in marine carbonates. *Geochemical Perspectives Letters*, **2**, 24–34, https://doi.org/10.7185/geochemlet.1603

Liu, X.-M., Kah, L.C., Knoll, A.H., Cui, H., Wang, C., Bekker, A. and Hazen, R.M. 2021. A persistently low level of atmospheric oxygen in Earth's middle age. *Nature Communications*, **12**, 351, https://doi.org/10.1038/s41467-020-20484-7

Loyd, S.J., Marenco, P.J., Hagadorn, J.W., Lyons, T.W., Kaufman, A.J., Sour-Tovar, F. and Corsetti, F.A. 2012. Sustained low marine sulfate concentrations from the Neoproterozoic to the Cambrian: insights from carbonates of northwestern Mexico and eastern California. *Earth and Planetary Science Letters*, **339–340**, 79–94, https://doi.org/10.1016/j.epsl.2012.05.032

Loyd, S.J., Marenco, P.J., Hagadorn, J.W., Lyons, T.W., Kaufman, A.J., Sour-Tovar, F. and Corsetti, F.A. 2013. Local $\delta^{34}S$ variability in *c.* 580 Ma carbonates of northwestern Mexico and the Neoproterozoic marine sulfate reservoir. *Precambrian Research*, **224**, 551–569, https://doi.org/10.1016/j.precamres.2012.10.007

Lu, M., Zhu, M. *et al.* 2013. The DOUNCE event at the top of the Ediacaran Doushantuo Formation, South China: broad stratigraphic occurrence and non-diagenetic origin. *Precambrian Research*, **225**, 86–109, https://doi.org/10.1016/j.precamres.2011.10.018

Lu, W., Ridgwell, A. *et al.* 2018. Late inception of a resiliently oxygenated upper ocean. *Science*, **361**, 174–177, https://doi.org/10.1126/science.aar5372

Luo, G., Ono, S., Beukes, N.J., Wang, D.T., Xie, S. and Summons, R.E. 2016. Rapid oxygenation of Earth's atmosphere 2.33 billion years ago. *Science Advances*, **2**, e1600134, https://doi.org/10.1126/sciadv.1600134

Luo, C., Pan, B. and Reitner, J. 2017. Chambered structures from the Ediacaran Dengying Formation, Yunnan, China: comparison with the Cryogenian analogues and their microbial interpretation. *Geological Magazine*, **154**, 1269–1284, https://doi.org/10.1017/S001675681700053X

Lyons, T.W., Reinhard, C.T. and Planavsky, N.J. 2014. The rise of oxygen in Earth's early ocean and atmosphere. *Nature*, **506**, 307–315, https://doi.org/10.1038/nature13068

Ma, Z., Gray, E., Thomas, E., Murphy, B., Zachos, J. and Paytan, A. 2014. Carbon sequestration during the Palaeocene–Eocene Thermal Maximum by an efficient biological pump. *Nature Geoscience*, **7**, 382–388, https://doi.org/10.1038/NGEO2139

Macdonald, F.A., Strauss, J.V. *et al.* 2013. The stratigraphic relationship between the Shuram carbon isotope excursion, the oxygenation of Neoproterozoic oceans, and the first appearance of the Ediacara biota and bilaterian trace fossils in northwestern Canada. *Chemical Geology*, **362**, 250–272, https://doi.org/10.1016/j.chemgeo.2013.05.032

Macouin, M., Besse, J., Ader, M., Gilder, S., Yang, Z., Sun, Z. and Agrinier, P. 2004. Combined paleomagnetic and isotopic data from the Doushantuo carbonates, South China: implications for the 'snowball Earth' hypothesis. *Earth and Planetary Science Letters*, **224**, 387–398, https://doi.org/10.1016/j.epsl.2004.05.015

Macouin, M., Ader, M., Moreau, M.-G., Poitou, C., Yang, Z. and Sun, Z. 2012. Deciphering the impact of diagenesis overprint on negative $\delta^{13}C$ excursions using rock magnetism: case study of Ediacaran carbonates, Yangjiaping section, South China. *Earth and Planetary Science Letters*, **351–352**, 281–294, https://doi.org/10.1016/j.epsl.2012.06.057

Marenco, P.J., Corsetti, F.A., Hammond, D.E., Kaufman, A.J. and Bottjer, D.J. 2008. Oxidation of pyrite during extraction of carbonate associated sulfate. *Chemical Geology*, **247**, 124–132, https://doi.org/10.1016/j.chemgeo.2007.10.006

Martinez-Ruiz, F., Paytan, A. *et al.* 2019. Barite formation in the ocean: origin of amorphous and crystalline precipitates. *Chemical Geology*, **511**, 441–451, https://doi.org/10.1016/j.chemgeo.2018.09.011

Matsu'ura, F., Nakada, R., Usui, T., Sawaki, Y., Ueno, Y., Kajitani, I. and Saitoh, M. 2021. Spatial distribution and speciation of sulfur in Ediacaran limestones with μ-XRF imaging and XANES spectroscopy: implications for diagenetic mobilization of sulfur species. *Geochimica et Cosmochimica Acta*, **306**, 20–43, https://doi.org/10.1016/j.gca.2021.05.010

McFadden, K.A., Huang, J. *et al.* 2008. Pulsed oxidation and biological evolution in the Ediacaran Doushantuo Formation. *Proceedings of the National Academy of Sciences*, **105**, 3197–3202, https://doi.org/10.1073/pnas.0708336105

Mehra, A., Keller, C.B. *et al.* 2021. Curation and analysis of global sedimentary geochemical data to inform Earth history. *GSA Today*, **31**, 4–10, https://doi.org/10.1130/GSATG484A.1

Meister, P. 2015. For the deep biosphere, the present is not always the key to the past: what we can learn from the geological record. *Terra Nova*, **27**, 400–408, https://doi.org/10.1111/ter.12174

Meister, P., McKenzie, J.A., Vasconcelos, C., Bernasconi, S., Frank, M., Gutjahr, M. and Schrag, D.P. 2007. Dolomite formation in the dynamic deep biosphere: results from the Peru Margin. *Sedimentology*, **54**, 1007–1032, https://doi.org/10.1111/j.1365-3091.2007.00870.x

Melezhik, V.A., Fallick, A.E., Rychanchik, D.V. and Kuznetsov, A.B. 2005. Palaeoproterozoic evaporites in Fennoscandia: implications for seawater sulphate, the rise of atmospheric oxygen and local amplification of the $\delta^{13}C$ excursion. *Terra Nova*, **17**, 141–148, https://doi.org/10.1111/j.1365-3121.2005.00600.x

Melezhik, V.A., Pokrovsky, B.G., Fallick, A.E., Kuznetsov, A.B. and Bujakaite, M.I. 2009. Constraints on $^{87}Sr/^{86}Sr$ of Late Ediacaran seawater: insight from Siberian high-Sr limestones. *Journal of the Geological Society*, *London*, **166**, 183–191, https://doi.org/10.1144/0016-76492007-171

Muscente, A.D., Hawkins, A.D. and Xiao, S. 2015. Fossil preservation through phosphatization and silicification in the Ediacaran Doushantuo Formation (South China): a comparative synthesis. *Palaeogeography, Palaeoclimatology, Palaeoecology*, **434**, 46–62, https://doi.org/10.1016/j.palaeo.2014.10.013

Och, L.M. and Shields-Zhou, G.A. 2012. The Neoproterozoic oxygenation event: environmental perturbations and biogeochemical cycling. *Earth-Science Reviews*, **110**, 26–57, https://doi.org/10.1016/j.earscirev.2011.09.004

Okubo, J., Klyukin, Y.I., Warren, L.V., Sublett, D.M., Bodnar, R.J., Gill, B.C. and Xiao, S. 2020. Hydrothermal influence on barite precipitates in the basal Ediacaran Sete Lagoas cap dolostone, São Francisco Craton, central Brazil. *Precambrian Research*, **340**, 105628, https://doi.org/10.1016/j.precamres.2020.105628

Osburn, M., Grotzinger, J. and Bergmann, K. 2014. Facies, stratigraphy, and evolution of a middle Ediacaran carbonate ramp: Khufai Formation, Sultanate of Oman. *AAPG Bulletin*, **98**, 1631–1667, https://doi.org/10.1306/07291312140

Paytan, A. and Gray, E.T. 2012. Sulfur isotope stratigraphy. *In*: Gradstein, F.M., Ogg, J.G., Schmitz, M.D. and Ogg, G.M. (eds) *The Geologic Time Scale*. Elsevier, Boston, 167–180, https://doi.org/10.1016/b978-0-444-59425-9.00009-3

Paytan, A. and Griffith, E.M. 2007. Marine barite: recorder of variations in ocean export productivity. *Deep Sea Research Part II: Topical Studies in Oceanography*, **54**, 687–705, https://doi.org/10.1016/j.dsr2.2007.01.007

Peng, Y., Bao, H., Zhou, C. and Yuan, X. 2011. ^{17}O-depleted barite from two Marinoan cap dolostone sections, South China. *Earth and Planetary Science Letters*, **305**, 21–31, https://doi.org/10.1016/j.epsl.2011.02.014

Peng, Y., Bao, H. *et al.* 2014. Widespread contamination of carbonate-associated sulfate by present-day secondary atmospheric sulfate: evidence from triple oxygen isotopes. *Geology*, **42**, 815–818, https://doi.org/10.1130/G35852.1

Peng, Y., Jiang, G., Bao, H., Xiao, S., Kaufman, A.J., Zhou, C. and Wang, J. 2015. Sulfate-driven anaerobic oxidation of methane as the origin of extremely ^{13}C-depleted calcite in the Doushantuo cap carbonates in South China. AGU Fall meeting, San Francisco, B21A-0408.

Peng, J., Zhang, H. and Lin, X. 2017. Study on characteristics and genesis of botryoidal dolostone of the Upper Sinian Dengying Formation: a case study from Hanyuan region, Sichuan, China. *Carbonates and Evaporites*, **33**, 285–299, https://doi.org/10.1007/s13146-017-0343-8

Pisarevsky, S.A., Murphy, J.B., Cawood, P.A. and Collins, A.S. 2008. Late Neoproterozoic and early Cambrian palaeogeography: models and problems. *Geological Society, London, Special Publications*, **294**, 9–31, https://doi.org/10.1144/SP294.2

Prince, J.K.G., Rainbird, R.H. and Wing, B.A. 2019. Evaporite deposition in the mid-Neoproterozoic as a driver for changes in seawater chemistry and the biogeochemical cycle of sulfur. *Geology*, **47**, 375–379, https://doi.org/10.1130/G45464.1

Reuschel, M., Melezhik, V., Whitehouse, M., Lepland, A., Fallick, A. and Strauss, H. 2012. Isotopic evidence for a sizeable seawater sulfate reservoir at 2.1 Ga. *Precambrian Research*, **192**, 78–88, https://doi.org/10.1016/j.precamres.2011.10.013

Riedinger, N., Kasten, S., Gröger, J., Franke, C. and Pfeifer, K. 2006. Active and buried authigenic barite fronts in sediments from the Eastern Cape Basin. *Earth and Planetary Science Letters*, **241**, 876–887, https://doi.org/10.1016/j.epsl.2005.10.032

Rooney, A.D., Strauss, J.V., Brandon, A.D. and Macdonald, F.A. 2015. A Cryogenian chronology: two long-lasting synchronous Neoproterozoic glaciations. *Geology*, **43**, 459–462, https://doi.org/10.1130/G36511.1

Rooney, A.D., Cantine, M.D. *et al.* 2020. Calibrating the coevolution of Ediacaran life and environment. *Proceedings of the National Academy of Sciences*, **117**, 16824–16830, https://doi.org/10.1073/pnas.2002918117

Rothman, D.H., Hayes, J.M. and Summons, R.E. 2003. Dynamics of the Neoproterozoic carbon cycle. *Proceedings of the National Academy of Sciences*, **100**, 8124–8129, https://doi.org/10.1073/pnas.0832439100

Sahoo, S.K., Planavsky, N.J. *et al.* 2012. Ocean oxygenation in the wake of the Marinoan glaciation. *Nature*, **489**, 546–549, https://doi.org/10.1038/nature11445

Sahoo, S.K., Planavsky, N.J. *et al.* 2016. Oceanic oxygenation events in the anoxic Ediacaran ocean. *Geobiology*, **14**, 457–468, https://doi.org/10.1111/gbi.12182

Santos, R.F.D., Nogueira, A.C.R., Romero, G.R., Soares, J.L. and Bandeira, J. 2021. Life in the aftermath of Marinoan glaciation: the giant stromatolite evolution in the Puga cap carbonate, southern Amazon Craton, Brazil. *Precambrian Research*, **354**, 106059, https://doi.org/10.1016/j.precamres.2020.106059

Sawaki, Y., Ohno, T. *et al.* 2010. The Ediacaran radiogenic Sr isotope excursion in the Doushantuo Formation in the Three Gorges area, South China. *Precambrian Research*, **176**, 46–64, https://doi.org/10.1016/j.precamres.2009.10.006

Schmitz, M.D. 2012. Radiometric ages used in GTS2012. *In*: Gradstein, F.M., Ogg, J.G., Schmitz, M.D. and Ogg, G.M. (eds) *The Geologic Time Scale*. Elsevier, Boston, 1045–1082, https://doi.org/10.1016/b978-0-444-59425-9.15002-4

Scholle, P.A. and Ulmer-Scholle, D.S. 2003. *A Color Guide to the Petrography of Carbonate Rocks: Grains, Textures, Porosity, Diagenesis. AAPG Memoir 77*. AAPG.

Schrag, D.P., Higgins, J.A., Macdonald, F.A. and Johnston, D.T. 2013. Authigenic carbonate and the history of the global carbon cycle. *Science*, **339**, 540–543, https://doi.org/10.1126/science.1229578

Schröder, S., Bekker, A., Beukes, N.J., Strauss, H. and Van Niekerk, H.S. 2008. Rise in seawater sulphate concentration associated with the Paleoproterozoic positive carbon isotope excursion: evidence from sulphate evaporites in the ∼2.2–2.1 Gyr shallow-marine Lucknow Formation, South Africa. *Terra Nova*, **20**, 108–117, https://doi.org/10.1111/j.1365-3121.2008.00795.x

Shi, W., Li, C. and Algeo, T.J. 2017. Quantitative model evaluation of organic carbon oxidation hypotheses for the Ediacaran Shuram carbon isotopic excursion. *Science China Earth Sciences*, **60**, 2118–2127, https://doi.org/10.1007/s11430-017-9137-1

Shi, W., Li, C. *et al.* 2018. Sulfur isotope evidence for transient marine-shelf oxidation during the Ediacaran Shuram Excursion. *Geology*, **46**, 267–270, https://doi.org/10.1130/G39663.1

Shields, G.A., Deynoux, M., Strauss, H., Paquet, H. and Nahon, D. 2007. Barite-bearing cap dolostones of the Taoudéni Basin, northwest Africa: sedimentary and isotopic evidence for methane seepage after a Neoproterozoic glaciation. *Precambrian Research*, **153**, 209–235, https://doi.org/10.1016/j.precamres.2006.11.011

Shields, G.A., Mills, B.J.W., Zhu, M., Raub, T.D., Daines, S.J. and Lenton, T.M. 2019. Unique Neoproterozoic carbon isotope excursions sustained by coupled evaporite dissolution and pyrite burial. *Nature Geoscience*, **12**, 823–827, https://doi.org/10.1038/s41561-019-0434-3

Smith, A.G. 2012. A review of the Ediacaran to Early Cambrian ('Infra-Cambrian') evaporites and associated sediments of the Middle East. *Geological Society, London, Special Publications*, **366**, 229–250, https://doi.org/10.1144/sp366.12

Song, H., Jiang, G. *et al.* 2017. The onset of widespread marine red beds and the evolution of ferruginous oceans. *Nature Communications*, **8**, 399, https://doi.org/10.1038/s41467-017-00502-x

Sperling, E.A., Wolock, C.J. *et al.* 2015. Statistical analysis of iron geochemical data suggests limited late Proterozoic oxygenation. *Nature*, **523**, 451–454, https://doi.org/10.1038/nature14589

Stewart, J.H., McMenamin, M.A. and Morales-Ramirez, J. 1984. Upper Proterozoic and Cambrian rocks in the Caborca region, Sonora, Mexico—physical stratigraphy, biostratigraphy, paleocurrent studies, and regional relations. *US Geological Survey Professional Paper*, **1309**, 36.

Stolper, D.A. and Keller, C.B. 2018. A record of deep-ocean dissolved O_2 from the oxidation state of iron in submarine basalts. *Nature*, **553**, 323–327, https://doi.org/10.1038/nature25009

Summa, C.L. 1993. *Sedimentologic, Stratigraphic, and Tectonic Controls of A Mixed Carbonate-Siliciclastic Succession: Neoproterozoic Johnnie Formation, Southeast California*. PhD thesis, Massachusetts Institute of Technology.

Sun, X. and Turchyn, A.V. 2014. Significant contribution of authigenic carbonate to marine carbon burial. *Nature Geoscience*, **7**, 201–204, https://doi.org/10.1038/ngeo2070

Tang, M., Ehreiser, A. and Li, Y.-L. 2014. Gypsum in modern Kamchatka volcanic hot springs and the Lower Cambrian black shale: applied to the microbial-mediated precipitation of sulfates on Mars. *American Mineralogist*, **99**, 2126–2137, https://doi.org/10.2138/am-2014-4754

Tian, X. and Luo, K. 2017. Distribution and enrichment patterns of selenium in the Ediacaran and early Cambrian strata in the Yangtze Gorges area, South China. *Science China Earth Sciences*, **60**, 1268–1282, https://doi.org/10.1007/s11430-016-9045-1

Torres, M.E., Brumsack, H., Bohrmann, G. and Emeis, K. 1996. Barite fronts in continental margin sediments: a new look at barium remobilization in the zone of sulfate reduction and formation of heavy barites in diagenetic fronts. *Chemical Geology*, **127**, 125–139, https://doi.org/10.1016/0009-2541(95)00090-9

Tostevin, R., Clarkson, M.O. *et al.* 2019. Uranium isotope evidence for an expansion of anoxia in terminal Ediacaran oceans. *Earth and Planetary Science Letters*, **506**, 104–112, https://doi.org/10.1016/j.epsl.2018.10.045

Turchyn, A.V., Bradbury, H.J., Walker, K. and Sun, X. 2021. Controls on the precipitation of carbonate minerals within marine sediments. *Frontiers in Earth Science*, **9**, https://doi.org/10.3389/feart.2021.618311

Turner, E.C. and Bekker, A. 2016. Thick sulfate evaporite accumulations marking a mid-Neoproterozoic oxygenation event (Ten Stone Formation, Northwest Territories, Canada). *Geological Society of America Bulletin*, **128**, 203–222, https://doi.org/10.1130/b31268.1

Von Breymann, M.T., Emeis, K.-C. and Suess, E. 1992. Water depth and diagenetic constraints on the use of barium as a palaeoproductivity indicator. *Geological Society, London, Special Publications*, **64**, 273–284, https://doi.org/10.1144/GSL.SP.1992.064.01.18

Wang, Z. and Li, G. 1991. Barite and witherite deposits in Lower Cambrian shales of South China: stratigraphic distribution and geochemical characterization. *Economic Geology*, **86**, 354–363, https://doi.org/10.2113/gsecongeo.86.2.354

Wang, J., Jiang, G., Xiao, S., Li, Q. and Wei, Q. 2008. Carbon isotope evidence for widespread methane seeps in the *c.* 635 Ma Doushantuo cap carbonate in south China. *Geology*, **36**, 347–350, https://doi.org/10.1130/G24513A.1

Wang, X., Jiang, G., Shi, X. and Xiao, S. 2016. Paired carbonate and organic carbon isotope variations of the Ediacaran Doushantuo Formation from an upper slope section at Siduping, South China. *Precambrian Research*, **273**, 53–66, https://doi.org/10.1016/j.precamres.2015.12.010

Wang, W., Hu, Y., Muscente, A.D., Cui, H., Guan, C., Hao, J. and Zhou, C. 2021. Revisiting Ediacaran sulfur isotope chemostratigraphy with *in situ* nanoSIMS analysis of sedimentary pyrite. *Geology*, **49**, 611–616, https://doi.org/10.1130/G48262.1

Warren, J.K. 2016. Interpreting Evaporite Textures. *In*: Warren, J.K. (ed.) *Evaporites: A Geological Compendium*. Springer International, Cham, 1–83, https://doi.org/10.1007/978-3-319-13512-0_1

Warren, J.K. 2021. Evaporite deposits. *In*: Alderton, D. and Elias, S.A. (eds) *Encyclopedia of Geology (Second Edition)*. Academic Press, Oxford, 945–977, https://doi.org/10.1016/B978-0-08-102908-4.00165-X

Wei, G.-Y., Planavsky, N.J., Tarhan, L.G., Chen, X., Wei, W., Li, D. and Ling, H.-F. 2018. Marine redox fluctuation as a potential trigger for the Cambrian explosion. *Geology*, **46**, 587–590, https://doi.org/10.1130/G40150.1

Wei, G.-Y., Ling, H.-F., Shields, G.A., Hohl, S.V., Yang, T., Lin, Y.-B. and Zhang, F. 2021*a*. Revisiting stepwise ocean oxygenation with authigenic barium enrichments in marine mudrocks. *Geology*, **49**, 1059–1063 https://doi.org/10.1130/g48825.1

Wei, W., Zeng, Z., Shen, J., Tian, L.-L., Wei, G.-Y., Ling, H.-F. and Huang, F. 2021*b*. Dramatic changes in the carbonate-hosted barium isotopic compositions in the Ediacaran Yangtze Platform. *Geochimica et Cosmochimica Acta*, **299**, 113–129, https://doi.org/10.1016/j.gca.2021.02.026

Wood, R.A., Poulton, S.W. *et al.* 2015. Dynamic redox conditions control late Ediacaran metazoan ecosystems in the Nama Group, Namibia. *Precambrian Research*, **261**, 252–271, https://doi.org/10.1016/j.precamres.2015.02.004

Wright, V.P., Ries, A.C. and Munn, S.G. 1990. Intraplatformal basin-fill deposits from the Infracambrian Huqf Group, east central Oman. *Geological Society, London, Special Publications*, **49**, 601–616, https://doi.org/10.1144/GSL.SP.1992.049.01.36

Xiao, S. and Narbonne, G.M. 2020. The Ediacaran Period. *In*: Gradstein, F.M., Ogg, J.G., Schmitz, M.D. and Ogg, G.M. (eds) *Geologic Time Scale 2020*. Elsevier, 521–561, https://doi.org/10.1016/B978-0-12-824360-2.00018-8

Xiao, S., Narbonne, G.M., Zhou, C., Laflamme, M., Grazhdankin, D.V., Moczydłowska-Vidal, M. and Cui, H. 2016. Toward an Ediacaran time scale: problems, protocols, and prospects. *Episodes*, **39**, 540–555, https://doi.org/10.18814/epiiugs/2016/v39i4/103886

Xu, L., Lehmann, B., Mao, J., Zheng, W., Ye, H. and Li, H. 2016. Strontium, sulfur, carbon, and oxygen isotope geochemistry of the Early Cambrian strata-bound barite and witherite deposits of the Qinling-Daba Region, Northern Margin of the Yangtze Craton, China. *Economic Geology*, **111**, 695–718, https://doi.org/10.2113/econgeo.111.3.695

Yao, W., Griffith, E. and Paytan, A. 2020. Pelagic barite: tracer of ocean productivity and a recorder of isotopic compositions of seawater S, O, Sr, Ca and Ba. *In*: Lyons, T., Turchyn, A. and Reinhard, C. (eds) *Elements in Geochemical Tracers in Earth System Science*. Cambridge University Press, Cambridge, 1–22, https://doi.org/10.1017/9781108847162

Zhang, F., Xiao, S. *et al.* 2018. Extensive marine anoxia during the terminal Ediacaran Period. *Science Advances*, **4**, eaan8983, https://doi.org/10.1126/sciadv.aan8983

Zhang, F., Xiao, S. *et al.* 2019. Global marine redox changes drove the rise and fall of the Ediacara biota. *Geobiology*, **17**, 594–610, https://doi.org/10.1111/gbi.12359

Zhao, M., Planavsky, N., Oehlert, A.M., Wei, G. and Gong, Z. 2020. Simulating meteoric and mixing zone carbonate diagenesis with a two-dimensional reactive transport model. *American Journal of Science*, **320**, 599–636, https://doi.org/10.2475/09.2020.02

Zhou, C. and Xiao, S. 2007. Ediacaran $\delta^{13}C$ chemostratigraphy of South China. *Chemical Geology*, **237**, 89–108, https://doi.org/10.1016/j.chemgeo.2006.06.021

Zhou, C., Bao, H., Peng, Y. and Yuan, X. 2010. Timing the deposition of ^{17}O-depleted barite at the aftermath of Nantuo glacial meltdown in South China. *Geology*, **38**, 903–906, https://doi.org/10.1130/G31224.1

Zhou, C., Jiang, S., Xiao, S., Chen, Z. and Yuan, X. 2012. Rare earth elements and carbon isotope geochemistry of the Doushantuo Formation in South China: implication for middle Ediacaran shallow marine redox conditions. *Chinese Science Bulletin*, **57**, 1998–2006, https://doi.org/10.1007/s11434-012-5082-6

Zhou, X., Chen, D., Dong, S., Zhang, Y., Guo, Z., Wei, H. and Yu, H. 2015. Diagenetic barite deposits in the Yurtus Formation in Tarim Basin, NW China: implications for barium and sulfur cycling in the earliest Cambrian. *Precambrian Research*, **263**, 79–87, https://doi.org/10.1016/j.precamres.2015.03.006

Zhou, C., Guan, C., Cui, H., Ouyang, Q. and Wang, W. 2016. Methane-derived authigenic carbonate from the lower Doushantuo Formation of South China: implications for seawater sulfate concentration and global carbon cycle in the early Ediacaran ocean. *Palaeogeography, Palaeoclimatology, Palaeoecology*, **461**, 145–155, https://doi.org/10.1016/j.palaeo.2016.08.017

Zhou, C., Xiao, S., Wang, W., Guan, C., Ouyang, Q. and Chen, Z. 2017. The stratigraphic complexity of the middle Ediacaran carbon isotopic record in the Yangtze Gorges area, South China, and its implications for the age and chemostratigraphic significance of the Shuram excursion. *Precambrian Research*, **288**, 23–38, https://doi.org/10.1016/j.precamres.2016.11.007

Zhu, M., Strauss, H. and Shields, G.A. 2007*a*. From snowball earth to the Cambrian bioradiation: calibration of Ediacaran–Cambrian earth history in South China. *Palaeogeography, Palaeoclimatology, Palaeoecology*, **254**, 1–6, https://doi.org/10.1016/j.palaeo.2007.03.026

Zhu, M., Zhang, J. and Yang, A. 2007*b*. Integrated Ediacaran (Sinian) chronostratigraphy of South China. *Palaeogeography, Palaeoclimatology, Palaeoecology*, **254**, 7–61, https://doi.org/10.1016/j.palaeo.2007.03.025

Zhu, M., Lu, M. *et al.* 2013. Carbon isotope chemostratigraphy and sedimentary facies evolution of the Ediacaran Doushantuo Formation in western Hubei, South China. *Precambrian Research*, **225**, 7–28, https://doi.org/10.1016/j.precamres.2011.07.019

Zhu, M., Zhang, J. *et al.* 2021. Neoproterozoic stratigraphy, depositional environments & hydrocarbon source-reservoir-seal bed assemblage in South China. *In*: Sun, S. and Wang, T.-G. (eds) *Meso-Neoproterozoic Geology and Petroleum Resources*. Springer & Science, in press.